UNIVERSIDADE DE SÃO PAULO
ESCOLA DE ENGENHARIA DE SÃO CARLOS

Norman Chavez Cussy

Efeitos do número de Reynolds na hidrodinâmica de meso-escala de escoamentos gás-sólido fluidizados

São Carlos

2017

Norman Chavez Cussy

Efeitos do número de Reynolds na hidrodinâmica de meso-escala de escoamentos gás-sólido fluidizados

Dissertação apresentada à Escola de Engenharia de São Carlos da Universidade de São Paulo, para obtenção do título de Mestre em Ciências - Programa de Pós-Graduação em Engenharia Mecânica.

Área de concentração: Térmica e Fluídos

Supervisor: Prof. Dr. Fernando E. Milioli

ESTE EXEMPLAR TRATA-SE DA
VERSÃO CORRIGIDA. A VERSÃO
ORIGINAL ENCONTRA-SE
DISPONÍVEL JUNTO AO
DEPARTAMENTO DE ENGENHARIA
MECÂNICA DA

EESC-USP

São Carlos
2017

EESC - USP
Biblioteca
CAMPUS DE S. CARLOS

EESC/USP
Serviço de Pós Graduação
Protocolado em 08 / 11 / 2017

Class. TESE
Cutt. 9888

Tombo T2162/17
Sysno [illegible]

31100269418

AUTORIZO A REPRODUÇÃO TOTAL OU PARCIAL DESTE TRABALHO, POR QUALQUER MEIO CONVENCIONAL OU ELETRÔNICO, PARA FINS DE ESTUDO E PESQUISA, DESDE QUE CITADA A FONTE.

Chavez-Cussy, Norman
C512e Effects of Reynolds number on the meso-scale hydrodynamics of fluidized gas-solid flows / Norman Chavez-Cussy; orientador Fernando Eduardo Milioli. São Carlos, 2017.

Dissertação (Mestrado) - Programa de Pós-Graduação em Engenharia Mecânica e Área de Concentração em Térmica e Fluídos -- Escola de Engenharia de São Carlos da Universidade de São Paulo, 2017.

1. Gas-solid flow. 2. Reynolds number. 3. Two-fluid modeling. 4. Meso-scale parameters. I. Título.

FOLHA DE JULGAMENTO

Candidato: Engenheiro **NORMAN CHAVEZ CUSSY.**

Título da dissertação: "Efeitos do número de Reymolds na hidrodinâmica de meso-escala de escoamentos gás-sólido fluidizados".

Data da defesa: 05/10/2017.

Comissão Julgadora:	**Resultado:**
Prof. Dr. **Fernando Eduardo Milioli** **(Orientador)** (Escola de Engenharia de São Carlos/EESC)	Aprovado
Prof. Dr. **Rodrigo Béttega** (Universidade Federal de São Carlos/UFSCar)	APROVADO
Prof. Dr. **Anderson Antonio Ubices de Moraes** (Universidade Federal de São Carlos/UFSCar)	APROVADO

Coordenador do Programa de Pós-Graduação em Engenheira Mecânica:
Prof. Associado **Gherhardt Ribatski**

Presidente da Comissão de Pós-Graduação:
Prof. Associado **Luís Fernando Costa Alberto**

For my loving mother Adelaida

ACKNOWLEDGEMENTS

To my advisor Prof. Fernando Eduardo Milioli (Ph.D.) for competence, patience and concern for the development of the work.

To my colleagues and researchers of GMEGS (Group of Gas-Solid Flow Modeling) at EESC/USP: Christian Milioli (Ph.D.), Joseph Mouallem (M.Sc.), Reza Amini (M.Sc.) and Gabriel Netzlaff (B.Sc.) who worked with me on this project.

To the professors and staff of NETef (Núcleo de Engenharia Térmica e Fluidos da EESC/USP) for teaching and knowledge.

To CNPq (Conselho Nacional de Desenvolvimento Científico e Tecnológico), for the scholarship funding for the Master's program.

To FAPESP (Fundação de Amparo à Pesquisa do Estado de São Paulo) and to CNPq for the infra-structure and computing equipment available at the Gas-Solid Flow Modeling Laboratory of NETeF/EESC/USP.

To USP (Universidade de São Paulo) and EESC (Escola de Engenharia de São Carlos), for the knowledge and wisdom imparted in their classrooms.

To my family, a special feeling of gratitude to my loving parents Antonio and Adelaida, for the continuous support.

ABSTRACT

CHAVEZ-CUSSY, Norman **Effects of Reynolds number on the meso-scale hydrodynamics of fluidized gas-solid flows**. 2017. 99p. Dissertação (Mestrado) - Escola de Engenharia de São Carlos, Universidade de São Paulo, São Carlos, 2017.

Filtered two-fluid models have been widely used to simulate gas-particle flows in fluidized beds, which require closures for filtered interface interaction forces and stresses. Such closures have been recently derived from results of highly resolved simulations applying microscopic two-fluid modeling. The usual highly resolved simulation is applied over periodic domains where the flow driving force is enforced through a boundary imposed axial gas-pressure gradient which is chosen to exactly match the gravity acting on the average gas-particle mixture. This renders a particulate flow field which is upwards in low solid concentration regions and downwards in high solid concentration regions, with Reynolds numbers varying in a very confined low range. In such a condition Reynolds number is found not to significantly affect filtered parameters. In the current work the effect of Reynolds number over filtered parameters is evaluated under more realistic gas flow conditions. The more recent closure models for drag and stresses derived from microscopic two-fluid modeling have been formulated as a function of filter size, filtered solid fraction and filtered slip velocity (Milioli et al., 2013, Sarkar et al., 2016). Correlations have been proposed where the solid volume fraction is usually referred to as a first marker, while the filtered slip velocity has been named a second marker. By imposing more realistic Reynolds numbers to the flow, those markers are revised as for their effects over relevant filtered parameters, and the Reynolds number itself is showed to be an additional marker to be accounted for. The domain average solid fraction is also considered as a possible additional marker. This work investigates how the domain average gas flow Reynolds number, and the domain average solid volume fraction, affect relevant parameters related to filtered interface forces between the phases, and related to filtered and effective stresses in both phases. The present concern is turned to circulating fluidized bed applications considering a high Stokes number particulate and average solid fractions inside the dilute flow regime typical of risers. Computational experiments have been developed for ranges of solid fractions and gas flow rates covering flow regimes typical of risers. The MFIX open source code has been used in all the simulations. The ultimate goal which is pursued is to provide new evidence so that more realistic closure models can be derived for filtered two-fluid modeling of fluidized gas-particle flows.

Keywords: two-fluid modeling, sub-grid modeling, highly resolved simulation, gas-solid flow, fluidization, risers.

RESUMO

CHAVEZ-CUSSY, Norman **Efeitos do número de Reynolds na hidrodinâmica de meso-escala de escoamentos gás-sólido fluidizados**. 2017. 99p. Dissertação (Mestrado) - Escola de Engenharia de São Carlos, Universidade de São Paulo, São Carlos, 2017.

Modelos de dois fluidos filtrados tem sido largamente utilizados para simulação de escoamentos gás-sólido em leitos fluidizados. Estes modelos requerem fechamentos para forças interativas de interface e tensões filtradas, os quais tem sido recentemente gerados a partir de resultados de simulações altamente resolvidas aplicando modelagem microscópica de dois fluidos. A simulação altamente resolvida usual é aplicada sobre domínios periódicos, onde o "driving force"do escoamento é provido por um gradiente axial de pressão imposto à fase gás através dos contornos, que é escolhido para exatamente compensar a gravidade atuando sobre a mistura gás-partícula média. Isso produz um escoamento particulado ascendente em regiões de baixas concentrações de sólido, e descendente em regiões de alta concentração de sólido, com números de Reynolds baixos e variando em faixa bastante restrita. Sob tais condições observa-se que o número de Reynolds não afeta significativamente parâmetros filtrados. No presente trabalho o efeito do número de Reynolds sobre parâmetros filtrados é avaliado sob condições de escoamento gás-sólido mais realistas. Os modelos de fechamento mais recentes para arrasto e tensões derivados de modelagem microscópica de dois fluidos tem sido formulados em função de tamanho de filtro, fração volumétrica de sólido filtrada, e velocidade de deslizamento filtrada (Milioli et al., 2013; Sarkar et al., 2016). Correlações tem sido propostas onde a fração volumétrica de sólido é usualmente referida como primeiro marcador, enquanto a velocidade de deslizamento é referida como segundo marcador. Através da imposição de números de Reynolds mais realistas ao escoamento, estes marcadores são revisados quanto a seus efeitos sobre parâmetros filtrados relevantes, e mostra-se que o próprio número de Reynolds apresenta-se como um marcador adicional a ser considerado. A fração de sólido média no domínio é também considerada como um possível marcador adicional. Neste trabalho investiga-se como o número de Reynolds médio do gás e a fração de sólido média no domínio afetam parâmetros relacionados a forças de interface entre fases filtradas, e relacionados a tensões filtradas e efetivas em ambas as fases. O presente interesse direciona-se para aplicações de leitos fluidizados circulantes, considerando-se particulado de elevado número de Stokes e frações de sólido médias no domínio dentro do regime de escoamento diluído típico de "risers". Experimentos computacionais foram desenvolvidos para faixas de frações de sólido e fluxos de gás cobrindo regimes de escoamento típicos de "risers". O código aberto MFIX é usado em todas as simulações. Como objetivo final busca-se prover novas evidencias que venham a contribuir para o desenvolvimento de modelos de fechamento mais realistas para modelos filtrados de dois fluidos para escoamentos gás-sólido fluidizados.

Palavras-chave: modelagem de dois fluidos,modelagem sub-malha, simulação altamente resolvida, escoamento gás-sólido, fluidização, risers.

LIST OF FIGURES

Figure 1 – Flow regimes in fluidized beds 24

Figure 2 – Circulating Fluidized Bed 26

Figure 3 – Structures of particles in riser flows 27

Figure 4 – Stokes number in fluid-solid flow associated to the motion of a particle for a particular case 29

Figure 5 – Multi-scale Modeling 31

Figure 6 – Different topologies in gas-solid flow 44

Figure 7 – Typical behavior of the domain average of any variable while simulating in a periodic domain. 51

Figure 8 – Run configuration 53

Figure 9 – Filter-window 55

Figure 10 – Dimensionless gas velocity in the axial direction, $\langle \mathbf{v}_g \rangle^*_{susp}$, as a function of dimensionless time, t^*, for the runs under suspension like conditions, for domain average solid volume fractions $\langle \phi_s \rangle = 0.05$ (a), 0.15 (b) and 0.25 (c). 58

Figure 11 – Grayscale plots of solid volume fraction in the domain inside the statistical steady state regime, for simulations with domain average solid fractions $\langle \phi_s \rangle = 0.05$, 0.15 and 0.25 (columns), and gas Reynolds number ratios $\langle Re_g \rangle / \langle Re_g \rangle_{susp} = 1$, 8.15, 16.30, 24.45 (rows) 60

Figure 12 – Drag coefficient correction, H, as a function of the filtered solid volume fraction, $\overline{\phi}_s$, for various gas Reynolds ratios $\langle Re_g \rangle / \langle Re_g \rangle_{susp} = 1$ (–), 4.08 (○), 8.15 (◁), 12.23 (◊), 16.30 (▷), 20.34 (□), and 24.45 (▽), for the domain average solid volume fraction $\langle \phi_s \rangle = 0.05$ (a), 0.15 (b) and 0.25 (c). The results stand for the dimensionless filtered axial slip velocities $\tilde{\mathbf{v}}_{slip,y} / \mathbf{v}_t = 0.85$, 2.03 and 4.85, and the dimensionless filter size $\Delta_f / \left(\mathbf{v}_t^2 / \mathbf{g} \right) = 2.056$ 62

Figure 13 – Drag coefficient correction, H, as a function of the filtered solid volume fraction, $\overline{\phi}_s$, for the domain average solid volume fractions $\langle \phi_s \rangle =$ 0.05 (full lines), 0.15 (gray symbols) and 0.25 (white symbols), for gas Reynolds ratios $\langle Re_g \rangle / \langle Re_g \rangle_{susp} = 1$ (a), 4.08 (b), 8.15 (c), 12.23 (d), 16.30 (e), 20.34 (f). The results stand for the dimensionless filtered axial slip velocities $\tilde{\mathbf{v}}_{slip,y} / \mathbf{v}_t = 0.85$, 2.03 and 4.85, and the dimensionless filter size $\Delta_f / \left(\mathbf{v}_t^2 / \mathbf{g} \right) = 2.056$ 63

Figure 14 – Filtered solid pressure, $P_{fil,s}$, as a function of the filtered solid volume fraction, $\overline{\phi}_s$, for various gas Reynolds ratios $\langle Re_g\rangle/\langle Re_g\rangle_{susp} = 1$ (–), 4.08 (○), 8.15 (◁), 12.23 (◇), 16.30 (▷), 20.34 (□), and 24.45 (▽), for the domain average solid volume fraction $\langle \phi_s\rangle = 0.05$ (a), 0.15 (b) and 0.25 (c). The results stand for the dimensionless filtered axial slip velocity $\tilde{\mathbf{v}}_{slip,y}/\mathbf{v}_t = 0.85$ and the dimensionless filter size $\Delta_f/\left(\mathbf{v}_t^2/\mathbf{g}\right) = 2.056$ . . 65

Figure 15 – Filtered solid pressure, $P_{fil,s}$, as a function of the filtered solid volume fraction, $\overline{\phi}_s$, for various gas Reynolds ratios $\langle Re_g\rangle/\langle Re_g\rangle_{susp} = 1$ (–), 4.08 (○), 8.15 (◁), 12.23 (◇), 16.30 (▷), 20.34 (□), and 24.45 (▽), for the domain average solid volume fraction $\langle \phi_s\rangle = 0.05$ (a), 0.15 (b) and 0.25 (c). The results stand for the dimensionless filtered axial slip velocity $\tilde{\mathbf{v}}_{slip,y}/\mathbf{v}_t = 4.85$ and the dimensionless filter size $\Delta_f/\left(\mathbf{v}_t^2/\mathbf{g}\right) = 2.056$ . . 66

Figure 16 – Filtered solid dynamic viscosity, $\mu_{fil,s}$, as a function of the filtered solid volume fraction, $\overline{\phi}_s$, for various gas Reynolds ratios $\langle Re_g\rangle/\langle Re_g\rangle_{susp} = 1$ (–), 4.08 (○), 8.15 (◁), 12.23 (◇), 16.30 (▷), 20.34 (□), and 24.45 (▽), for the domain average solid volume fraction $\langle \phi_s\rangle = 0.05$ (a), 0.15 (b) and 0.25 (c). The results stand for the dimensionless filtered axial slip velocity $\tilde{\mathbf{v}}_{slip,y}/\mathbf{v}_t = 0.85$ and the dimensionless filter size $\Delta_f/\left(\mathbf{v}_t^2/\mathbf{g}\right) = 2.056$ . . 67

Figure 17 – Effective solid and gas pressures, $P_{eff,s}$ and $P_{eff,g}$, as a function of the filtered solid volume fraction, $\overline{\phi}_s$, for various gas Reynolds ratios $\langle Re_g\rangle/\langle Re_g\rangle_{susp} = 1$ (–), 4.08 (○), 8.15 (◁), 12.23 (◇), 16.30 (▷), 20.34 (□), and 24.45 (▽), for the domain average solid volume fraction $\langle \phi_s\rangle =$ 0.05 (a), 0.15 (b) and 0.25 (c). The results stand for the dimensionless filtered axial slip velocity $\tilde{\mathbf{v}}_{slip,y}/\mathbf{v}_t = 0.85$ and the dimensionless filter size $\Delta_f/\left(\mathbf{v}_t^2/\mathbf{g}\right) = 2.056$ 69

Figure 18 – Effective solid and gas dynamic viscosities, $\mu_{eff,s}$ and $\mu_{eff,g}$, as a function of the filtered solid volume fraction, $\overline{\phi}_s$, for various gas Reynolds ratios $\langle Re_g\rangle/\langle Re_g\rangle_{susp} = 1$ (–), 4.08 (○), 8.15 (◁), 12.23 (◇), 16.30 (▷), 20.34 (□), and 24.45 (▽), for the domain average solid volume fraction $\langle \phi_s\rangle =$ 0.05 (a), 0.15 (b) and 0.25 (c). The results stand for the dimensionless filtered axial slip velocity $\tilde{\mathbf{v}}_{slip,y}/\mathbf{v}_t = 0.85$ and the dimensionless filter size $\Delta_f/\left(\mathbf{v}_t^2/\mathbf{g}\right) = 2.056$ 70

Figure 19 – Drag coefficient correction, H, as a function of the filtered solid volume fraction, $\overline{\phi}_s$, for various gas Reynolds ratios $\langle Re_g\rangle/\langle Re_g\rangle_{susp} = 1$ (–), 4.08 (○), 8.15 (◁), 12.23 (◇), 16.30 (▷), 20.34 (□), and 24.45 (▽), for the domain average solid volume fraction $\langle \phi_s\rangle = 0.05$ (a), 0.15 (b) and 0.25 (c). The results stand for the dimensionless filtered axial slip velocities $\tilde{\mathbf{v}}_{slip,y}/\mathbf{v}_t = 0.85$, 2.03 and 4.85, and the dimensionless filter size $\Delta_f/\left(\mathbf{v}_t^2/\mathbf{g}\right) = 1.028$ 84

Figure 20 – Drag coefficient correction, H, as a function of the filtered solid volume fraction, $\overline{\phi}_s$, for various gas Reynolds ratios $\langle Re_g\rangle/\langle Re_g\rangle_{susp} = 1$ (–), 4.08 (○), 8.15 (◁), 12.23 (◇), 16.30 (▷), 20.34 (□), and 24.45 (▽), for the domain average solid volume fraction $\langle\phi_s\rangle = 0.05$ (a), 0.15 (b) and 0.25 (c). The results stand for the dimensionless filtered axial slip velocities $\tilde{\mathbf{v}}_{slip,y}/\mathbf{v}_t = 0.85$, 2.03 and 4.85, and the dimensionless filter size $\Delta_f/\left(\mathbf{v}_t^2/\mathbf{g}\right) = 4.112$ 85

Figure 21 – Drag coefficient correction, H, as a function of the filtered solid volume fraction, $\overline{\phi}_s$, for the domain average solid volume fractions $\langle\phi_s\rangle = 0.05$ (full lines), 0.15 (gray symbols) and 0.25 (white symbols), for gas Reynolds ratios $\langle Re_g\rangle/\langle Re_g\rangle_{susp} = 1$ (a), 4.08 (b), 8.15 (c), 12.23 (d), 16.30 (e), 20.34 (f). The results stand for the dimensionless filtered axial slip velocities $\tilde{\mathbf{v}}_{slip,y}/\mathbf{v}_t = 0.85$, 2.03 and 4.85, and the dimensionless filter size $\Delta_f/\left(\mathbf{v}_t^2/\mathbf{g}\right) = 1.028$ 86

Figure 22 – Drag coefficient correction, H, as a function of the filtered solid volume fraction, $\overline{\phi}_s$, for the domain average solid volume fractions $\langle\phi_s\rangle = 0.05$ (full lines), 0.15 (gray symbols) and 0.25 (white symbols), for gas Reynolds ratios $\langle Re_g\rangle/\langle Re_g\rangle_{susp} = 1$ (a), 4.08 (b), 8.15 (c), 12.23 (d), 16.30 (e), 20.34 (f). The results stand for the dimensionless filtered axial slip velocities $\tilde{\mathbf{v}}_{slip,y}/\mathbf{v}_t = 0.85$, 2.03 and 4.85, and the dimensionless filter size $\Delta_f/\left(\mathbf{v}_t^2/\mathbf{g}\right) = 4.112$ 87

Figure 23 – Filtered solid pressure, $P_{fil,s}$, as a function of the filtered solid volume fraction, $\overline{\phi}_s$, for various gas Reynolds ratios $\langle Re_g\rangle/\langle Re_g\rangle_{susp} = 1$ (–), 4.08 (○), 8.15 (◁), 12.23 (◇), 16.30 (▷), 20.34 (□), and 24.45 (▽), for the domain average solid volume fraction $\langle\phi_s\rangle = 0.05$ (a), 0.15 (b) and 0.25 (c). The results stand for the dimensionless filtered axial slip velocity $\tilde{\mathbf{v}}_{slip,y}/\mathbf{v}_t = 0.85$ and the dimensionless filter size $\Delta_f/\left(\mathbf{v}_t^2/\mathbf{g}\right) = 1.028$ . . 90

Figure 24 – Filtered solid pressure, $P_{fil,s}$, as a function of the filtered solid volume fraction, $\overline{\phi}_s$, for various gas Reynolds ratios $\langle Re_g\rangle/\langle Re_g\rangle_{susp} = 1$ (–), 4.08 (○), 8.15 (◁), 12.23 (◇), 16.30 (▷), 20.34 (□), and 24.45 (▽), for the domain average solid volume fraction $\langle\phi_s\rangle = 0.05$ (a), 0.15 (b) and 0.25 (c). The results stand for the dimensionless filtered axial slip velocity $\tilde{\mathbf{v}}_{slip,y}/\mathbf{v}_t = 0.85$ and the dimensionless filter size $\Delta_f/\left(\mathbf{v}_t^2/\mathbf{g}\right) = 4.112$ . . 91

Figure 25 – Filtered solid dynamic viscosity, $\mu_{fil,s}$, as a function of the filtered solid volume fraction, $\overline{\phi}_s$, for various gas Reynolds ratios $\langle Re_g\rangle/\langle Re_g\rangle_{susp} = 1$ (–), 4.08 (○), 8.15 (◁), 12.23 (◇), 16.30 (▷), 20.34 (□), and 24.45 (▽), for the domain average solid volume fraction $\langle\phi_s\rangle = 0.05$ (a), 0.15 (b) and 0.25 (c). The results stand for the dimensionless filtered axial slip velocity $\tilde{\mathbf{v}}_{slip,y}/\mathbf{v}_t = 0.85$ and the dimensionless filter size $\Delta_f/\left(\mathbf{v}_t^2/\mathbf{g}\right) = 1.028$ . . 92

Figure 26 – Filtered solid dynamic viscosity, $\mu_{fil,s}$, as a function of the filtered solid volume fraction, $\overline{\phi}_s$, for various gas Reynolds ratios $\langle Re_g\rangle/\langle Re_g\rangle_{susp} = 1$ (−), 4.08 (○), 8.15 (◁), 12.23 (◇), 16.30 (▷), 20.34 (□), and 24.45 (▽), for the domain average solid volume fraction $\langle\phi_s\rangle = 0.05$ (a), 0.15 (b) and 0.25 (c). The results stand for the dimensionless filtered axial slip velocity $\tilde{\mathbf{v}}_{slip,y}/\mathbf{v}_t = 0.85$ and the dimensionless filter size $\Delta_f/\left(\mathbf{v}_t^2/\mathbf{g}\right) = 4.112$ . . 93

Figure 27 – Effective solid and gas pressures, $P_{eff,s}$ and $P_{eff,g}$, as a function of the filtered solid volume fraction, $\overline{\phi}_s$, for various gas Reynolds ratios $\langle Re_g\rangle/\langle Re_g\rangle_{susp} = 1$ (−), 4.08 (○), 8.15 (◁), 12.23 (◇), 16.30 (▷), 20.34 (□), and 24.45 (▽), for the domain average solid volume fraction $\langle\phi_s\rangle =$ 0.05 (a), 0.15 (b) and 0.25 (c). The results stand for the dimensionless filtered axial slip velocity $\tilde{\mathbf{v}}_{slip,y}/\mathbf{v}_t = 0.85$ and the dimensionless filter size $\Delta_f/\left(\mathbf{v}_t^2/\mathbf{g}\right) = 1.028$ 96

Figure 28 – Effective solid and gas pressures, $P_{eff,s}$ and $P_{eff,g}$, as a function of the filtered solid volume fraction, $\overline{\phi}_s$, for various gas Reynolds ratios $\langle Re_g\rangle/\langle Re_g\rangle_{susp} = 1$ (−), 4.08 (○), 8.15 (◁), 12.23 (◇), 16.30 (▷), 20.34 (□), and 24.45 (▽), for the domain average solid volume fraction $\langle\phi_s\rangle =$ 0.05 (a), 0.15 (b) and 0.25 (c). The results stand for the dimensionless filtered axial slip velocity $\tilde{\mathbf{v}}_{slip,y}/\mathbf{v}_t = 0.85$ and the dimensionless filter size $\Delta_f/\left(\mathbf{v}_t^2/\mathbf{g}\right) = 4.112$ 97

Figure 29 – Effective solid and gas dynamic viscosities, $\mu_{eff,s}$ and $\mu_{eff,g}$, as a function of the filtered solid volume fraction, $\overline{\phi}_s$, for various gas Reynolds ratios $\langle Re_g\rangle/\langle Re_g\rangle_{susp} = 1$ (−), 4.08 (○), 8.15 (◁), 12.23 (◇), 16.30 (▷), 20.34 (□), and 24.45 (▽), for the domain average solid volume fraction $\langle\phi_s\rangle =$ 0.05 (a), 0.15 (b) and 0.25 (c). The results stand for the dimensionless filtered axial slip velocity $\tilde{\mathbf{v}}_{slip,y}/\mathbf{v}_t = 0.85$ and the dimensionless filter size $\Delta_f/\left(\mathbf{v}_t^2/\mathbf{g}\right) = 1.028$ 98

Figure 30 – Effective solid and gas dynamic viscosities, $\mu_{eff,s}$ and $\mu_{eff,g}$, as a function of the filtered solid volume fraction, $\overline{\phi}_s$, for various gas Reynolds ratios $\langle Re_g\rangle/\langle Re_g\rangle_{susp} = 1$ (−), 4.08 (○), 8.15 (◁), 12.23 (◇), 16.30 (▷), 20.34 (□), and 24.45 (▽), for the domain average solid volume fraction $\langle\phi_s\rangle =$ 0.05 (a), 0.15 (b) and 0.25 (c). The results stand for the dimensionless filtered axial slip velocity $\tilde{\mathbf{v}}_{slip,y}/\mathbf{v}_t = 0.85$ and the dimensionless filter size $\Delta_f/\left(\mathbf{v}_t^2/\mathbf{g}\right) = 4.112$ 99

LIST OF TABLES

Table 1 – Physical properties of gas and solid. 52
Table 2 – Set up for simulations. 54
Table 3 – Values for filtering. 57
Table 4 – Reynolds number for suspension condition runs. 57
Table 5 – Reynolds numbers for all runs. 59

LIST OF ABBREVIATIONS AND ACRONYMS

MFIX	Multiphase Flow with Interphase eXchange
NETL	National Energy Technology Laboratory
DOE-USA	United States Department of Energy
FCC	Fluid Catalytic Cracking
FBC	Fluidized Bed Combustion
mf	minimum fluidization
BFB	Bubbling Fluidized Bed
TB	Turbulent Bed
FF	Fast Fluidization
PC	Pneumatic Transport
CFB	Circulating Fluidized Bed
LSS	Large Scale Simulations
HRS	Highly Resolved Simulations
DEM	Discrete Element Method
LBM	Lattice Boltzmann Method
MPPIC	Multi-phase Particle in Cell Method
TFM	Two-fluid model
KTGF	Kinetic Theory of Granular Flows
PTE	Pseudo-Thermal Energy
TVD	Total Variation Diminishing

LIST OF SYMBOLS

A	m^2	Single particle surface area
$\mathbf{B}'$	Nm^{-3}	Fluctuation of gas-solid buoyancy force
c_D	–	Single particle drag coefficient
d_p	m	Particle diameter
e	–	Restitution coefficient for particle-particle collisions
$\mathbf{E}$		Symmetric tensor
$\mathbf{F}_d$	N	Single particle friction drag force
Fr_{d_p}	–	Particle size based Froude number
$\mathbf{g}, g$	ms^{-2}	Acceleration of gravity
$\mathbf{g}_0$	–	Radial distribution function
H	–	Drag coefficient correction
$\mathbf{I}$	–	Unit tensor
$\mathbf{J}_{coll}$	$Jm^{-3}s^{-1}$	Rate of dissipation of granular energy by collisional damping.
$\mathbf{J}_{vis}$	$Jm^{-3}s^{-1}$	Rate of dissipation of granular energy by viscous damping.
$\mathbf{M}$	Nm^{-3}	Drag force
P	Nm^{-2}	Pressure
Re_p	–	Particle size based Reynolds number
$\mathbf{s}$	s^{-1}	Strain rate tensor due to viscous plus pressure effects
St_{d_p}	–	Particle size based Stokes number
t	s	Time
u_0	ms^{-1}	Superficial gas velocity
$\mathbf{v}$	ms^{-1}	Velocity vector
v_{mf}	ms^{-1}	Minimum fluidization gas velocity
v_t	ms^{-1}	Free fall terminal gas velocity
y	m	Vertical (axial) Cartesian coordinate

Greek letters

β	$kgm^{-3}s^{-1}$	Micro-scale gas-solid drag coefficient
β^*	–	Wen and Yu drag coefficient (transition regime)
Γ_{slip}	$Jm^{-3}s^{-1}$	Rate of production of granular energy by gas-particle slip
Δ_f	m	Filter size
ϵ_p	–	Particle sphericity
ϵ_{mf}	–	Minimum fluidization void fraction
Θ	m^2s^{-2}	Granular temperature
κ_s	$kgm^{-1}s^{-1}$	Granular thermal conductivity

λ	Nsm^{-2}	Bulk viscosity
μ	Nsm^{-2}	Dynamic viscosity
ρ	kgm^{-3}	Density
$\boldsymbol{\sigma}$	Nm^{-2}	Deviatoric stress tensor
$\boldsymbol{\tau}'$	Nm^{-2}	Reynolds-like stress tensor
τ_p	s	Particle response time
τ_g	s	Turbulence time scale
ϕ	$-$	Volume fraction

Subscripts

eff	Effective, or filtered, or meso-scale related
fil	Filtered
g	Gas phase
i	Horizontal direction
I	Interface
j	Vertical direction
ℓ	A generic phase, either s or g
max	Maximum
r	Relative
s	Solid phase
$susp$	Suspension

Other symbols

$-$	Filtered or volume averaged
$*$	Dimensionless parameter
$\sim$	Favre or mass weighed average, $\tilde{f} = \dfrac{\overline{\phi f}}{\overline{\phi}}$
$\langle \ \rangle$	Domain volume average

CONTENTS

1 INTRODUCTION . . . 23

1.1 Fluidization Regimes . . . 24

1.2 Gas-solid Riser Flows . . . 26

1.3 Modeling Fluidized Gas-Solid Flows . . . 29

1.3.1 Some fundamentals of the Euler-Euler approach . . . 30

1.3.2 Euler-Euler Two-fluid Multi-scale Modeling . . . 31

2 MAIN LITERATURE REVIEW AND OBJECTIVES . . . 33

2.1 Objectives . . . 35

3 METHODOLOGY . . . 37

3.1 Microscopic Two-Fluid Model . . . 37

3.1.1 Microscopic closures for solid phase stresses . . . 40

3.1.2 Microscopic closures for drag . . . 42

3.2 Filtered Two-Fluid Model . . . 45

3.3 Numerical Simulations . . . 50

3.3.1 Numerical Procedure . . . 51

3.3.2 Simulations . . . 52

3.3.3 Filtering and Binning . . . 54

4 RESULTS AND DISCUSSION . . . 57

4.1 Flow topology . . . 59

4.2 Drag coefficient correction . . . 60

4.3 Filtered pressure and dynamic viscosity for solid phase . . . 64

4.4 Effective pressures and dynamic viscosities for solid and gas phases 68

5 CONCLUSIONS AND SUGGESTIONS FOR FUTURE WORK . . . 71

5.1 Conclusions . . . 71

5.2 Some suggestions for future work . . . 73

BIBLIOGRAPHY . . . 75

APPENDIX 81

APPENDIX A – DRAG COEFFICIENT CORRECTION, H . . . 83

APPENDIX B – FILTERED SOLID PRESSURE, $P_{fil,s}$ AND DYNAMIC VISCOSITY $\mu_{fil,s}$ 89

APPENDIX C – EFFECTIVE PRESSURES $P_{eff,s}$ AND $P_{eff,g}$, AND DYNAMIC VISCOSITIES $\mu_{eff,s}$ AND $\mu_{eff,g}$ 95

1 INTRODUCTION

Fluidized bed reactors are widely used in chemical and energy industries, representing a formidable impact on world's economy. Among the most important applications are Fluid Catalytic Cracking (FCC) (King, 1992) and Fluidized Bed Combustion (FBC) as in coal combustion (Basu and Fraser, 1991). In petroleum refineries FCC reactors perform the conversion of high molecular weight hydrocarbons of the crude oil into gasoline and other byproducts. The FBC reactor is used in combustion technology to burn solid fuels as coal and biomass while allowing for pollutant emission control such us those of SOx and NOx. Also it is used in gasification technology to obtain carbon dioxide, methane, hydrogen and other industrial gases.

The development of such reactors is still a very much empirical science, based upon gradually scaled demonstration plants that involve both very high costs and excessive execution times. The current research ultimately intends to contribute in the context of replacing those very expensive plants by computational simulation. Computational simulation of fluidized bed reactors requires accurate modeling, and no accurate modeling can be advanced without a rigorous description of the concerning very heterogeneous gas-solid flows. Those flows are characterized by very dynamic formation, composition and dissipation of entities such as gas bubbles and clusters of particulate, which manifest in a multitude of time and length scales, and profoundly affect mass transfer, heat transfer and chemical reaction rates. Owing to the commonly huge physical volumes that are involved in real scale fluidized bed reactors, only the so called large scale simulations (LSS) are feasible. LSS impose very coarse numerical grids, inside which any heterogeneity is filtered, and their effects are thereby lost. Therefore, if accuracy is desired, closure models must be added to the LSS formulations in order to recover filtered effects.

Literature presents filtered closure models that are derived from results of highly resolved simulations (HRS) with microscopic two-fluid modeling. In those models, relevant filtered parameters are correlated to inside filtered parameters only, taking no account of macro-scale parameters related to flow topology. In the present work macro-scale related parameters are investigated regarding their effects over relevant filtered parameters.

The current research, therefore, ultimately intends to be a contribution for the derivation of increasingly realistic filtered closure models. As in previous works, this is also done by means of computational experiment with microscopic two-fluid modeling. It is proposed to investigate the effect of Reynolds number over filtered parameters, since the current state of the art in this line of development offers only models derived under low Reynolds number conditions. The present concern is turned to the application of high Stokes number particulates which are typical of fluidized bed processes. A high Stokes number (frequently defined as the ratio of the particulate response time to the Kolmogorov time scale or other relevant time scales of the flow) means that the motion of individual particles is not affected by the carrying gas turbulence.

Computational experiments have been developed for ranges of solid fractions and gas flow rates covering flow regimes typical of risers. The MFIX open source code has been used in all the simulations.

1.1 Fluidization Regimes

In the process of gas fluidization a granular material is converted from a static solid-like state to a dynamic fluid-like state using a gas crossing through the granular material.

Flow regime is the characterization of the different configurations of the hydrodynamic of gas-solid fluidized bed based on the motion of the gas and solids, their interactions and physical properties as it is shown in the figure (1). There are many possible configurations depending primarily on the superficial velocity of the gas through the bed u_0, the particle diameter d_p and its density ρ_s. These regimes are known as minimum fluidizing, bubbling, turbulent, fast fluidizing and pneumatic transport.

Figure 1: Flow regimes in fluidized beds

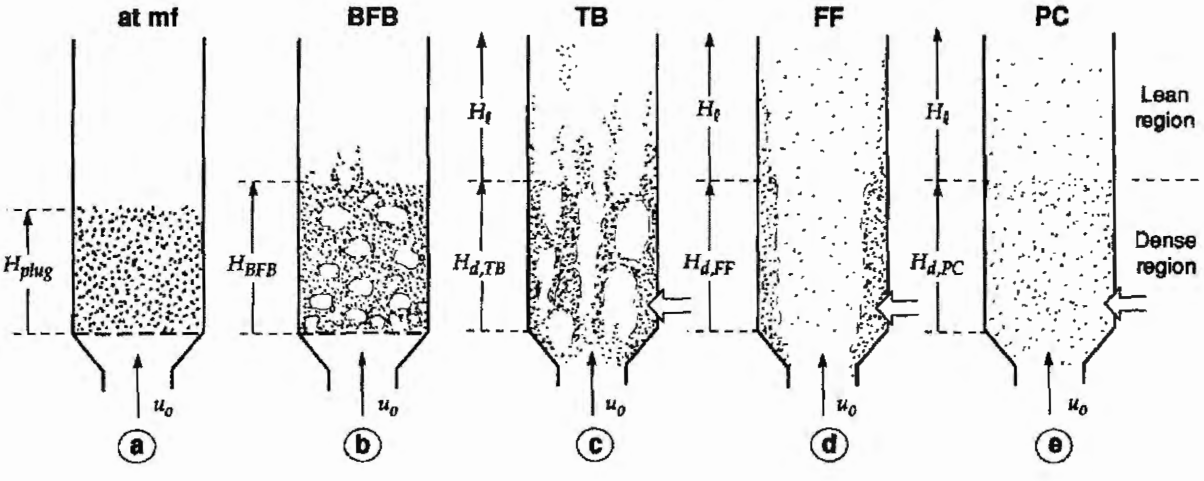

Source: Kunii and Levenspiel (1991).

A fixed bed occurs when the particles remain static. With the gas flowing through the bed, the particles are suspended when the pressure drop exceeds slightly the weight of the solids (this is the minimum fluidizing regime). The voidage increases and an expansion of the bed can be observed. The minimum fluidization velocity v_{mf} is defined at this configuration. As the gas flow rate grows above that required for minimum fluidization, gas bubbles start to develop and rise through the bed while coalescing to each other, and burst at the bed surface (bubbling regime). Further increase of the gas flow rate will disrupt the bubbles into irregular gas voids through the bed (turbulent regime).

As the gas flow rate through the bed is further increased above the turbulent regime, a condition is reached where the particulate is blown out (fast fluidization regime). At this condition the gas velocity is very much related to the particle free fall terminal velocity v_t (the steady state velocity of an individual particle dropping in a quiescent gas).

The free fall terminal velocity of a spherical particle may be determined following Geldart (1986):

$$v_t = \frac{\rho_s g d_p^2}{18\mu_g} \qquad \text{for} \qquad Re \leq 0.2 \qquad \text{Laminar Stokes regime} \tag{1.1}$$

$$v_t = \frac{\rho_s g}{\beta^*} \qquad \text{for} \qquad 0.2 < Re < 1000 \qquad \text{Transition regime} \tag{1.2}$$

$$v_t = \sqrt{\frac{4}{3}\frac{(\rho_s - \rho_g) g d_p}{0.43\rho_g}} \qquad \text{for} \qquad Re \geq 1000 \qquad \text{Turbulent regime} \tag{1.3}$$

where:

$$\beta^* = \frac{3}{4} c_d^* \frac{\rho_g v_t}{d_p} \qquad \text{(Wen and Yu, 1966)} \tag{1.4}$$

$$c_d^* = \frac{24}{Re^*}\left(1 + 0.15 Re^{*0.687}\right) \qquad \text{(Schiller and Newmann, 1935)} \tag{1.5}$$

$$Re^* = \frac{\rho_g v_t d_p}{\mu_g} \tag{1.6}$$

Ergun (1952) found an equation for the minimum fluidization velocity and Haider and Levenspiel (1989) for the terminal velocity for spherical particles, each one in its dimensionless form.

$$\frac{150}{\epsilon_{mf}^3}(1 - \epsilon_{mf}) v_{mf}^* + \frac{1.75}{\epsilon_{mf}^3}\left(v_{mf}^*\right)^2 d_p^* = \left(d_p^*\right)^2 \tag{1.7}$$

$$v_t^* = \left(\frac{18}{(d_p^*)^2} + \frac{0.591}{(d_p^*)^{1/2}}\right)^{-1} \tag{1.8}$$

Based on the dimensionless particle diameter d_p^* and gas velocity v^* defined as:

$$d_p^* = d_p \left(\frac{\rho_g(\rho_s - \rho_g)g}{\mu_g^2} \right)^{1/3} \tag{1.9}$$

$$v^* = v \left(\frac{\rho_g^2}{\mu_g(\rho_s - \rho_g)g} \right)^{1/3} \tag{1.10}$$

If the gas velocity exceeds the fast fluidized condition the system is in the pneumatic conveying regime.

1.2 Gas-solid Riser Flows

In a circulating fluidized bed (CFB) the solid particles circulate between the main column (*riser*) and the feeding back loop column (*downcomer*). The particles which are continuously discharged from the top of the riser must be replaced or re-entered through the downcomer in the bottom of the riser. The riser, which operates in the fast fluidization regime, is the section of the reactor where the intended chemical reaction process takes place. A layout of a circulating fluidized bed reactor is shown in the figure (2).

Figure 2: Circulating Fluidized Bed

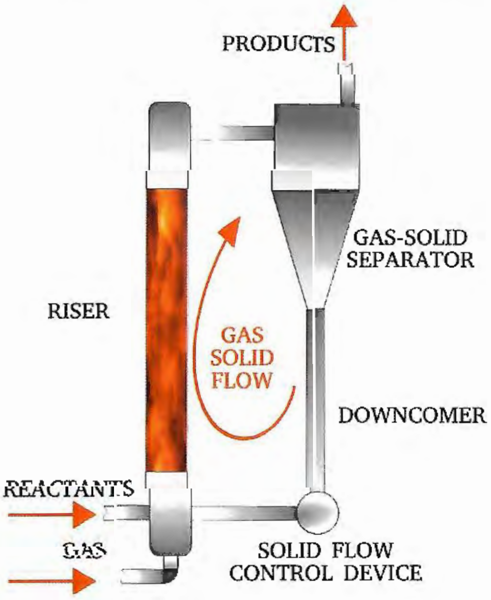

Source: Elaborated by the author.

Besides the riser and the downcomer, a CFB system also includes a gas-solid separator (cyclone) and a solid flow control device. In the riser the solids flow usually co-currently upward with the fluidizing gas which is introduced at the bottom of the column. The solid particles come from the downcomer via the control device and are carried upward with the gas. At the top of the riser, the mixture flows to a gas-solid separator. Separated particles flow to the downcomer upper part and are fed back to the riser. The modeling effort in the current work concerns the riser flow.

The CFB system can be classified based on many different parameters as concentration of the solid, type of material, kinetic of the chemical reaction if it exists, gas-solid mass flow rates, recirculation of the solid, etc. Gas flow velocities can vary over a wide range typically from about 5 m/s up to about 28 m/s depending on the solid particle diameter, which typically ranges from 40 μm up to about 1000 μm. The recirculation solid mass flux is usually between 10 kg/m^2s and 1200 kg/m^2s, (Sun, 1992). The solid concentration in the stream depends on the particular application and can vary from very dilute to very dense conditions, usually from 0.01 % up to 20 % and even denser, (Bi and Grace, 1997). The capacity of production of the system is more related to the transversal area of the riser, while the required time of residence of the solid, which is quite dependent on to the kinetics of the chemical reactions and hydrodynamics, is more related to the high of the riser. The gas-solid flow in risers is characterized by complex hydrodynamics. The spatial distribution of the particles is non uniform. Solid particles recirculate inside the riser, ascending with the flowing gas streams in the core of the column while descending near the walls because of the low gas velocity at those regions. The fluctuating, non-uniform, heterogeneous and unstable behavior of the flow comes from a continuous formation, dissipation and interaction among coherent structures (clusters of particles), together with dispersed solids in the gaseous phase. Figure (3) illustrates such structures that appear in different scales. As these structures manifest over a multitude of length and time scales, modeling and simulation must be set rigorously, so as to capture all the physics involved.

Figure 3: Structures of particles in riser flows

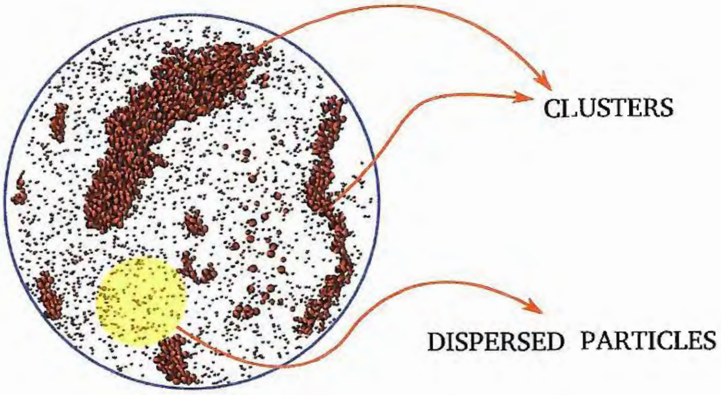

Source: Elaborated by the author.

The length scales are the problematic issue here as they can range from a few particle sizes up to the size of the column. The time scales, on the other hand, are not an issue since they are much larger than time steps practiced in usual numerical procedures (Sharma et al., 2000). So, the question rests on to accurately account for the effects of even the smaller clusters in the flow field.

The micro-scales of a gas-solid flow are defined as those below which the flow is completely homogeneous, so that no coherent structures are observed. Otherwise, the meso and macro-scales of the flow are quite heterogeneous and fully characterized by coherent structures. The macro-scales are all the scales that can be captured in large scale simulations. The meso-scales are all the scales that are filtered in large scale simulations, and can be captured in highly resolved simulations (see Section 4.1).

Usually, in riser flows, the macro-scale is in the order of $cm - m$, meso-scale in the order of $mm - cm$ and micro-scale in the order of μm.

The particulate structures emerge as a consequence of instabilities related to the relative movement of the gas and solid phases, and due to the dissipation of energy related to the fluctuating movement of particles caused by inelastic collision and viscous damping (Agrawal et al., 2001). The characteristic relative size of meso-scale structures is on the order of 10 up to 100 and even 1000 times particle diameters (Igci and Sundaresan, 2011).

The physical properties of the particles combined to the fluid flow conditions have great impact on particle structures development and behavior. The dimensionless Stokes number is particularly relevant in this context as it tells about the impact of the fluid phase turbulence over the particulate. The Stokes number based on the particle diameter (d_p), is defined as the ratio between a particle relaxing or response time and a gas turbulence time scale. The particle response time is usually taken from the free fall terminal velocity evaluated at the Stokes drag region, which gives:

$$\tau_p = \frac{v_t}{g} = \frac{\rho_s d_p^2}{18\mu_g} \tag{1.11}$$

The turbulence time scale is taken from the gas velocity and a relevant turbulence length scale, which is usually chosen to match with the particle size. This gives:

$$\tau_g = \frac{d_p}{|\mathbf{v}_g|} \tag{1.12}$$

The Stokes number for fluid-solid flow results:

$$St_{d_p} = \frac{\tau_p}{\tau_g} = \frac{\rho_s d_p |\mathbf{v}_g|}{18\mu_g} \tag{1.13}$$

Large values of Stokes number correspond to the coarsest and heaviest particles for which there is no effect of turbulent gas vortexes over the motion of the particles. That condition is known as inertial flow regime. A small Stokes number means that particles follow the movement of the gas flow just like tracers. This is the viscous flow regime. Figure (4) illustrates the inertial and viscous flow regimes, as well as the transitional flow regime, where the particles are affected by the gas turbulence but do not follow its stream lines. The figures for Stokes number are for a particular case (Hrenya and Sinclair, 1997).

In the current work a large Stokes number particulate is considered, so that no gas turbulence treatment is implemented (See section 3.3.2).

Figure 4: Stokes number in fluid-solid flow associated to the motion of a particle for a particular case

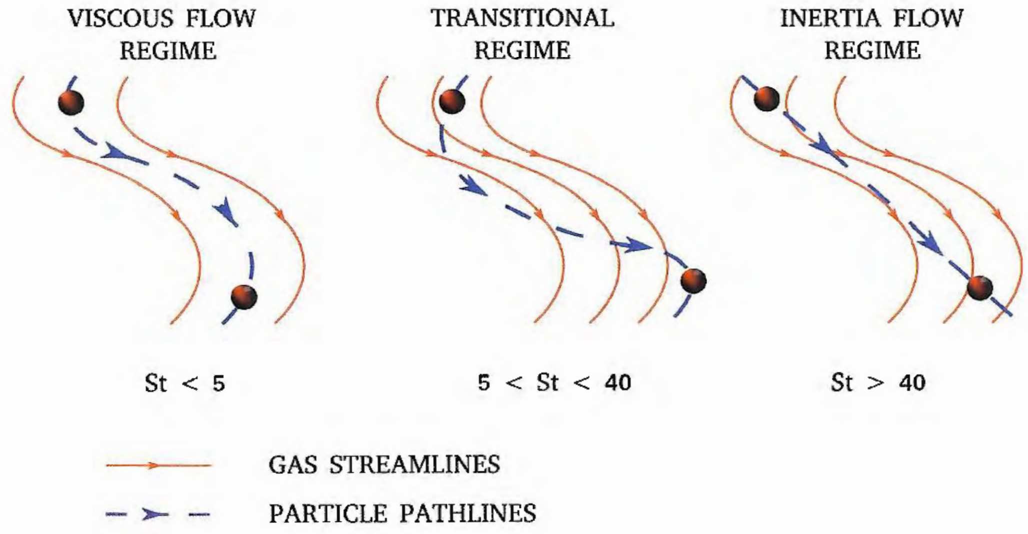

Source: Hrenya and Sinclair (1997).

Another relevant dimensionless group is the Froude number, which is particularly significant regarding gas-solid flow scaling.

A Froude number associated to the motion of a particle is usually defined as the ratio of the particle inertial force to the gravitational force acting on a particle.

$$Fr_{d_p} = \frac{v_t^2}{g d_p} \tag{1.14}$$

1.3 Modeling Fluidized Gas-Solid Flows

In gas-solid fluidization modeling, the gas phase is usually treated as a continuum. The particulate may be treated either by accounting for individual particles, parcels of particles, or a continuum phase that simulates its behavior. Depending on how the particulate is treated, the formulations are classified either as Euler-Lagrange (continuum for the gas, discrete particles for the particulate), or as Euler-Euler (gas and particulate treated as interpenetrating continua). Discrete Element Method (DEM), Lattice Boltzmann

Method (LBM) and Multi-phase Particle in Cell Method (MPPIC) are all Euler-Lagrange like formulations. The Two-fluid model (TFM) is an Euler-Euler like formulation. All of those formulations are widely practiced by researchers for different purposes, ranging from small domain fundamental investigations (mainly LBM, DEM and TFM) up to real domain large scale predictions (mainly MPPIC and TFM) (see, for instance, van der Hoef et al., 2006; Milioli and Milioli, 2011; Syamlal et al., 1993). Instead of advancing a comprehensive comparison among the various possibilities, as each of them have different merits, in this work it is just chosen to work with TFM. This approach is considered a very promising one for both large scale real simulations as well as small domain fundamental studies (Sundaresan, 2000) just like those developed in the current work.

1.3.1 Some fundamentals of the Euler-Euler approach

According to Ishii (1975), there are four groups of two-phase flows depending on the constituent phases: gas-solid flows, gas-liquid flows, solid-liquid flows and flows of two non-miscible liquids. Depending on the topology of the flow there are three groups: separated flows, mixed flows and dispersed flows. In this work the concern is turned to gas-solid dispersed flows. The two phases are modeled using equations for single phase flow with a moving boundary between the phases. Averaging procedures as space average, time-average and ensemble-average are usually applied to provide useful formulations.

An Euler-Euler hydrodynamic two-dimensional model for a two-fluid flow is developed consisting of two continuity equations and two momentum equations. Also closure laws are needed. There are three types of closure laws: topological laws describing the spatial distribution of phase-specific quantities, constitutive laws which describe physical properties of the phases, and transfer laws which describe interactions between the phases.

Euler-Euler formulations are founded on the very fundamental continuum hypothesis. The matter is a compound of elemental particles such as atoms and molecules. This concept brings inherently a discontinuity of the matter, because at the atomic or molecular level the matter is not a continuum. The assumption of continuum is valid when the length scale of analysis is larger compared with the dimensions of those elemental particles. The continuum hypothesis allows the description of fluid and solid flow properties using differential calculus to set governing equations and model a physical problem.

Continuum properties such as density and velocity become representative in any large enough volume element. When the length scale of the volume element is big enough to satisfy the continuum hypotheses, the quantity of elemental particles inside it is large, and any average properties of the particles become representative.

To formulate a two-fluid Euler-Euler hydrodynamic model, a control volume is set which is defined as a fixed space containing both the phases. Integral balances for mass and momentum are applied over this control volume. These balances provide local instantaneous equations for each phase and local instantaneous jump conditions which account for interactions between the phases at the interface.

The local instantaneous equations apply to both phases, each one of them required to be a continuum. Clearly, on a finite fraction of space there would be discontinuities in a phase owing to the presence of the other phase, and the local instantaneous equation can not be applied. To overcome that difficulty averaging procedures are applied, thereby defining interpenetrating continua where interface interactions are treated in average, as continuum field effects. Different averaging procedures may be applied (time, volume, ensemble averaging), which are usually assumed equivalent to each other (ergodicity hypothesis) (see, for instance, Enwald et al., 1996; Gidaspow, 1994).

1.3.2 Euler-Euler Two-fluid Multi-scale Modeling

The very complex set of conservative equations of the Euler-Euler two-fluid model can only be solved by numerical methods. Owing to computational limitations and to the huge volumes to be resolved, large scale simulations (LSS) are only feasible under very coarse numerical grids. At this scale of simulation the coarse grids filter any sub-grid effects. It is said that any meso-scale structures are filtered so that their effects over the macro-scale are lost. The formulation to be resolved in large scale simulations, frequently referred to as filtered formulation, requires sub-grid closures meant to recover coarse grid filtered effects. One way of recovering such effects, and thereby providing data for sub-grid correlation, is through the so called highly resolved simulations (HRS). Usually, in HRS, a refined grid is defined over domains matching a LSS coarse grid cell, so that smaller structures are captured. The concerning refined grid must be fine enough so that all structures are captured, down to the smallest (of about 10 particle diameters, according to Agrawall et al., 2001). Figure (5) illustrates both LSS and HRS domain and grids.

Figure 5: Multi-scale Modeling

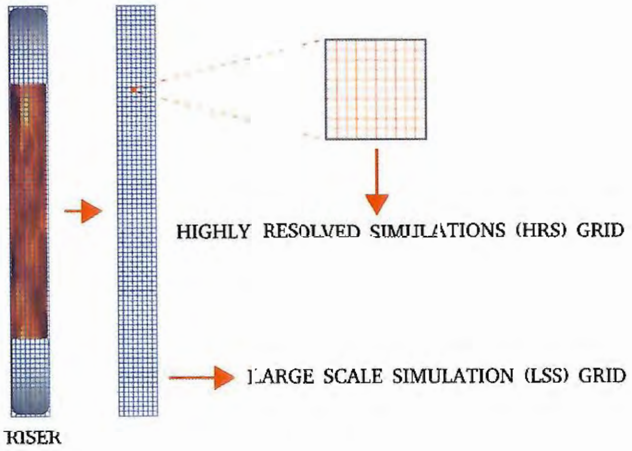
HIGHLY RESOLVED SIMULATIONS (HRS) GRID
LARGE SCALE SIMULATION (LSS) GRID
RISER

Source: Elaborated by the author.

EESC - USP
Biblioteca
CAMPUS DE S. CARLOS

2 MAIN LITERATURE REVIEW AND OBJECTIVES

Two-fluid models including suitable filtered closures represent the most promising next generation models for multiphase reactors and, in this context, the formulation of realistic filtered models is a great challenge ahead (Sundaresan, 2000). This particular issue has been addressed by a number of researchers on the basis of highly resolved computational experiments (or highly resolved simulations, HRS) with microscopic two-fluid modeling (Agrawal et al., 2001; Andrews IV et al., 2005; Igci et al., 2008; Igci and Sundaresan, 2011; Parmentier et al., 2012; Ozel et al., 2013; Milioli et al., 2013; Agrawal et al., 2013; Schneiderbauer and Pirker, 2014; Sarkar et al., 2016). Besides making it clear the real necessity for filtered models, those works suggest that filtered models so produced from highly resolved computational experiments do require continuous improvement as more and more realistic approaches are pursued. The filtered models are also called meso-scale models since they are generated from computational experiments under grid refinements that are expected to capture all the solid phase scales of the flow, so that filtered meso-scale data can be derived. In most cases, reduced domains are considered, which are extracted from the free stream in the core of the flow field, and periodic boundaries are applied. As periodic boundaries are applied, an extra gas phase pressure gradient is imposed in the vertical direction in order to impose a flow driving force. It is usual to consider an extra gas phase pressure gradient to exactly compensate the gravity acting on the gas-solid mixture. This idea is brought from fundamental studies on the instabilities that develop in gas-solid flows owing to inter-particle inelastic collisions, which ultimately lead to clustering (Goldhirsch et al., 1993; Tan and Goldhirsch, 1997). While those studies are valid for quasi-static conditions, where the particulate arranges itself in low velocity suspensions, it has been commonly assumed that the cluster formation mechanism that prevails is also relevant to any flow topology, from bubbling, to turbulent, to rapid gas-solid flows.

Following the above basic approach, Agrawal et al. (2001), Andrews IV et al. (2005), Igci et al. (2008), Igci et al. (2010), and Igci and Sundaresan (2011) developed highly resolved simulations and analyzed the behavior of filtered parameters like effective pressure and viscosity and effective drag coefficient. Agrawal et al. (2001) characterized the meso-scale of the gas-solid flow as comprised of solid coherent structures with dimensions from 10 to 100 times the particulate size. From their predictions the authors analyzed the behavior of filtered and effective dynamic viscosities and pressures of the solid phase. As observed by van der Hoef et al. (2006), Agrawal et al. (2001) showed that grid refinements of the order of 10 times the particulate size provided grid independent predictions for a particular case. They also showed that vertical boundary conditions of free slip, partial slip and periodic, do produce the same heterogeneous flow pattern. Andrews IV et al.

(2005) explicitly proposed ad hoc closures for the effective drag, viscosity and pressure of the solid phase. Igci et al. (2008) further extended the previous works of Agrawal et al. (2001) and Andrews IV et al. (2005), and showed that the filtered predictions depend on the sub-grid filter size. A posterior work also showed the filtered predictions to depend on the distance from walls (Igci et al., 2010). Further extending the work reported in Igci et al. (2008), Igci and Sundaresan (2011) produced correlations for the filtered effective drag, pressure and viscosity of the solid phase, as a function of filter size and filtered solid volume fraction. The effective drag coefficient was expressed in the form of a drag coefficient correction relating the actual effective drag coefficient to the filtered micro-scale drag coefficient, as previously done, for instance, by Zhang and VanderHeyden (2002). Igci et al. (2012) tested the correlations presented in Igci and Sundaresan (2011), including the wall corrections proposed in Igci et al. (2010), in coarse grid simulations of a riser flow. The comparisons against empirical data showed qualitative agreement, while quantitative differences still remained.

Following the same basics of the previous works, Parmentier et al. (2012) proposed a similar approach to deal with the filtered effective drag, except they did not apply periodic boundaries but a small 2D bubbling bed configuration. Their correlations for the drag coefficient correction were alike those proposed in Igci and Sundaresan (2011), except for the inclusion of a macro-scale length scale in the filter size dependence of the drag coefficient correction. They also included a coarse grid dynamical adjustment analogous to the dynamic correction usually applied in large eddy simulation of turbulent flows. A test of their drag coefficient correction correlation in a coarse grid simulation of a bubbling bed set up recovered the correct bed expansion which came out from a highly resolved simulation. The model remained to be tested for more dilute flow configurations such as circulating fluidized beds. Ozel et al. (2013) extended the work of Parmentier et al. (2012) by incorporating vertical periodic boundaries over 3D bubbling bed conditions, and also by extending the development to include stresses analyses as done by Agrawal et al. (2001). Their conclusions were similar to those of Parmentier et al. (2012).

In the works cited so far (Agrawal et al., 2001; Andrews IV et al., 2005; Igci et al., 2008; Igci and Sundaresan, 2011; Parmentier et al., 2012; Ozel et al., 2013) filtered parameters have been correlated to filter size and filtered solid volume fraction. It so happens that different patterns, ranging from very homogeneous to very heterogeneous, may occur for any particular values of filter size and filtered solid fraction. In order to account for the heterogeneity of the flow, Milioli et al. (2013) introduced an additional independent variable in filtered parameter correlation (named 2nd marker, while the solid volume fraction was named 1st marker). Models for effective pressures and viscosities were proposed in analogy with the Smagorinsky's turbulence viscosity model, thereby introducing the filtered scalar shear rate as 2nd marker. Also, a model for the effective drag coefficient correction was proposed including the filtered slip velocity as a 2nd marker.

Ozarkar et al. (2015) applied the sub-grid models of Milioli et al. (2013) to a large scale simulation of a bubbling fluidized bed, and compared results to experiment. They found a very good agreement between experiment and predictions for both bed expansion and pressure drop through the height of the bed. Schneiderbauer and Pirker (2014) followed the same path as Milioli et al. (2013), and found similar results. Agrawal et al. (2013) extended the work of Milioli et al. (2013) by also proposing filtered models for the mass/heat diffusivity coefficient and for the interphase mass/heat transfer coefficient, respectively accounting for the filtered scalar shear rate and the filtered slip velocity as 2nd marker.

Sarkar et al. (2016) developed new sub-grid models following the work of Milioli et al. (2013), except that based on 3D highly resolved simulations. Similar behavior of the effective drag coefficient correction and effective pressures and viscosities were observed, with some quantitative differences. Regarding the effective pressures and viscosities, a correlation to the filtered slip velocity as 2nd marker was also observed which was not seen on the previous results of Milioli et al. (2013). In addition to sub-grid model proposition, Sarkar et al. (2016) also developed a validation step by comparing predictions of a large scale simulation against experiment for a bubbling bed situation. A very good agreement between predictions and experiments was found for both bed expansion and pressure drop through the height of the bed.

2.1 Objectives

Literature presents sub-grid analyses of gas-solid flows on the basis of highly resolved simulations with microscopic two-fluid modeling. Except from a few works under bubbling bed conditions, most of the research has been carried out under suspension like conditions in periodic domains. This renders flow conditions at low Reynolds numbers which, nevertheless, is assumed to be relevant for any gas-solid flow no matter its macro-scale topology.

This assumption is consistent with the scale separation hypothesis which, nevertheless, does not hold for gas-solid riser flows. In this work, having in view the notorious lack of separation of scales in those flows, an analysis was advanced which also accounted for the effects of the macro-scale over sub-grid filtered parameters.

In recent works, relevant filtered parameters related to effective drag and stresses have been evaluated as for their relation to filtered solid volume fraction and filtered slip velocity. In this work the analysis was extended by also relating those relevant filtered parameters to macro-scale parameters, namely the domain average solid volume fraction and the domain average gas flow Reynolds number. In addition to the usual suspension like conditions, a range of domain average gas Reynolds numbers was imposed together with a range of domain average solid volume fractions. Those ranges were set for usual riser flow conditions, for a high Stokes number particulate. All the simulations were performed with the microscopic two-fluid model of the open source code MFIX.

3 METHODOLOGY

In two-fluid modeling all the phases, no matter fluid or particulate, are treated as inter-penetrating dispersed continua in thermodynamic equilibrium (Anderson and Jackson, 1967; Ishii, 1975; Drew, 1971 and 1983; Delhaye, 1974 and 1981; Gidaspow, 1994; Enwald et al., 1996). The hydrodynamic two-fluid models comprise a set of average mass and momentum conservative equations plus closure laws for stress tensors, viscosities, pressures and drag. In this research, highly resolved simulations (HRS) are performed in order to produce filtered data that are required for the development of sub-grid filtered closures, which are needed in two-fluid large scale simulations (LSS) of gas-solid flows in fluidized beds. LSS is performed using the so called filtered models, that require sub-grid closures, while HRS is performed using the so called microscopic models, that require micro-scale closures.

Both the concerning formulations, the microscopic (for HRS) and the filtered (for LSS) are presented next. While the filtered formulation is not resolved in the current work, it is also presented so as to show exactly what sub-grid parameters are required, and should therefore be derived from HRS.

3.1 Microscopic Two-Fluid Model

The gas-solid two-fluid model presents variations for closure relations (Syamlal et al., 1993). The micro-scale closures for the solid phase, that are required by the so called microscopic formulation of the two-fluid model, are established by applying the kinetic theory of granular flows (KTGF) (Bagnold, 1954; Jenkins and Savage, 1983; Lun et al., 1984; Gidaspow, 1994), where solid phase micro-scale properties are derived as a function of a granular temperature determined from a pseudo thermal energy balance. The microscopic formulation of the two-fluid model is presented next. The correlation of Wen and Yu (1966) is taken as the micro-scale closure for drag. Other possible interface forces between the phases are not accounted for, as drag is recognized as the dominant one.

The conservation equations of continuity and momentum for both phases are:

$$\frac{\partial}{\partial t}(\rho_g \phi_g) + \nabla \cdot (\rho_g \phi_g \mathbf{v}_g) = 0 \tag{3.1}$$

$$\frac{\partial}{\partial t}(\rho_s \phi_s) + \nabla \cdot (\rho_s \phi_s \mathbf{v}_s) = 0 \tag{3.2}$$

$$\frac{\partial}{\partial t}\left(\rho_g \phi_g \mathbf{v}_g\right) + \nabla \cdot \left(\rho_g \phi_g \mathbf{v}_g \mathbf{v}_g\right) = -\phi_g \nabla \cdot \boldsymbol{\sigma}_g - \mathbf{M}_I + \rho_g \phi_g \mathbf{g} \tag{3.3}$$

$$\frac{\partial}{\partial t}\left(\rho_s \phi_s \mathbf{v}_s\right) + \nabla \cdot \left(\rho_s \phi_s \mathbf{v}_s \mathbf{v}_s\right) = -\nabla \cdot \boldsymbol{\sigma}_s - \phi_s \nabla \cdot \boldsymbol{\sigma}_g + \mathbf{M}_I + \rho_s \phi_s \mathbf{g} \tag{3.4}$$

The microscopic model also requires a conservation equation of granular pseudo-thermal energy (PTE) (Lun et al., 1984; Gidaspow, 1994) to be resolved:

$$\frac{3}{2}\left[\frac{\partial}{\partial t}\left(\rho_s \phi_s \Theta\right) + \nabla \cdot \left(\rho_s \phi_s \mathbf{v}_s \Theta\right)\right] = -\boldsymbol{\sigma}_s : \nabla \mathbf{v}_s + \nabla \cdot \left(\kappa_s \nabla \Theta\right) + \Gamma_{slip} - \mathbf{J}_{coll} - \mathbf{J}_{vis} \tag{3.5}$$

Finally, the volumetric continuity requires that:

$$\phi_g + \phi_s = 1 \tag{3.6}$$

The deviatoric stress tensor for both phases (for $\ell = g, s$) is given by:

$$\boldsymbol{\sigma}_\ell = P_\ell \boldsymbol{I} - \boldsymbol{\tau}_\ell \tag{3.7}$$

Applying the divergence operator to the stress tensor in equation (3.7) gives:

$$\nabla \cdot \boldsymbol{\sigma}_\ell = \nabla P_\ell - \nabla \cdot \boldsymbol{\tau}_\ell \tag{3.8}$$

Considering hypotheses of isotropic and Newtonian fluid for both phases, it comes that:

$$\boldsymbol{\sigma}_\ell = \left[P_\ell - \left(\lambda_\ell + \frac{2}{3}\mu_\ell\right)(\nabla \cdot \mathbf{v}_\ell)\right]\mathbf{I} - 2\mu_\ell \mathbf{s}_\ell \tag{3.9}$$

The strain rate tensor due to viscous plus pressure effects is defined by:

$$\mathbf{s}_\ell = \frac{1}{2}\left[\nabla \mathbf{v}_\ell + (\nabla \mathbf{v}_\ell)^T\right] - \frac{1}{3}(\nabla \cdot \mathbf{v}_\ell)\,\mathbf{I} \tag{3.10}$$

For the gas phase in an isothermal flow the dynamic viscosity is constant ($\mu_g =$ constant), and following the Stokes hypothesis the second coefficient of viscosity is made null ($\lambda_g = 0$). The viscous stresses of gas phase are given by:

$$\boldsymbol{\tau}_g = \mu_g\left(\nabla \mathbf{v}_g + (\nabla \mathbf{v}_g)^T\right) \tag{3.11}$$

The viscous stresses of the solid phase are given by:

$$\boldsymbol{\tau}_s = \mu_s\left(\nabla \mathbf{v}_s + (\nabla \mathbf{v}_s)^T\right) + \lambda_s(\nabla \cdot \mathbf{v}_s)\,\mathbf{I} \tag{3.12}$$

Then equations (3.3), (3.4) and (3.5) can be rewritten respectively as:

$$\frac{\partial}{\partial t}(\rho_g \phi_g \mathbf{v}_g) + \nabla \cdot (\rho_g \phi_g \mathbf{v}_g \mathbf{v}_g) = -\phi_g \nabla P_g + \phi_g \nabla \cdot \boldsymbol{\tau}_g - \mathbf{M}_I + \rho_g \phi_g \mathbf{g} \tag{3.13}$$

$$\frac{\partial}{\partial t}(\rho_s \phi_s \mathbf{v}_s) + \nabla \cdot (\rho_s \phi_s \mathbf{v}_s \mathbf{v}_s) = -\nabla P_s + \nabla \cdot \boldsymbol{\tau}_s - \phi_s(\nabla P_g - \nabla \cdot \boldsymbol{\tau}_g) + \mathbf{M}_I + \rho_s \phi_s \mathbf{g} \tag{3.14}$$

$$\frac{3}{2}\left[\frac{\partial}{\partial t}(\rho_s\phi_s\Theta)+\nabla\cdot(\rho_s\phi_s\mathbf{v}_s\Theta)\right]=-\left(P_s\mathbf{I}+\boldsymbol{\tau}_s\right):\nabla\mathbf{v}_s+\nabla\cdot(\kappa_s\nabla\Theta)+\Gamma_{slip}-\mathbf{J}_{coll}-\mathbf{J}_{vis} \tag{3.15}$$

Equations (3.13) to (3.15) require closures for stresses related parameters which are trivial for the gas phase. The closures for stresses in the solid phase are developed next, together with closures for drag.

3.1.1 Microscopic closures for solid phase stresses

The microscopic closures for stresses in the solid phase are derived from the Kinetic Theory of Granular Flows (KTGF) (Lun et al., 1984), which is an analogy with the kinetic theory of dense gases.

The KTGF theory is based on many studies such as the work of Jenkins and Savage (1983) among others.

The flow of granular materials is modeled for dilute and dense concentrations of solids accounting for kinetic and collisional contributions as mechanisms of transport of momentum and energy.

The main assumptions for developing this granular flow theory are:

- The granular material is composed of smooth, hard, inelastic, uniform and spherical particles.
- Collisions are the principal mechanism of transport of momentum and energy.
- Collisions are considered to be almost elastic, so that $1-e \ll 1$, where e is a collisional restitution coefficient.

On the basis of KTGF, Lun et al. (1984) developed a set of relations describing properties of particulates treated as a continuum, which are used as closures in microscopic two-fluid models for gas-solid flows.

The dynamic viscosity (μ_s) and the second coefficient of viscosity (bulk viscosity) of the solid phase (λ_s) are given by:

$$\mu_s=\frac{(2+\alpha)}{3}\left[\frac{\xi^*}{\mathrm{g}_0\eta(2-\eta)}\left(1+\frac{8}{5}\phi_s\eta\mathrm{g}_0\right)\left(1+\frac{8}{5}\eta(3\eta-2)\phi_s\mathrm{g}_0\right)+\frac{6}{5}\eta\mu_b\right] \tag{3.16}$$

$$\lambda_s = \eta\mu_b - \frac{2}{3}\mu_s \tag{3.17}$$

where:

$$\mu_b = \frac{256\xi\phi_s^2 \mathbf{g}_0}{5\pi} \tag{3.18}$$

$$\xi^* = \frac{\xi}{1 + \dfrac{2\beta\xi}{(\rho_s\phi_s)^2 \mathbf{g}_0 \Theta}} \tag{3.19}$$

$$\xi = \frac{5\rho_s d_p (\pi\Theta)^{1/2}}{96} \tag{3.20}$$

$$\alpha = 1.6 \tag{3.21}$$

$$\eta = \frac{1+e}{2} \tag{3.22}$$

The radial distribution function is given by:

$$\mathbf{g}_0 = \frac{1}{1 - \left(\dfrac{\phi_s}{\phi_{s,max}}\right)^{1/3}} \tag{3.23}$$

where:

$$\phi_{s,max} = 0.65 \tag{3.24}$$

The pressure of the solid phase is given by (Gidaspow, 1994):

$$P_s = \rho_s\phi_s \left(1 + 4\eta\phi_s \mathbf{g}_0\right)\Theta \tag{3.25}$$

The closures for Equation (3.15) are as follows.

The granular thermal conductivity is given by:

$$\kappa_s = \frac{\gamma^*}{\mathrm{g}_0}\left[\left(1+\frac{12}{5}\eta\phi_s\mathrm{g}_0\right)\left(1+\frac{12}{5}\eta^2(4\eta-3)\phi_s\mathrm{g}_0\right)+\frac{64}{25\pi}(41-33\eta)\eta^2\phi_s^2\mathrm{g}_0^2\right] \tag{3.26}$$

where:

$$\gamma^* = \frac{\gamma}{1+\dfrac{6\beta\gamma}{5(\rho_s\phi_s)^2\mathrm{g}_0\Theta}} \tag{3.27}$$

$$\gamma = \frac{75\rho_s d_p(\pi\Theta)^{1/2}}{48\eta(41-33\eta)} \tag{3.28}$$

The rate of production of granular energy due to gas-particle slip is given by:

$$\Gamma_{slip} = \frac{81\phi_s\mu_g^2|\mathbf{v}_g-\mathbf{v}_s|^2}{\mathrm{g}_0 d_p^3\rho_s(\pi\Theta)^{1/2}} \tag{3.29}$$

The rate of dissipation of granular energy by collisional and viscous damping are given by:

$$\mathbf{J}_{coll} = \frac{48}{\pi 1/2}\eta(1-\eta)\frac{\rho\phi_s^2}{d_p}\mathrm{g}_0\Theta^{3/2} \tag{3.30}$$

$$\mathbf{J}_{vis} = 3\beta\Theta \tag{3.31}$$

3.1.2 Microscopic closures for drag

Momentum exchanges between the gas and the solid phases may happen due to a number of different interface forces. Descriptions of a variety of such forces may be found in Gidaspow (1994) and Enwald et al. (1996), for instance. Even though interface mechanisms like lift and virtual mass, for instance, may be of some relevance, it is recognized that the stationary drag is the most relevant interface force to account for in fluidized gas-solid flows. Most of the literature relevant to the present work, which has been reported in Section 2, considers drag as the only relevant mechanism for microscopic momentum exchanges between phases. The present work follows the same path.

The drag effect is actually the *driving force* for the motion of solid particles and clusters of particles in gas-solid fluidization.

Drag is a surface force that acts in the opposite direction to the relative motion of particle and fluid. So it depends on the magnitude of the relative or slip velocity:

$$\mathbf{F}_d \equiv \mathbf{F}_d(\mathbf{v}_r) \tag{3.32}$$

It is a resistive force acting on the particle against its movement, which may be assumed as comprised of two components (Faber, 1995). The first is the form-drag which is due to the pressure stress. The second is the friction-drag, which is related to the fluid viscous stress.

The drag coefficient is usually defined as the ratio of the friction drag force per unit area to the dynamic pressure based on the relative velocity:

$$c_D = \frac{\frac{|\mathbf{F}_d|}{A}}{\frac{1}{2}\rho_g|\mathbf{v}_r|^2} \tag{3.33}$$

Experiments have shown a dependence of the drag coefficient on the Reynolds number $c_D \equiv c_D(Re)$, shape and orientation of the particles. For very small Reynolds numbers ($Re < 0.2$) the friction drag is bigger than the form drag, and for values of ($0.2 < Re < 1000$) form drag may be more significant than the friction drag.

A balance of momentum over the steady state motion of a spherical particle dropping in a quiescent infinite gas expanse provides an expression for a drag coefficient given by (Ranade, 2002; Clift et al., 1978):

$$c_D = \frac{4}{3}\frac{d_p}{\rho_g}\frac{\rho_s - \rho_g}{|\mathbf{v}_t|^2} \tag{3.34}$$

Where $|\mathbf{v}_t|$ is the free fall terminal velocity of the particle. Considering the fluid also in motion, the same equation prevails providing the terminal velocity is replaced with the modulus of the slip velocity, that is:

$$c_D = \frac{4}{3}\frac{d_p}{\rho_g}\frac{\rho_s - \rho_g}{|\mathbf{v}_{slip}|^2} \tag{3.35}$$

In order to account for the drag over an individual particle immersed in an homogeneous multiparticle system, Wen and Yu (1966) proposed the following corrected coefficient:

$$c_D^* = (1 - \phi_s)^{-4.7} c_D \tag{3.36}$$

While this correction suits homogeneous systems, it does not suit an heterogeneous situation such as that in riser flows. See figure (6).

Figure 6: Different topologies in gas-solid flow

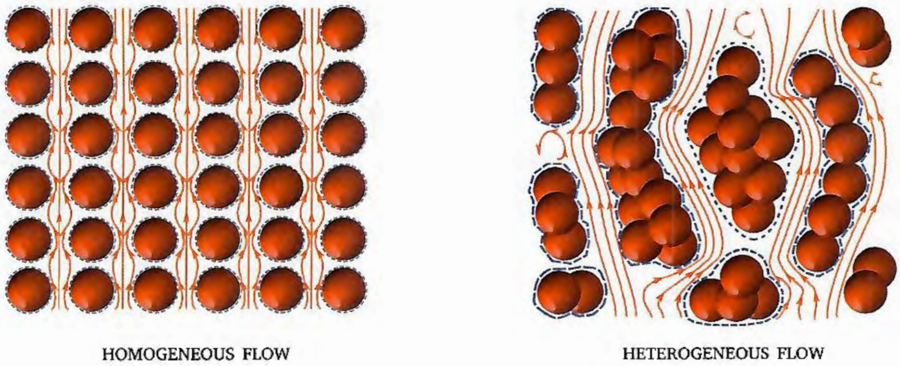

Source: Elaborated by the author.

This correction does not account for the effects of cluster formation and evolution over the drag. The presence of clusters decreases the value of the drag coefficient. Also, Reynolds number and concentration of solids greatly affect flow topology (clusters), thereby imposing a strong effect on drag.

Experiment shows that the drag coefficient for heterogeneous flows is much smaller than that for homogeneous flows (Wen and Yu, 1966).

In homogeneous flows there is a high contact surface between the fluid and the particles, and the drag results relatively high. In heterogeneous flows the clustering imposes bypasses for the gas, diminishing the contact surface, and the drag results relatively low.

Gidaspow and Ettehadieh (1983) proposed a widely accepted revised correction on c_D which is better suited to the solid concentrations typical of riser flows. It gives:

$$c_D^* = (1 - \phi_s)^{-2.65} c_D \tag{3.37}$$

Most of the literature in highly resolved simulations of gas-solid flows that are relevant to the present work (see Section 2) apply a drag model derived from Wen and Yu's developments, also accounting for Gidaspow and Ettehadieh's correction. The same path is followed in the present work.

Following the usual procedure the drag force of the gas over the solid phase per unit volume, as it appears in Equations (3.13) and (3.14), is given by:

$$\mathbf{M}_I = \beta(\mathbf{v}_g - \mathbf{v}_s) \tag{3.38}$$

Where the drag coefficient β is given by:

$$\beta = \frac{3}{4} c_D \frac{\rho_g \phi_s \phi_g \left|\mathbf{v}_g - \mathbf{v}_s\right|}{(d_p \epsilon_p)} (\phi_g)^{-2.65} \tag{3.39}$$

The single particle drag coefficient is brought from Rowe (1961):

$$c_D = \frac{24}{Re_p}\left(1 + 0.15 Re_p^{0.687}\right) \qquad \text{for} \qquad Re_p < 1000 \tag{3.40}$$

$$c_D = 0.44 \qquad \text{for} \qquad Re_p \geq 1000 \tag{3.41}$$

Where the Reynolds number based on particle size is given by:

$$Re_p = \frac{\left|\mathbf{v}_g - \mathbf{v}_s\right| d_p \rho_g \phi_g}{\mu_g} \tag{3.42}$$

3.2 Filtered Two-Fluid Model

A formulation of the hydrodynamic filtered two-fluid model applied to gas-solid flows is presented next alongside with the filtered closures that are required. The filtered formulation is obtained by applying a volumetric filter over the microscopic model equations, and then a Favre mass weighed filter, also defining effective stresses and drag as appropriate.

The filtered equations are as follows:

$$\frac{\partial}{\partial t}\left(\rho_g \overline{\phi}_g\right) + \nabla \cdot \left(\rho_g \overline{\phi}_g \tilde{\mathbf{v}}_g\right) = 0 \tag{3.43}$$

$$\frac{\partial}{\partial t}\left(\rho_s \overline{\phi}_s\right) + \nabla \cdot \left(\rho_s \overline{\phi}_s \tilde{\mathbf{v}}_s\right) = 0 \tag{3.44}$$

$$\frac{\partial}{\partial t}\left(\rho_g \overline{\phi}_g \tilde{\mathbf{v}}_g\right) + \nabla \cdot \left(\rho_g \overline{\phi}_g \tilde{\mathbf{v}}_g \tilde{\mathbf{v}}_g\right) = -\overline{\phi}_g \nabla \cdot \tilde{\boldsymbol{\sigma}}_g - \nabla \cdot \boldsymbol{\tau}'_g - \left(\mathbf{B}'_{gs} + \overline{\mathbf{M}}_I\right) + \rho_g \overline{\phi}_g \mathbf{g} \tag{3.45}$$

$$\frac{\partial}{\partial t}\left(\rho_s \overline{\phi}_s \tilde{\mathbf{v}}_s\right) + \nabla \cdot \left(\rho_s \overline{\phi}_s \tilde{\mathbf{v}}_s \tilde{\mathbf{v}}_s\right) = -\nabla \cdot \overline{\boldsymbol{\sigma}}_s - \nabla \cdot \boldsymbol{\tau}'_s - \overline{\phi}_s \nabla \cdot \tilde{\boldsymbol{\sigma}}_s + \left(\mathbf{B}'_{gs} + \overline{\mathbf{M}}_I\right) + \rho_s \overline{\phi}_s \mathbf{g} \tag{3.46}$$

The filtered volumetric continuity is given by:

$$\overline{\phi}_g + \overline{\phi}_s = 1 \tag{3.47}$$

The divergence of the filtered stress tensor for both phases (for $\ell = g, s$) gives:

$$\nabla \cdot \tilde{\boldsymbol{\sigma}}_\ell = \nabla \tilde{P}_\ell - \nabla \cdot \tilde{\boldsymbol{\tau}}_\ell \tag{3.48}$$

$$\nabla \cdot \overline{\boldsymbol{\sigma}}_\ell = \nabla \overline{P}_\ell - \nabla \cdot \overline{\boldsymbol{\tau}}_\ell \tag{3.49}$$

The filtered deviatoric stress tensor for the gas phase is given by:

$$\tilde{\boldsymbol{\sigma}}_g = P_{fil,g}\mathbf{I} - 2\mu_{fil,g}\tilde{\mathbf{S}}_g \tag{3.50}$$

where the filtered gas pressure and filtered gas viscosities are:

$$P_{fil,g} = \widetilde{P}_g - \left(\lambda_g + \frac{2}{3}\mu_g\right)(\nabla \cdot \widetilde{\mathbf{v}}_g) \tag{3.51}$$

$$\mu_{fil,g} = \mu_g \tag{3.52}$$

$$\lambda_g = 0 \tag{3.53}$$

$\widetilde{P}_g$ comes straight from the solution of the conservative Equations (3.43) to (3.46). The filtered deviatoric stress tensor for the solid phase is given by:

$$\overline{\boldsymbol{\sigma}}_s = P_{fil,s}\mathbf{I} - 2\mu_{fil,s}\widetilde{\mathbf{s}}_s \tag{3.54}$$

The filtered solid pressure and filtered solid dynamic viscosity are given by:

$$P_{fil,s} = \overline{P}_s - \overline{\left(\lambda_s + \frac{2}{3}\mu_s\right)(\nabla \cdot \mathbf{v}_s)} \tag{3.55}$$

$$\mu_{fil,s} = \overline{\mu}_s \tag{3.56}$$

$\overline{\mu}_s$ and $\overline{P}_s$ come from applying filtered parameters over Equations (3.16) and (3.25), respectively.

In Equations (3.50) and (3.54) the filtered strain rate tensor (for $\ell = g, s$) is given by:

$$\widetilde{\mathbf{s}}_\ell = \frac{1}{2}\left[\nabla\widetilde{\mathbf{v}}_\ell + (\nabla\widetilde{\mathbf{v}}_\ell)^T\right] - \frac{1}{3}(\nabla \cdot \widetilde{\mathbf{v}}_\ell)\mathbf{I} \tag{3.57}$$

The Reynolds-like stresses (for $\ell = g, s$) are defined by:

$$\boldsymbol{\tau}'_\ell = \rho_\ell \overline{\phi}_\ell \left(\widetilde{\mathbf{v}_\ell \mathbf{v}_\ell} \right) - \rho_\ell \overline{\phi}_\ell \widetilde{\mathbf{v}}_\ell \widetilde{\mathbf{v}}_\ell \tag{3.58}$$

In analogy with the viscous stresses, the Reynolds-like stresses may also be expressed in terms of effective parameters for pressures and viscosities (just like the usual analogy in turbulence regarding viscous and Reynolds stresses, hypothesis of Boussinesq).

$$\boldsymbol{\tau}'_\ell = P_{eff,\ell}\mathbf{I} - 2\mu_{eff,\ell}\widetilde{\mathbf{s}}_\ell \tag{3.59}$$

Assuming isotropy, the normal components of the Reynolds-like stresses define the effective pressure as:

$$P_{eff,\ell} = \frac{1}{3}\mathbf{tr}\left(\boldsymbol{\tau}'_\ell\right) \tag{3.60}$$

The shear components of the Reynolds-like stresses define the effective viscosity as:

$$\boldsymbol{\tau}'_{shear,\ell} = 2\mu_{eff,\ell}\widetilde{\mathbf{s}}_{shear,\ell} \tag{3.61}$$

where the shear components of the filtered strain rate tensor (for $\ell = g, s$) are given by:

$$\widetilde{\mathbf{s}}_{shear,\ell} = \frac{1}{2}\left(\nabla\widetilde{\mathbf{v}}_\ell + \left(\nabla\widetilde{\mathbf{v}}_\ell\right)^T\right) \tag{3.62}$$

Assuming isotropy, the effective viscosity results:

$$\mu_{eff,\ell} = \frac{|\boldsymbol{\tau}'_{shear,\ell}|}{2|\overline{\mathbf{S}}_{shear,\ell}|} \tag{3.63}$$

Accounting for the previous developments, Equations (3.45) and (3.46) can be rewritten as:

$$\frac{\partial}{\partial t}\left(\rho_g\overline{\phi}_g\widetilde{\mathbf{v}}_g\right)+\nabla\cdot\left(\rho_g\overline{\phi}_g\widetilde{\mathbf{v}}_g\widetilde{\mathbf{v}}_g\right) = -\overline{\phi}_g\left(\nabla\widetilde{P}_g - \nabla\cdot\widetilde{\boldsymbol{\tau}}_g\right)-\nabla\cdot\boldsymbol{\tau}'_g-\left(\mathbf{B}'_{gs}+\overline{\mathbf{M}}_I\right)+\rho_g\overline{\phi}_g\mathbf{g} \tag{3.64}$$

$$\begin{aligned}\frac{\partial}{\partial t}\left(\rho_s\overline{\phi}_s\widetilde{\mathbf{v}}_s\right)+\nabla\cdot\left(\rho_s\overline{\phi}_s\widetilde{\mathbf{v}}_s\widetilde{\mathbf{v}}_s\right) = &-\left(\nabla\overline{P}_s - \nabla\cdot\overline{\boldsymbol{\tau}}_s\right)-\nabla\cdot\boldsymbol{\tau}'_s\\ &-\overline{\phi}_s\left(\nabla\widetilde{P}_g - \nabla\cdot\widetilde{\boldsymbol{\tau}}_g\right)+\left(\mathbf{B}'_{gs}+\overline{\mathbf{M}}_I\right)+\rho_s\overline{\phi}_s\mathbf{g}\end{aligned} \tag{3.65}$$

In the above equations, $\overline{\mathbf{M}}_I$ is the filtered drag force of the gas over the solid phase, given by:

$$\overline{\mathbf{M}}_I = \overline{\beta\left(\mathbf{v}_g - \mathbf{v}_s\right)} \tag{3.66}$$

and $\mathbf{B}'_{gs}$ is the fluctuation of the buoyancy force of the gas over the solid phase, given by:

$$\mathbf{B}'_{gs} = -\left[\left(\nabla\overline{P}_g - \nabla\cdot\overline{\boldsymbol{\tau}}_g\right) - \left(\nabla\widetilde{P}_g - \nabla\cdot\widetilde{\boldsymbol{\tau}}_g\right)\right] \tag{3.67}$$

$(\mathbf{B}'_{gs} + \overline{\mathbf{M}}_I)$ in Equations (3.45) and (3.46) is defined as an effective interface interaction force. This generalized force is usually expressed as proportional to the filtered slip velocity:

$$\beta_{\mathbf{eff}}\left(\widetilde{\mathbf{v}}_g - \widetilde{\mathbf{v}}_s\right) = \overline{\beta\left(\mathbf{v}_g - \mathbf{v}_s\right)} - \left[\left(\nabla\overline{P}_g - \nabla\cdot\overline{\boldsymbol{\tau}}_g\right) - \left(\nabla\widetilde{P}_g - \nabla\cdot\widetilde{\boldsymbol{\tau}}_g\right)\right] \tag{3.68}$$

From this equation, the effective coefficient (called here effective drag force coefficient owing to the predominance of drag in the concerning composition of forces) results:

$$\beta_{\mathbf{eff}} = \frac{\overline{\beta\left(\mathbf{v}_g - \mathbf{v}_s\right)}}{\left(\tilde{\mathbf{v}}_g - \tilde{\mathbf{v}}_s\right)} - \frac{\left[\left(\nabla \overline{P}_g - \nabla \cdot \overline{\boldsymbol{\tau}}_g\right) - \left(\nabla \tilde{P}_g - \nabla \cdot \tilde{\boldsymbol{\tau}}_g\right)\right]}{\left(\tilde{\mathbf{v}}_g - \tilde{\mathbf{v}}_s\right)} \tag{3.69}$$

Also, a drag coefficient correction H may be defined by relating the effective drag coefficient to the filtered micro-scale drag coefficient:

$$H = 1 - \frac{\beta_{\mathbf{eff}}}{\overline{\beta}} \tag{3.70}$$

$\overline{\beta}$ comes from applying filtered parameters over Equation (3.39)

The above filtered formulation requires sub-grid models for H, $P_{fil,s}$, $\mu_{fil,s}$, $P_{eff,\ell}$ and $\mu_{eff,\ell}$ (for $\ell = g, s$). It is the aim of this work to provide information useful for the accurate correlation of those parameters to relevant independent variables (in the present case, macro-scale independent variables associated to flow topology).

3.3 Numerical Simulations

In this work highly resolved simulations with microscopic two-fluid modeling are performed for predicting the meso-scale of gas-solid dilute fluidized flows. As quite refined grids are needed, no real domain can be resolved, but only representative parts of it. One way of performing such a partial domain simulation is by applying periodic boundaries. In this procedure entrance/exit parallel boundaries are made to match each other, so that the flow that enters through a given boundary is exactly the same the exits through its parallel match. This procedure is followed in this work, and the domain is defined as a 2D periodical square. While 3D simulations are not carried out owing to computational limitations, the performed 2D simulations are quite suitable in view of the qualitative behavior analysis that is pursued.

As illustrated in Figure (7), the behavior of any domain average variable evolving through time in a periodic domain simulation shows two main stages. In a first stage the system initiates from its initial condition and evolves until achieving a second stage, where the variable keeps fluctuating around a well defined mean value. This is the so called statistical steady state regime.

In this work all the analyses are performed inside the statistical steady state regime, where the domain average solid volume fraction and the domain average gas Reynolds number are imposed constants through initial and boundary conditions.

Figure 7: Typical behavior of the domain average of any variable while simulating in a periodic domain.

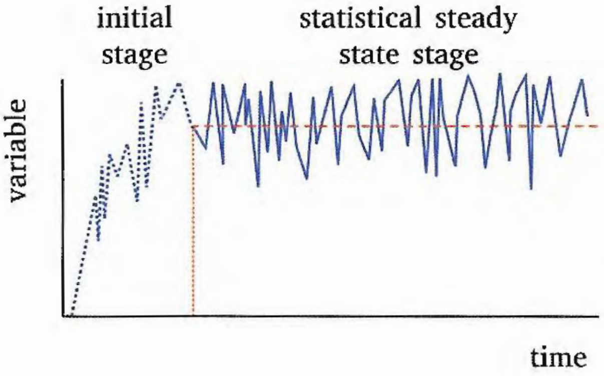

Source: Elaborated by the author.

3.3.1 Numerical Procedure

The complex system of coupled non-linear partial differential equations of the two-fluid models can only be solved by numerical procedures. There are different options available for that, such as the commercial codes CFX and Fluent, and the free open code MFIX. All of those codes are stable, and widely used to solve two-phase flows under two-fluid modeling. Numerical models in commercial appliances like CFX and Fluent do not allow access to the source code, thereby preventing any modifications on formulations and boundary conditions. In this research the MFIX code is used since it is free, and since it allows for code modifications when they are required, a feature that may be quite useful in future investigations.

MFIX (Multiphase Flow with Interphase eXchanges) (Syamlal et al., 1993) is a numerical code specific for gas-solid flow simulations, which includes two-fluid based formulations, developed and made available by NETL (National Energy Technology Laboratory, DOE-USA). Its source code is open so that any modifications and implementations on both formulation and boundary conditions are allowed. MFIX is a FORTRAN written parallelized code. The governing equations in MFIX's two-fluid model are discretized through the finite volume method. The resulting numerical model is solved through a point by point numerical technique. Diffusive terms are discretized following the second order central differencing scheme. For advection terms there are various alternative discretizing methods, ranging from the first order upwind method up to higher order TVD procedures.

da Silva, Cabezas-Gómez and Milioli (2006) tested some of the discretization procedures for advective terms in MFIX, and found the Superbee procedure to provide the best results for the simulation of a particular riser flow. The Superbee procedure is followed in the current work. The pressure-velocity coupling is solved through the SIMPLE algorithm. The numerical code of MFIX is fully described in Syamlal (1998).

3.3.2 Simulations

The current highly resolved simulations were done for a typical fluid catalytic cracking particulate whose properties are described in Table (1) together with the gas properties. Those are usual properties already practiced in many previous works.

Table 1: Physical properties of gas and solid.

Symbol	Value	Units	Description
d_p	7.5×10^{-5}	m	Particle diameter
ρ_s	1500	kg/m^3	Particle density
ρ_g	1.3	kg/m^3	Gas density
μ_g	1.8×10^{-5}	$kg/(ms)$	Gas viscosity*
e	0.9	-	Coefficient of restitution

*At Normal Temperature and Pressure (293.15 K, 1 atm)

The free fall terminal velocity, Stokes and Froude numbers of the particulate result (see Section 1.2).

$$v_t = 0.2184 \quad (m/s) \tag{3.71}$$

$$St_{d_p} = 75.83 \tag{3.72}$$

$$Fr_{d_p} = 64.83 \tag{3.73}$$

The simulations were done by imposing the domain average solid volume fraction $\langle \phi_s \rangle$ at specific values for each simulation: 0.05, 0.15 and 0.25. These particle concentrations cover gas-fluidized topologies typical of riser flows.

$\langle \phi_s \rangle$ is enforced through the initial conditions, and is kept constant through the simulations owing to continuity and to the periodical boundaries.

The domain average gas Reynold number is also set constant in each simulation at controlled values. The domain average gas Reynolds number $\langle Re_g \rangle$ based on particle diameter is defined as:

$$\langle Re_g \rangle = \frac{\rho_g \langle \phi_s \rangle \langle \mathbf{v}_{g,y} \rangle d_p}{\mu_g} \tag{3.74}$$

Under the suspension like condition, a gas pressure gradient in the axial (vertical) direction was imposed to be the same as the total weight of the gas and solid components. This gives:

$$\frac{\Delta P_g}{Y_{length}} = \langle \phi_g \rangle \rho_g \mathbf{g} + \langle \phi_s \rangle \rho_s \mathbf{g} \tag{3.75}$$

ΔP_g is imposed over the whole domain in the axial direction, through the initial conditions, and is kept constant throughout the simulations.

The suspension like conditions give rise to the statistical steady state domain average gas axial velocities that define $\langle Re_g \rangle_{susp}$. Multiples of $\langle Re_g \rangle_{susp}$ define various levels of higher gas flow Reynolds number that were practiced. Just as for $\langle \phi_s \rangle$ and ΔP_g, $\langle Re_g \rangle$ are also imposed through initial conditions and are kept constant throughout the simulations.

Figure 8: Run configuration

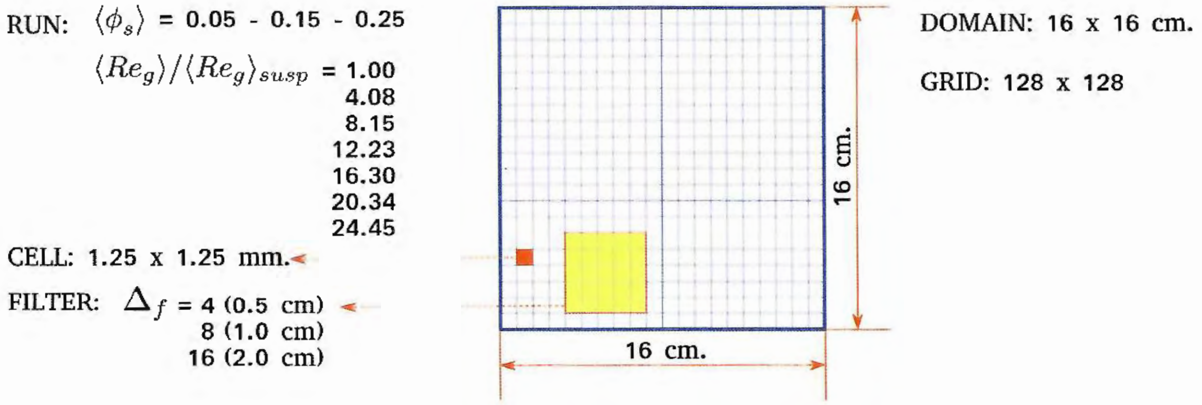
RUN: $\langle \phi_s \rangle$ = 0.05 - 0.15 - 0.25
$\langle Re_g \rangle / \langle Re_g \rangle_{susp}$ = 1.00
4.08
8.15
12.23
16.30
20.34
24.45
CELL: 1.25 x 1.25 mm.
FILTER: Δ_f = 4 (0.5 cm)
8 (1.0 cm)
16 (2.0 cm)
16 cm.
16 cm.
DOMAIN: 16 x 16 cm.
GRID: 128 x 128

Source: Elaborated by the author.

Once $\langle Re_g \rangle_{susp}$ is known, the ratio $\langle Re_g \rangle / \langle Re_g \rangle_{susp}$ is set to a range from 1 to about 24 times that required to sustain a gas-solid like suspension. Actually, uniformly distributed values were set in the simulations: 1.0, 4.08, 8.15, 12.23, 16.30, 20.34 and 24.45.

Table (2) show the complete simulations schedule that was followed. About the dimensions of the domain, a two-dimensional domain of 16 × 16 *cm* was applied, with a numerical mesh of 128 × 128 grids, producing a grid size of 1.25 *mm* (previous results show that grid sizes between 1 and 2 *mm* do provide grid size independent filtered results, Agrawal et al., 2001. Filter sizes (Δ_f) of 0.5 *cm* (4 *cells*), 1.0 *cm* (8 *cells*) and 2.0 *cm*

(16 *cells*) were considered (previous works show that filter sizes up to 1/4 (32 *cells*) of the domain size do provide filtered data independent of domain size, Igci et al., 2008. Figure (8) shows the set up for all simulations.

Table 2: Set up for simulations.

Simulation	$\langle\phi_s\rangle$	$\langle Re_g\rangle/\langle Re_g\rangle_{susp}$
1	0.05	1.00
2		4.08
3		8.15
4		12.23
5		16.30
6		20.34
7		24.45
8	0.15	1.00
9		4.08
10		8.15
11		12.23
12		16.30
13		20.34
14		24.45
15	0.25	1.00
16		4.08
17		8.15
18		12.23
19		16.30
20		20.34
21		24.45

Source: Elaborated by the author.

3.3.3 Filtering and Binning

Once the highly resolved simulations are accomplished, the next step is *filtering*. The results are available for each dependent variable of the TFM. Among those variables are gas volume fraction (ϕ_g), solid volume fraction (ϕ_s), velocity vectors for gas ($\mathbf{v}_g$) and solid ($\mathbf{v}_s$), pressure for gas phase (P_g) and solid phase (P_s). Fields of those variables in space and time are available for filtering. The procedure consists in calculating volume and Favre averages over partial volumes inside the domain (filters), and then using such averages to determine different filtered parameters of concern, such as those defined in Equations (3.55), (3.56), (3.60), (3.63) and (3.70).

The filter comprises a number of domain grid cells and, in the present work, is a square filter-window that is made to sweep throughout the domain while collecting averages. Figure (9) illustrates a given window over the domain. The filtering operation is repeated for as many snapshots as required inside the statistical steady state regime, and under as many different filter sizes as desired. While filtering, averaged values are classified according to ranges of relevant filtered parameters (markers), and statistically averaged for each particular filter size. This is the binning operation.

Figure 9: Filter-window

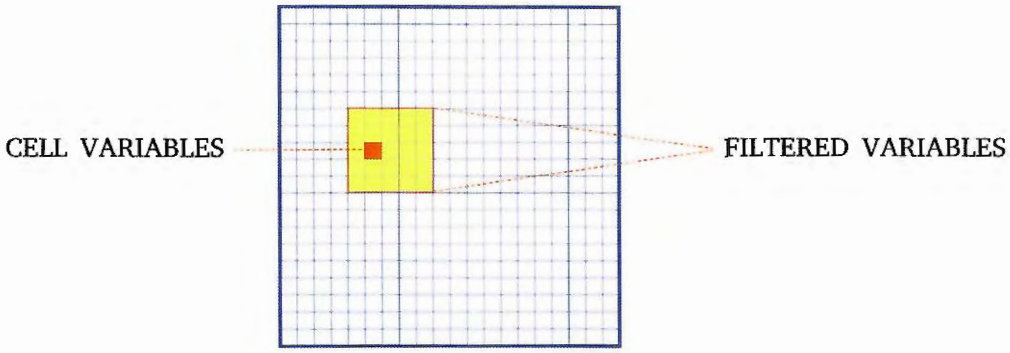

Source: Elaborated by the author.

In the present work two markers are considered. The first marker is the filtered solid volume fraction $\overline{\phi}_s$, and the second marker is the filtered slip velocity $\tilde{\mathbf{v}}_{slip}$ (following Milioli et al., 2013).

The particle volume fraction ϕ_s is defined between $[0-1]$ but experiments show a practical top value $\phi_{s,max} = 0.65$. This is the maximum value allowable for practical purposes (Igci and Sundaresan, 2011).

In this work, that permissible range $[0 \leq \overline{\phi_s} \leq \phi_{s,max}]$ is divided into 64 bins, so that each bin corresponds to a gap of $\Delta\overline{\phi}_s \equiv 0.01$. For the second marker, the filtered slip velocity $\tilde{\mathbf{v}}_{slip}$, the range (which actually results from the simulations) is divided into 80 bins. Consequently, the storage of filtered data was carried out over 64 x 80 bins (this binning resolution was found adequate in previous works, Sarkar et al., 2016). The detailed procedure for filtering and binning can be found in van der Hoef et al. (2006) and Igci et al. (2008).

In summary, one must consider a suitable number of snapshots of the flow field in the statistical steady state regime, so that good averaging statistics are obtained. A snapshot shows the flow field over the whole domain for a particular fixed time. Then a window (or filter) must be defined over the domain comprising a number of numerical cells. Averaging over this region provides averaged or filtered data. The window is made to move in space all over the domain and in time through the various snapshots, and the collected averaged data are classified by ranges of suitable independent variables (markers) and stored into bins. Different window sizes will provide filtered results for different filter sizes.

4 RESULTS AND DISCUSSION

The following section shows the results that were obtained. In all results the filtered solid volume fraction is the first marker and the dimensionless filtered slip velocity is the second marker.

The dimensionless form of the filtered slip velocity is calculated by dividing it by the terminal velocity (v_t); likewise the dimensionless filter size is obtained using the length scale v_t^2/g. Table (3) shows the filters that were considered.

The effects of filter size over filtered parameters are well described by Igci et al. (2008), Igci and Sundaresan (2011), Milioli et al. (2013), Agrawal et al. (2013), Sarkar et al. (2016). Owing to that no analysis is performed regarding the effects of filter size.

Results in this chapter are for dimensionless filter size $\Delta_f/(v_t^2/\mathrm{g}) = 2.056$ (i.e. filter 1 *cm.* x 1 *cm.* or 8 cells x 8 cells). In the appendixes A, B and C results are also presented for filters with 4 and 16 cells. Results presented in the appendixes are quite similar to those presented in the next sections.

Table 3: Values for filtering.

Filter Δ_f (cell)	Filter size Δ_f (cm.)	Dimensionless filter size $\Delta_f/(v_t^2/\mathrm{g})$ (-)
4	0.5	1.028
8	1.0	2.056
16	2.0	4.112

Source: Elaborated by the author.

Figure (10) shows results of the time evolution of the domain average dimensionless gas velocity in the axial direction for suspension like conditions for various $\langle\phi_s\rangle$. The graphs show profiles oscillating around well established averages in the statistical steady state regime, which are used to determine the respective domain average gas Reynolds numbers showed in Table (4).

Table 4: Reynolds number for suspension condition runs.

	$\langle\phi_s\rangle$		
	0.05	0.15	0.25
$\langle Re_g\rangle_{susp}$	4.67	2.26	0.96

Source: Elaborated by the author.

Figure 10: Dimensionless gas velocity in the axial direction, $\langle \mathbf{v}_g \rangle^*_{susp}$, as a function of dimensionless time, t^*, for the runs under suspension like conditions, for domain average solid volume fractions $\langle \phi_s \rangle = 0.05$ (a), 0.15 (b) and 0.25 (c).

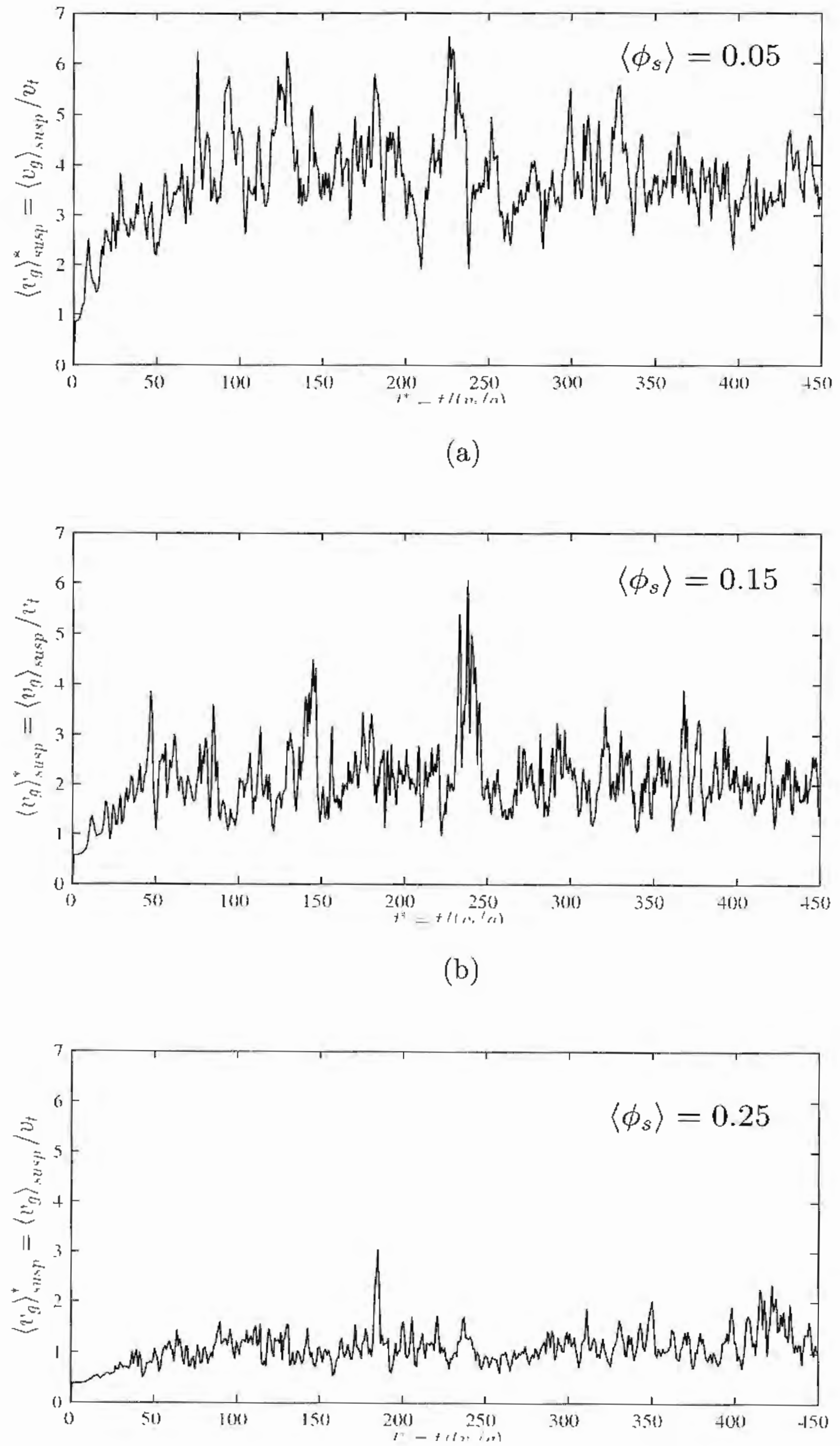

(a)

(b)

(c)

The Reynolds numbers for the other runs were established taking $\langle Re_g \rangle_{susp}$ as a reference. Table (5) depicts all the values of Reynolds numbers $\langle Re_g \rangle$ and the domain average solid volume fractions for the various runs. The ratio $\langle Re_g \rangle / \langle Re_g \rangle_{susp}$ was kept constant for the different $\langle \phi_s \rangle$ that were practiced.

Table (5) shows that as the concentration of solids in the flow increases the Reynolds number decreases, as the presence of more particles exerts a higher drag holding effect over the gas.

Table 5: Reynolds numbers for all runs.

		$\langle \phi_s \rangle$	
$\langle Re_g \rangle / \langle Re_g \rangle_{susp}$	0.05	0.15	0.25
1.00	4.67	2.26	0.96
4.08	18.21	9.21	3.92
8.15	36.33	18.42	7.83
12.23	54.54	27.63	11.75
16.30	72.67	36.83	15.67
20.34	90.71	46.04	19.54
24.45	109.00	55.25	23.50

Source: Elaborated by the author.

For all the simulations the statistical steady state regime was already established at about $t^* = 45$ (Figure (10) shows that for the suspension like simulations). In all the cases, the filtering was performed in a time interval from $t^* = 45$ to 450, which provided suitable statistics.

4.1 Flow topology

Figure 11 shows how the flow topology is affected by $\langle Re_g \rangle$ and $\langle \phi_s \rangle$. The figure shows snapshots of the flow for $\langle \phi_s \rangle$ of 0.05, 0.15 and 0.25, and for $\langle Re_g \rangle / \langle Re_g \rangle_{susp} = 1.00$, 8.15, 16.30 and 24.45. Comparing all the figures it can be noticed that both parameters have significant effect over the spatial distribution of particles throughout the domain as well as over the sizes and shapes of the solid structures.

It is seen that an increase on $\langle Re_g \rangle / \langle Re_g \rangle_{susp}$ for a given $\langle \phi_s \rangle$ causes the regions with higher solid concentrations (clusters) to stretch in the axial direction, and the flow field to grow increasingly homogeneous. Otherwise, an increase on $\langle \phi_s \rangle$ for a given $\langle Re_g \rangle / \langle Re_g \rangle_{susp}$ gives rise to denser and thicker structures.

The changes on topology observed in Figure 11, as $\langle \phi_s \rangle$ and $\langle Re_g \rangle / \langle Re_g \rangle_{susp}$ are varied, point towards related effects over relevant filtered parameters such as the drag coefficient correction and stresses related filtered and effective parameters. This matter is addressed next. It must be noticed that more detailed analysis related to effects of inside filtered parameters (i.e. 1^{st} and 2^{nd} markers) will not be pursued here since, just like effects related to filter size, such trends are already well addressed in literature (Igci et al., 2008; Igci and Sundaresan et al., 2011; Milioli et al., 2013; Sarkar et al., 2016).

Figure 11: Grayscale plots of solid volume fraction in the domain inside the statistical steady state regime, for simulations with domain average solid fractions $\langle \phi_s \rangle = 0.05$, 0.15 and 0.25 (columns), and gas Reynolds number ratios $\langle Re_g \rangle / \langle Re_g \rangle_{susp} = 1$, 8.15, 16.30, 24.45 (rows)

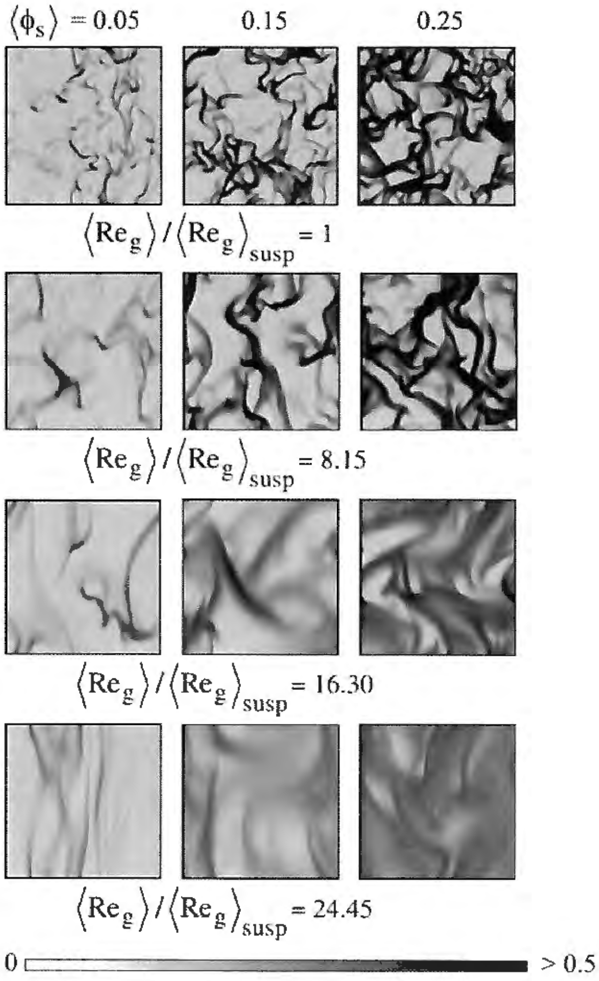

4.2 Drag coefficient correction

The drag coefficient correction H is a correction applied over the filtered Wen and Yu's drag coefficient (which stands for homogeneous flows), so that an effective drag coefficient is derived accounting for both meso-scale filtered drag and buoyancy fluctuation effects (see Equation (3.70)). H closing to zero means a topology closing towards a flow with uniformly distributed particles (i.e. closing towards homogeneity). Otherwise, as a flow becomes more and more heterogeneous, with clusters developing and growing larger and heavier and gas by-pass becoming more dominant, effective drag progressively looses relevance, and H closes to unity.

Figure (12) shows the variation of H with filtered solid volume fraction, dimensionless filtered slip velocity and Reynolds number ratio, for a dimensionless filter size $\Delta_f/\left(\mathrm{v}_t^2/\mathrm{g}\right) = 2.056$. Figures (12$a$), (12$b$) and (12$c$) stand for different domain average solid volume fractions.

It is clear from Figures (12a), (12b) and (12c) that H changes significantly with filtered solid volume fraction and filtered slip velocity. The higher the filtered solid volume fraction and the higher the filtered slip velocity, the higher H becomes. This implies that higher solid fractions and higher slip velocities are related to growing non-homogeneities on the flow.

The gas Reynolds number ratio considerably affects H for all domain average solid volume fractions. This influence is noticeable at lower filtered slip velocities while for higher values of filtered slip velocities the effect tends to decline progressively. It can be claimed that Reynolds number has no effect on H at high filtered slip velocities for the domain average solid volume fractions of 0.05, 0.15 and 0.25 that were considered.

However, at relative small filtered slip velocities, the higher the Reynolds number ratio the smaller H becomes. This effect is intensified with decreasing filtered slip velocity and lower filtered solid volume fraction. This is a consequence of the flow becoming more homogeneous at high gas Reynolds numbers and lower solid volume fractions, which is supported by the solid volume fraction grayscale plots in Figure (11).

Figure (13) shows the variation of the drag coefficient correction H with the filtered solid volume fraction and dimensionless filtered slip velocity, for domain average solid volume fractions $\langle\phi_s\rangle = 0.05$, 0.15 and 0.25, and Reynolds number ratios $\langle Re_g\rangle/\langle Re_g\rangle_{susp}$ from 1 to 20.34. The graphs stand for a dimensionless filter size $\Delta_f/\left(\mathrm{v}_t^2/\mathrm{g}\right) = 2.056$.

It is seen that changing $\langle\phi_s\rangle$ from 0.15 to 0.25 has no effect on H for gas Reynolds number ratios $\langle Re_g\rangle/\langle Re_g\rangle_{susp}$ up to 8.15 (Figures (13a) and (13b)). Otherwise, for $\langle Re_g\rangle/\langle Re_g\rangle_{susp} > 8.15$ the profiles depart from each other at low filtered solid volume fractions, and this difference becomes negligible for high filtered solid volume fractions. (Figures (13c) to (13f))

It can be seen that the filtered solid volume fraction from which the profiles collapse together is lower for larger filtered slip velocities. Also, the profiles grow more apart from each other at higher gas Reynolds number ratios. As the profiles for $\langle\phi_s\rangle = 0.05$, not only they depart from the others at any $\langle Re_g\rangle/\langle Re_g\rangle_{susp}$, but they also present a different shape. This change of behavior may be related to topology changes, which need to be further investigated.

Figure 12: Drag coefficient correction, H, as a function of the filtered solid volume fraction, $\overline{\phi}_s$, for various gas Reynolds ratios $\langle Re_g \rangle / \langle Re_g \rangle_{susp} = 1$ (–), 4.08 (○), 8.15 (◁), 12.23 (◇), 16.30 (▷), 20.34 (□), and 24.45 (▽), for the domain average solid volume fraction $\langle \phi_s \rangle = 0.05$ (a), 0.15 (b) and 0.25 (c). The results stand for the dimensionless filtered axial slip velocities $\tilde{\mathbf{v}}_{slip,y}/\mathbf{v}_t = 0.85$, 2.03 and 4.85, and the dimensionless filter size $\Delta_f / (\mathbf{v}_t^2/\mathbf{g}) = 2.056$

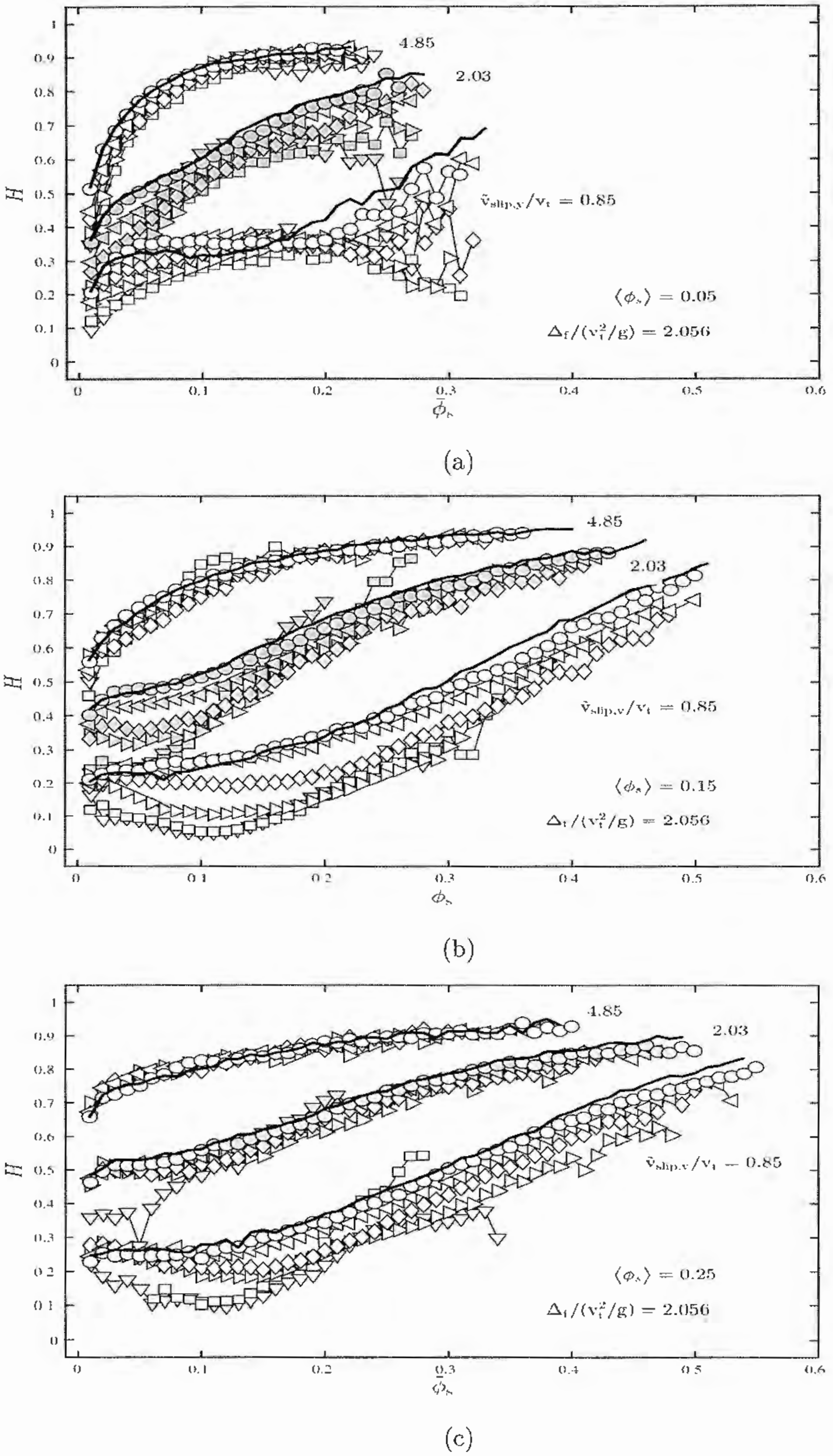

(a)

(b)

(c)

Figure 13: Drag coefficient correction, H, as a function of the filtered solid volume fraction, $\overline{\phi}_s$, for the domain average solid volume fractions $\langle \phi_s \rangle = 0.05$ (full lines), 0.15 (gray symbols) and 0.25 (white symbols), for gas Reynolds ratios $\langle Re_g \rangle / \langle Re_g \rangle_{susp} = 1$ (a), 4.08 (b), 8.15 (c), 12.23 (d), 16.30 (e), 20.34 (f). The results stand for the dimensionless filtered axial slip velocities $\tilde{\mathbf{v}}_{slip,y}/\mathbf{v}_t = 0.85$, 2.03 and 4.85, and the dimensionless filter size $\Delta_f / (\mathbf{v}_t^2/\mathbf{g}) = 2.056$

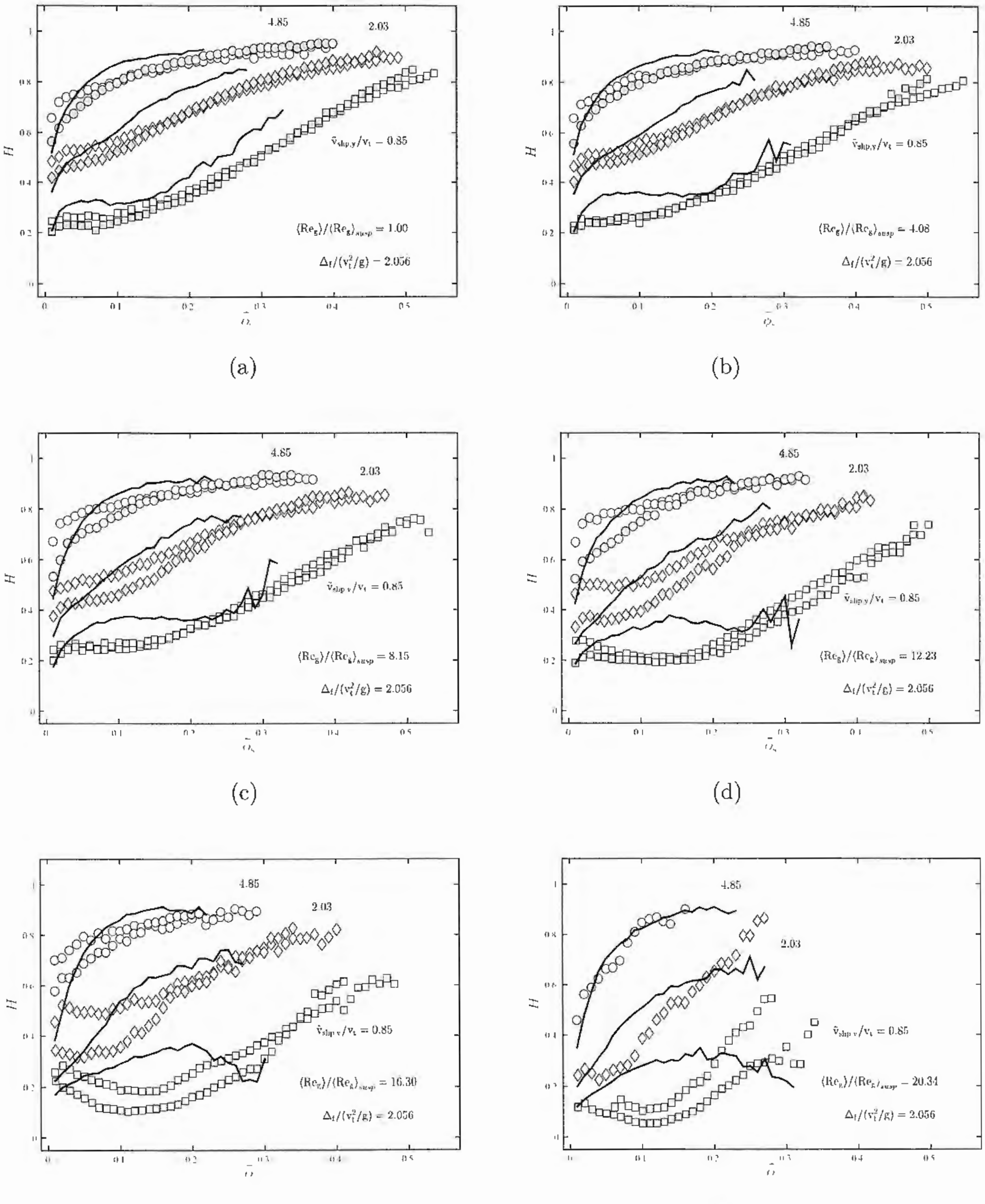

(a) (b)

(c) (d)

(e) (f)

4.3 Filtered pressure and dynamic viscosity for solid phase

Figures (14) and (15) show the variation of the dimensionless filtered solid pressure $P_{fil,s}$, with filtered solid volume fraction and gas Reynolds number ratios, for the dimensionless filter size $\Delta_f/\left(\mathbf{v}_t^2/\mathbf{g}\right) = 2.056$. The figures stand for the dimensionless filtered slip velocity $\tilde{\mathbf{v}}_{slip,y}/\mathbf{v}_t = 0.85$ and 4.85, respectively. Also, each figure stands for domain average solid fractions $\langle\phi_s\rangle = 0.05$, 0.15 and 0.25 (graphs a, b, c).

The filtered solid pressure $P_{fil,s}$ shows a general decreasing tendency as $\langle Re_g\rangle/\langle Re_g\rangle_{susp}$ increases. This comes as a consequence of the filtered granular temperature considerably dropping due to a higher dissipation of granular energy as $\langle Re_g\rangle$ grows high. For the lower $\tilde{\mathbf{v}}_{slip,y}/\mathbf{v}_t = 0.85$, $P_{fil,s}$ decreases by up to one order of magnitude as $\langle Re_g\rangle/\langle Re_g\rangle_{susp}$ increases from 1 to 24.45, for all $\langle\phi_s\rangle$ (0.05, 0.15 and 0.25). For the higher $\tilde{\mathbf{v}}_{slip,y}/\mathbf{v}_t = 4.85$, a decrease of $P_{fil,s}$ with $\langle Re_g\rangle/\langle Re_g\rangle_{susp}$ is still observed, but relatively smaller. See figure (15).

Figure (16) shows graphs similar to those of Figure (14), but for the dimensionless filtered dynamic viscosity of the solid phase $\mu_{fil,s}$ given by equation (3.56).

The dropping of granular temperature also causes $\mu_{fil,s}$ to decrease with increasing $\langle Re_g\rangle$, similarly to what happened for $P_{fil,s}$. Again, variations of up to one order of magnitude are observed as $\langle Re_g\rangle/\langle Re_g\rangle_{susp}$ changes from 1 to 24.45.

Figure 14: Filtered solid pressure, $P_{fil,s}$, as a function of the filtered solid volume fraction, $\overline{\phi}_s$, for various gas Reynolds ratios $\langle Re_g\rangle/\langle Re_g\rangle_{susp} = 1$ (−), 4.08 (○), 8.15 (◁), 12.23 (◇), 16.30 (▷), 20.34 (□), and 24.45 (▽), for the domain average solid volume fraction $\langle\phi_s\rangle = 0.05$ (a), 0.15 (b) and 0.25 (c). The results stand for the dimensionless filtered axial slip velocity $\tilde{\mathbf{v}}_{slip,y}/\mathbf{v}_t = 0.85$ and the dimensionless filter size $\Delta_f/\left(\mathbf{v}_t^2/\mathbf{g}\right) = 2.056$

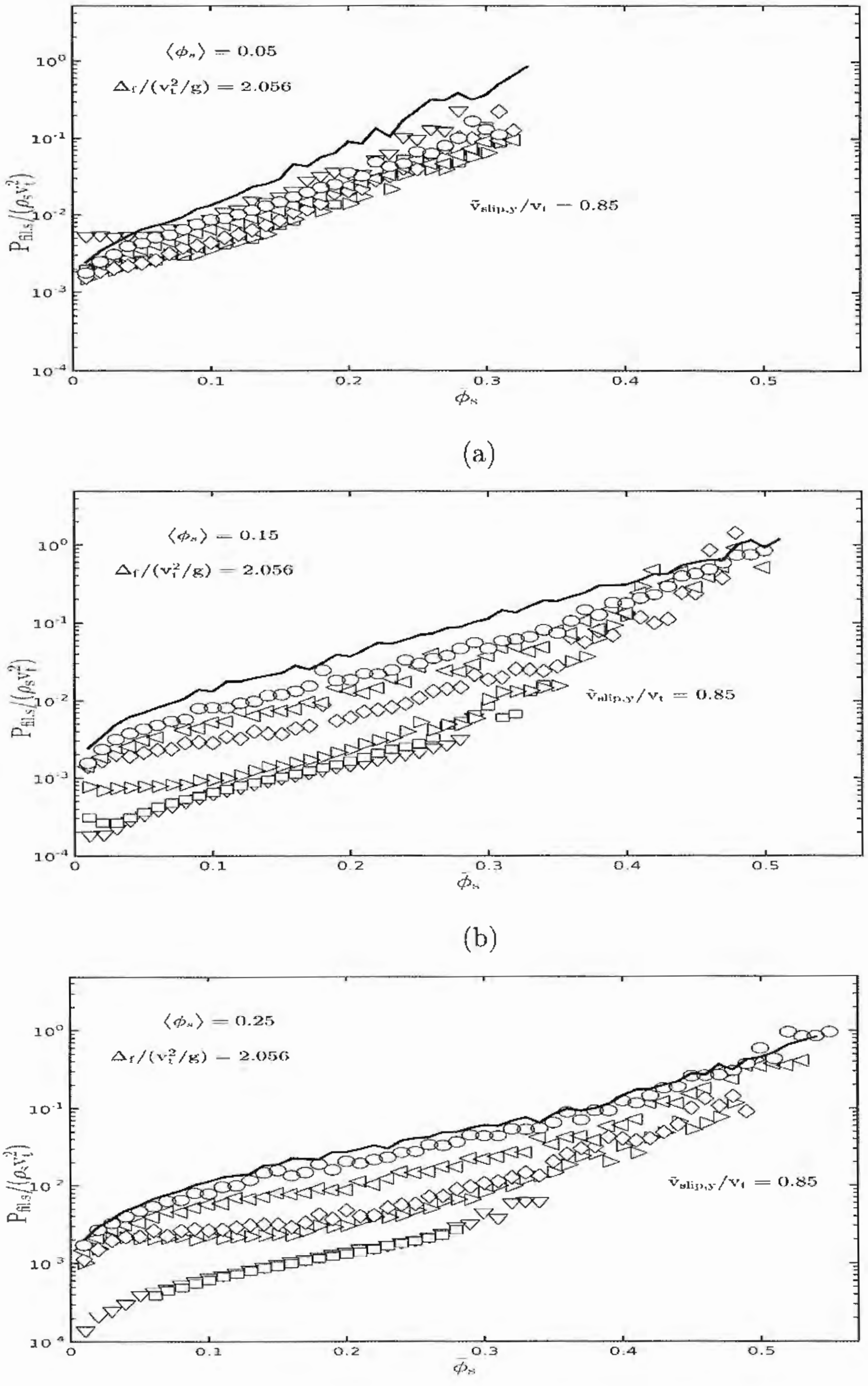

(a)

(b)

(c)

Figure 15: Filtered solid pressure, $P_{fil,s}$, as a function of the filtered solid volume fraction, $\bar{\phi}_s$, for various gas Reynolds ratios $\langle Re_g\rangle/\langle Re_g\rangle_{susp}$ = 1 (–), 4.08 (○), 8.15 (◁), 12.23 (◇), 16.30 (▷), 20.34 (□), and 24.45 (▽), for the domain average solid volume fraction $\langle\phi_s\rangle = 0.05$ (a), 0.15 (b) and 0.25 (c). The results stand for the dimensionless filtered axial slip velocity $\tilde{\mathbf{v}}_{slip,y}/\mathbf{v}_t = 4.85$ and the dimensionless filter size $\Delta_f/(\mathbf{v}_t^2/\mathbf{g}) = 2.056$

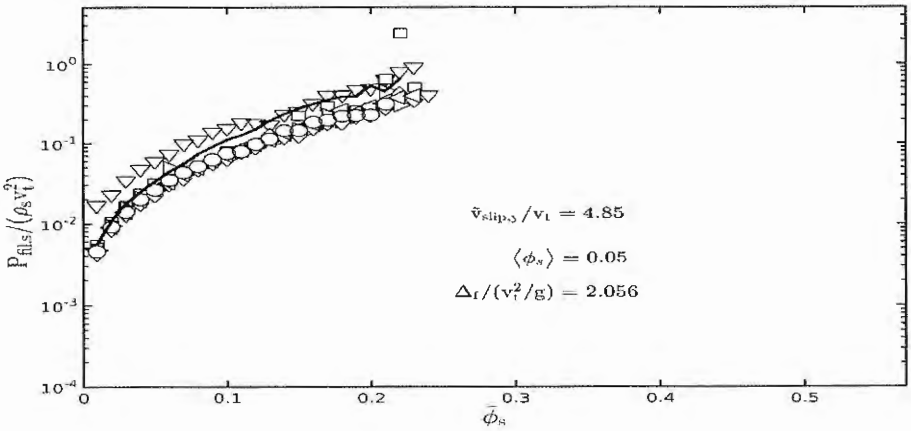

(a)

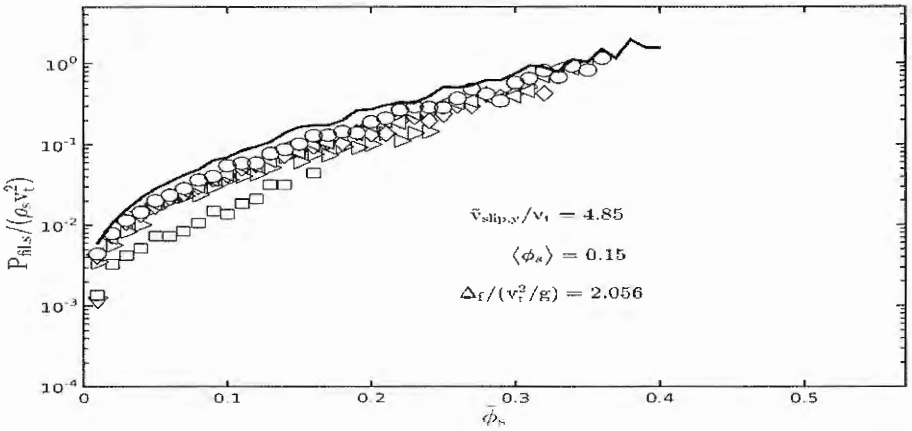

(b)

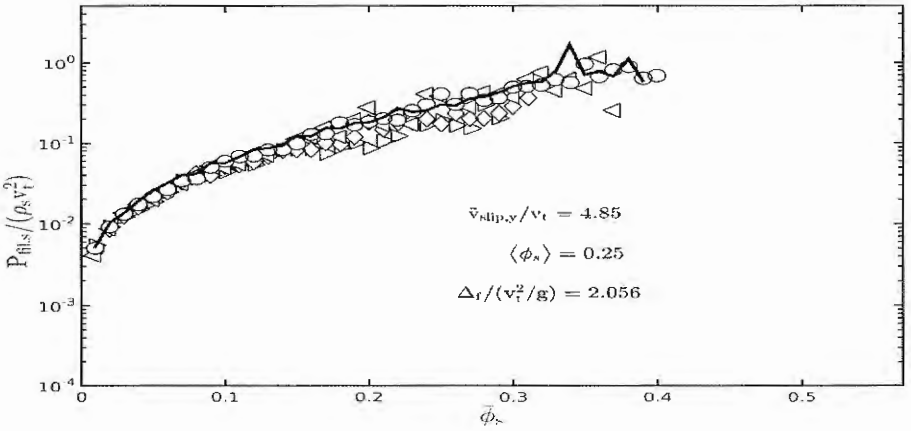

(c)

Figure 16: Filtered solid dynamic viscosity, $\mu_{fil,s}$, as a function of the filtered solid volume fraction, $\overline{\phi}_s$, for various gas Reynolds ratios $\langle Re_g\rangle/\langle Re_g\rangle_{susp} = 1$ (−), 4.08 (○), 8.15 (◁), 12.23 (◇), 16.30 (▷), 20.34 (□), and 24.45 (▽), for the domain average solid volume fraction $\langle\phi_s\rangle = 0.05$ (a), 0.15 (b) and 0.25 (c). The results stand for the dimensionless filtered axial slip velocity $\tilde{\mathbf{v}}_{slip,y}/\mathbf{v}_t = 0.85$ and the dimensionless filter size $\Delta_f/\left(\mathbf{v}_t^2/\mathbf{g}\right) = 2.056$

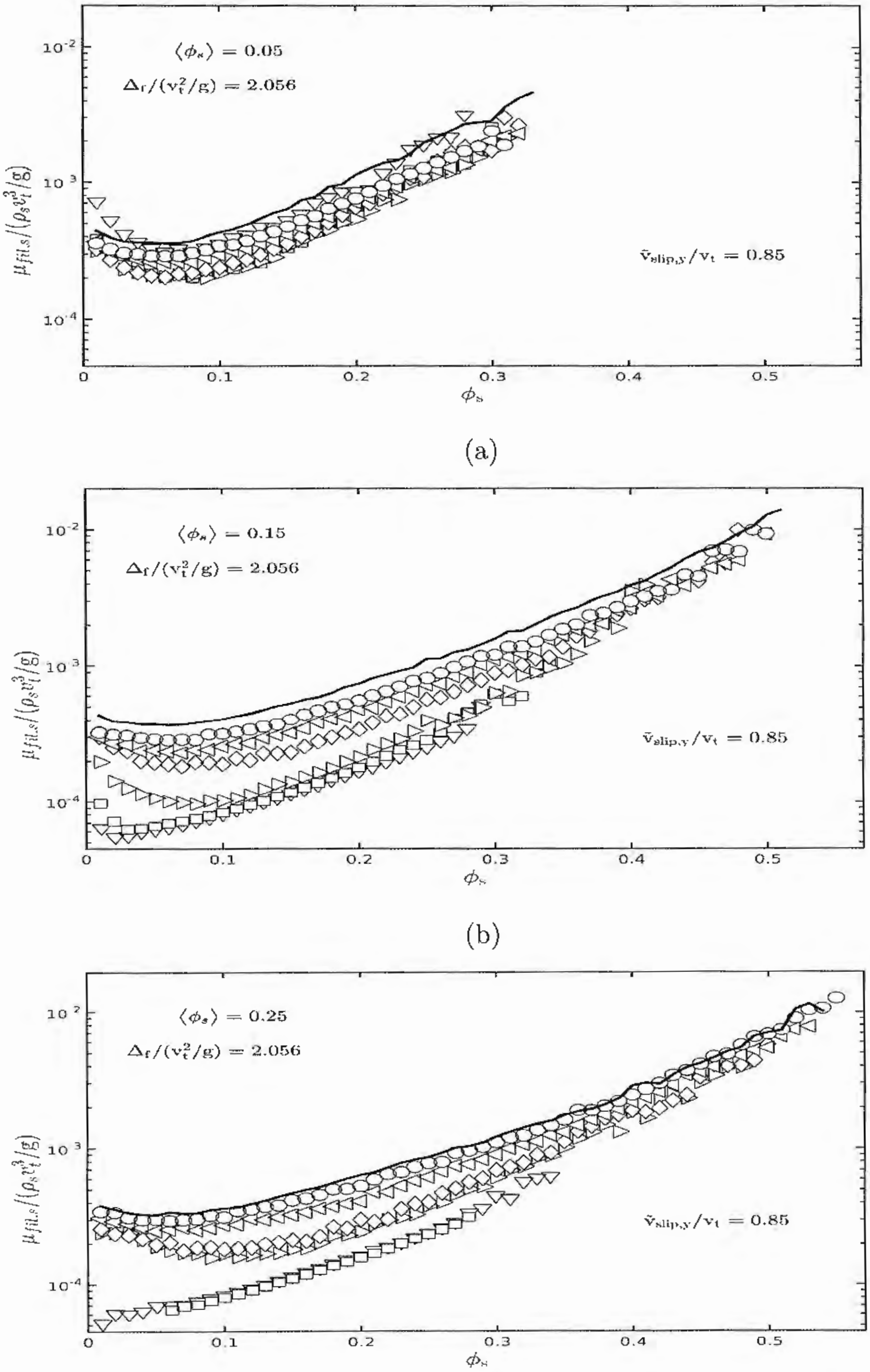

(a)

(b)

(c)

4.4 Effective pressures and dynamic viscosities for solid and gas phases

Figure (17) shows the variation of the dimensionless effective pressure of the solid and gas phases, $P_{eff,s}$ and $P_{eff,g}$, with filtered solid volume fraction and gas Reynolds number ratios, for the dimensionless filter size $\Delta_f / \left(\mathrm{v}_t^2/\mathrm{g}\right) = 2.056$. The figure stands for the dimensionless filtered slip velocity $\tilde{\mathrm{v}}_{slip,y}/\mathrm{v}_t = 0.85$ and for the domain average solid fractions $\langle \phi_s \rangle = 0.05$, 0.15 and 0.25 (graphs a, b, c).

The curves for $P_{eff,s}$ are similar to those for $P_{fil,s}$. As expected there was difference in order of magnitude between the gas and the solid effective pressures (Agrawal et al., 2001). Both $P_{eff,s}$ and $P_{eff,g}$ decrease for increasing $\langle Re_g \rangle / \langle Re_g \rangle_{susp}$. The effect of $\langle Re_g \rangle$ is higher at low $\overline{\phi}_s$, and tends to disappear for high $\overline{\phi}_s$.

Figure (18) shows graphs similar to those of Figure (17), but for the dimensionless effective viscosities of both phases $\mu_{eff,s}$ and $\mu_{eff,g}$.

Just like $P_{eff,s}$ and $P_{eff,g}$, $\mu_{eff,s}$ and $\mu_{eff,g}$ also decrease as $\langle Re_g \rangle / \langle Re_g \rangle_{susp}$ increases. Also similarly, the effect of $\langle Re_g \rangle$ is higher at lower $\overline{\phi}_s$, and tends to disappear for high $\overline{\phi}_s$.

Just as found for $P_{fil,s}$ and $\mu_{fil,s}$, also for $P_{eff,s}$, $P_{eff,g}$, $\mu_{eff,s}$ and $\mu_{eff,g}$, there are variations of up to one order of magnitude as $\langle Re_g \rangle / \langle Re_g \rangle_{susp}$ changes from 1 to 24.45.

The fact that all the effective pressures and viscosities drop as $\langle Re_g \rangle$ increases is a result of the flow becoming more homogeneous (see Figure (11)), with consequent reduction of space fluctuations on both phases. It is noticeable that this behavior is opposed to that of mono-phase turbulent flows, where higher Reynolds numbers impose higher fluctuations, and then higher effective pressures and viscosities.

Figure 17: Effective solid and gas pressures, $P_{eff,s}$ and $P_{eff,g}$, as a function of the filtered solid volume fraction, $\overline{\phi}_s$, for various gas Reynolds ratios $\langle Re_g \rangle / \langle Re_g \rangle_{susp} = 1$ (–), 4.08 (○), 8.15 (◁), 12.23 (◇), 16.30 (▷), 20.34 (□), and 24.45 (▽), for the domain average solid volume fraction $\langle \phi_s \rangle = 0.05$ (a), 0.15 (b) and 0.25 (c). The results stand for the dimensionless filtered axial slip velocity $\tilde{\mathbf{v}}_{slip,y}/\mathbf{v}_t = 0.85$ and the dimensionless filter size $\Delta_f/\left(\mathbf{v}_t^2/\mathbf{g}\right) = 2.056$

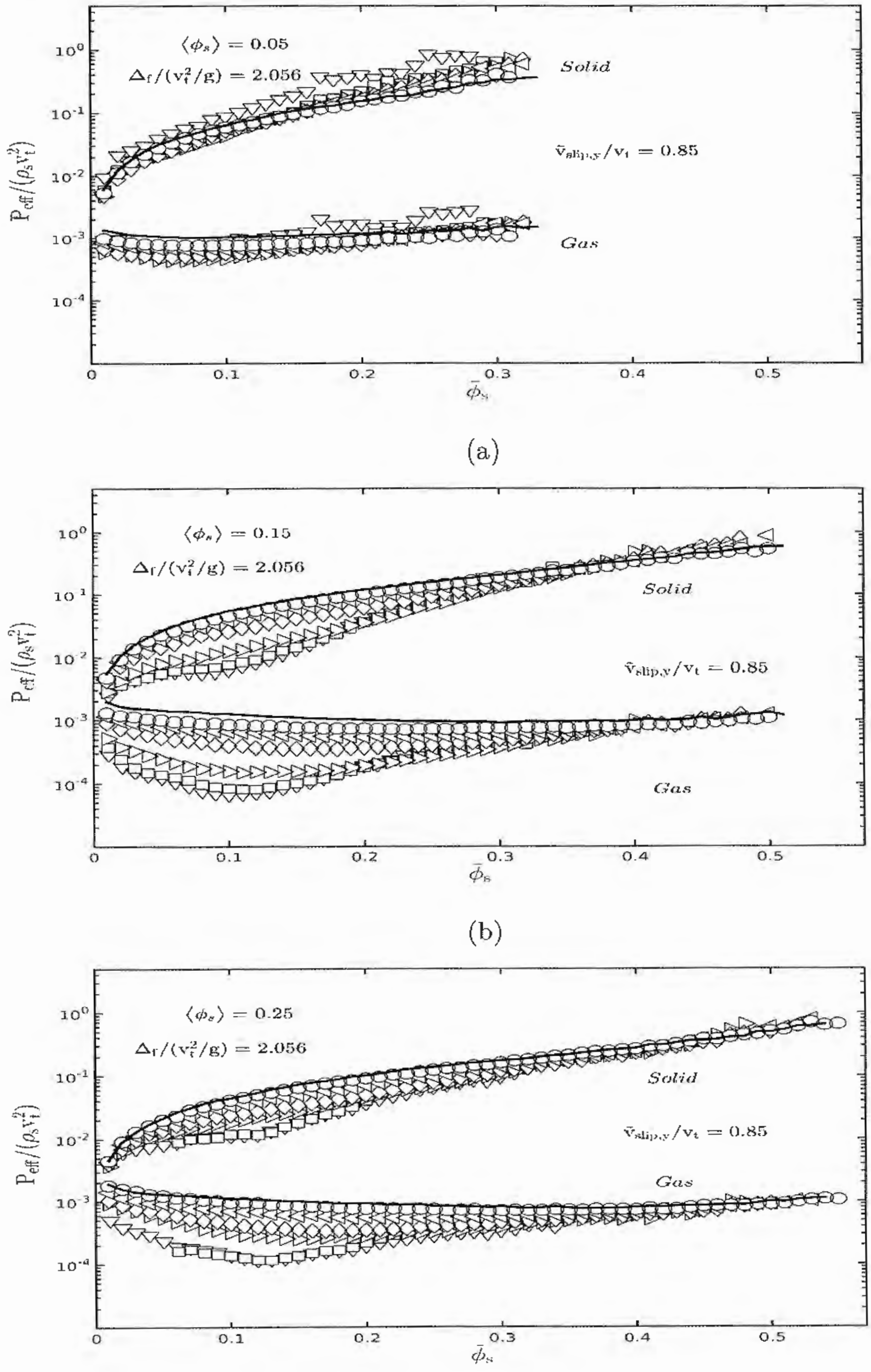

(a)

(b)

(c)

Figure 18: Effective solid and gas dynamic viscosities, $\mu_{eff,s}$ and $\mu_{eff,g}$, as a function of the filtered solid volume fraction, $\overline{\phi}_s$, for various gas Reynolds ratios $\langle Re_g\rangle/\langle Re_g\rangle_{susp} = 1$ (−), 4.08 (○), 8.15 (◁), 12.23 (◇), 16.30 (▷), 20.34 (□), and 24.45 (▽), for the domain average solid volume fraction $\langle\phi_s\rangle = 0.05$ (a), 0.15 (b) and 0.25 (c). The results stand for the dimensionless filtered axial slip velocity $\tilde{\mathbf{v}}_{slip,y}/\mathbf{v}_t = 0.85$ and the dimensionless filter size $\Delta_f/(\mathbf{v}_t^2/\mathbf{g}) = 2.056$

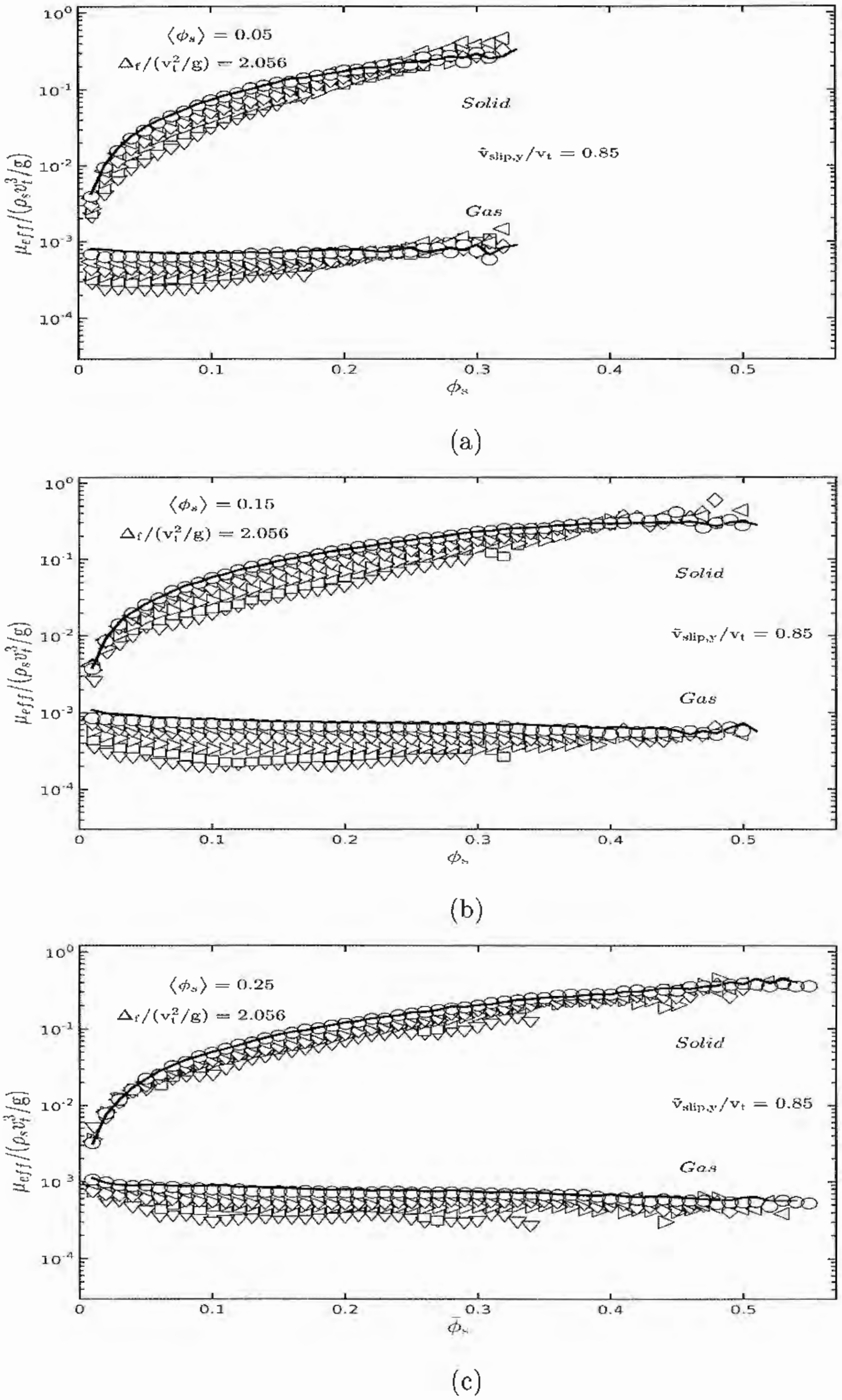

(a)

(b)

(c)

5 CONCLUSIONS AND SUGGESTIONS FOR FUTURE WORK

5.1 Conclusions

Large scale simulations of gas-solid riser flows require sub-grid closure models to recover effects filtered by the usual coarse grids that are applied. A widely practiced method used to derive such sub-grid models consists of filtering over results of meso-scale highly resolved simulations with microscopic two-fluid modeling. In the usual procedure, relevant filtered parameters such as effective drag coefficients and stresses related parameters are correlated to suitable filtered variables such as the filtered solid volume fraction and the filtered slip velocity. It comes out that the provided correlations do not take any account of macro-scale conditions, namely the flow topology, which is consistent with the usual scale separation assumption, even though such a separation of scales does not hold in fluidized gas-solid flows. This work was intended to verify whether a macro-scale dependence is required to be accounted for in sub-grid correlation, and to what extent. In order to do so, two macro-scale parameters usually associated to flow topology were considered as for their effects over relevant filtered parameters. Those are the macro-scale average solid volume fraction and the macro-scale average gas flow Reynolds number. The developments were carried out for dilute flow conditions typical of riser flows.

The current highly resolved simulations were performed using the well established microscopic two-fluid model of the MFIX code, where microscopic closures for fluid properties and stresses of the solid phase are brought from the kinetic theory of granular flows (Lun et al., 1984), and the microscopic closure for drag is provided by Wen & Yu's drag model (Wen & Yu, 1966). All the simulations were carried out for a unique particulate typical of fluid catalytic cracking widely studied in previous works. As a unique Froude number was considered, scaling was not treated at any extent. The simulations were performed over 2D periodical domains keeping the domain average gas flow rate and solid volume fraction as constants. Results were collected over statistical steady state conditions and through a time interval large enough to provide for robust statistics. Average filtered results were then gathered for particular filter sizes sweeping over the domain in space and time, and stored as a function of relevant filtered variables (i.e. filtered solid volume fraction and filtered slip velocity), for each pair of macro-scale conditions imposed in the simulations (i.e. domain average solid volume fraction and domain average gas Reynolds number).

Results showed considerable topology impacts as the concerning macro-scale parameters were varied, with very significant effects over the filtered parameters of interest, namely the drag coefficient correction, and the filtered and effective pressures and viscosities of both phases. The main conclusions that were drawn from the results are as follows:

1. Grayscale plots of solid volume fraction over the whole domain, for snapshots inside the statistical steady state regime, show a considerable effect over the flow topology of both macro-scale parameters, i.e. the domain average solid volume fraction and the domain average gas Reynolds number. An increase on gas Reynolds number ratio for a given domain average solid volume fraction causes the regions with higher solid concentrations (clusters) to stretch in the axial direction, and the flow field to grow increasingly homogeneous. Otherwise, an increase on domain average solid volume fraction for a given gas Reynolds number ratio gives rise to denser and thicker structures. Effects similar to those were reported by Milioli and Milioli (2011) for a much coarser particulate ($Fr_p = 1235.4$), even though the current particulate Froude number is about 19 times smaller. This similitude of behavior is suggestive having in view future scaling concerns.

2. The drag coefficient correction, H, stands for a correction over the filtered Wen and Yu's drag coefficient, which is suitable to homogeneous flows, in order to provide for an effective drag coefficient suitable to heterogeneous flows. Therefore, the smaller H is the more homogeneous is the flow. Irrespective of the domain average solid volume fraction, the current results show that a higher domain average gas Reynolds number causes H to decrease, an effect that becomes more prominent at lower filtered solid volume fractions and lower filtered slip velocities. This behavior comes from the flow becoming more homogeneous at higher gas Reynolds numbers and lower solid volume fractions, which is supported by solid volume fraction grayscale plots. In regions of lower slip velocities H is lower and, as the gas Reynolds number increases, the spread among the profiles become larger and grow through a larger range of solid volume fractions. In summary, the drag coefficient correction was significantly affected by the average gas Reynolds number noticeably at lower filtered solid volume fractions and lower filtered slip velocities, no matter the average solid volume fraction. Otherwise, the effect of the average solid volume fraction over the drag coefficient correction was significant only at higher gas Reynolds numbers.

3. The filtered and effective pressure and viscosity of the solid phase are all considerably decreased as the domain average gas Reynolds number increases. For the gas Reynolds numbers that were imposed, ranging from suspension like conditions up to conditions close to pneumatic transport, all of those parameters experimented variations of up to one order of magnitude. Regarding the filtered parameters, this comes as a consequence of the filtered granular temperature considerably dropping due to a higher dissipation of granular energy as the gas Reynolds number grows high. Regarding the effective parameters, this comes as a result of the flow becoming

more homogeneous at higher gas Reynolds numbers, with consequent reduction of space fluctuations on both phases. It is noticeable that the dropping with increasing gas Reynolds numbers of the effective pressures and viscosities in gas-solid flows is opposed to what happens in mono-phase turbulence, where higher Reynolds numbers impose higher fluctuations, and thereby higher effective pressures and viscosities. In summary, there were significant quantitative variations of all the stresses related filtered parameters, which were even more intense at high average gas Reynolds numbers. The effective pressure and viscosity of the gas phase have similar behavior as compared to those for the solid phase.

The present results allow to conclude that the currently usual sub-grid modeling that correlates relevant filtered parameters to inside filter parameters alone is clearly insufficient. Evidence was presented pointing that a more rigorous sub-grid modeling must also embrace topology related effects, the macro-scale average solid volume fraction and the macro-scale average gas Reynolds number standing as relevant parameters to be accounted for.

5.2 Some suggestions for future work

The accuracy of the current sub-grid analysis of gas-solid fluidized flows based on highly resolved simulations with microscopic two-fluid modeling ultimately depends on the accuracy of the microscopic formulation and closures that are applied. Therefore, microscopic two-fluid model enhancements and improved closures are always wanted. Some possible issues for future research may include:

1. Newtonian rheology is usually assumed for both phases, the gas as well as the solid phase that accounts for the particulate treated as a continuum. While the Newtonian assumption sounds correct for the gas phase, there is no evidence that it is equally adequate for the solid phase. This is an issue for further research.

2. The grids on highly resolved simulations are still quite coarse from the point of view of the gas phase, so that under-grid scale gas turbulence is filtered. At one side, direct numerical simulation is still unfeasible in view of the domain sizes that need to be resolved and owing to computational limitations. At another side, gas turbulence still needs to be accounted for in order to unveil its possible effects on flow heterogeneity and thereby on filtered parameters. Knowledge is very limited in those fields. While there is some knowledge on how particulates interact with gas turbulence depending on particle Stokes number, little is known regarding interactions with structures of particles, no matter their Stokes number. This is an issue waiting for new ideas.

3. Most highly resolved simulations analyses on literature concentrate on monodisperse particulates. As real gas-solid flows are usually characterized by wide granulometry distributions, polidisperse analyses are needed.
4. Hydrodynamic scaling is quite a challenge in gas-solid fluidized flows. In order to exploit that matter, much extensive computational experimentation is needed for various Froude number particulates and macro-scale flow conditions. That would be a start for addressing hydrodynamic scaling in the field.
5. The most practiced microscopic closure for drag comes from a well accepted correlation by Wen and Yu (1966), which nevertheless was originally derived for gas-liquid uniformly fluidized flows. This situation does not suit the very heterogeneous gas-solid fluidized flows, and new approaches are needed. A possibility would be to derive new micro-scale correlations from predictions with discrete element methods, for instance.
6. Besides drag, other interface effects among phases may become relevant in gas-solid fluidized flows. Effects such as friction, electrostatic and moisture could be assessed in future highly resolved simulation analyses.
7. The kinetic theory of granular flows, which is used to derive closure properties for solid phases treated as continua, is still to be validated. This is a challenge waiting for new fresh ideas.

BIBLIOGRAPHY

Agrawal, K., Holloway, W., Milioli, C.C., Milioli, F.E. and Sundaresan, S., 2013, "Filtered models for scalar transport in gas-particle flows", Chem. Eng. Science, Vol,. 95, pp. 291-300.

Agrawal, K., Loezos, P.N., Syamlal, M. and Sundaresan, S., 2001, "The role of meso-scale structures in rapid gas-solid flows", J. Fluid Mech., Vol. 445, pp. 151-185.

Anderson, T. B., Jackson, R., 1967, "Fluid mechanical description of fluidized beds. Equations of motion", Ind. Eng. Chem. Fund., Vol. 6, pp. 527-539.

Andrews IV, A.T., Loezos, P.N. and Sundaresan, S., 2005, "Coarse-grid simulation of gas-particle flows in vertical risers", Ind. Eng. Chem. Res., Vol. 44, No. 16, pp. 6022-6037.

Bagnold, R. A., 1954, "Experiments on a gravity-free dispersion of large solid spheres in a Newtonian fluid under shear", Proc. R. Soc., Vol. A225, pp. 49-63.

Basu, P., Fraser, 1991, "Circulating Fluidized Bed Boiler: Design and Operation", Butterworth-Heinemann, Boston.

Bi, H. T., Grace, J.R., 1997, " Flow Regime Diagrams for Gas-Solid Fluidization and Upward Transport ", Int. J. Multiphase Flow, 21, 1229-1236.

Clift, R., Grace, J. R., Weber, M. E., 1978, " Bubbles, Drops and Particles ", Academic Press, Inc. 111 Fifth Avenue, New York, New York 10003.

da Silva, R.C., Cabezas-Gómez, L. and Milioli, F.E., 2006, "Some modeling and numerical aspects of the two-fluid simulation of the gas-solids flow in a CFB riser", Brazilian J. of Chem. Eng., Vol. 23, pp. 487-496.

Delhaye, J. M., 1974, "Jump conditions and entropy sources in two-phase systems. Local instant formulation", Int. J. Multiphase Flow, Vol. 1, pp. 395-409.

Delhaye, J.M., 1981, “Local instantaneous equations”, in: Thermohydraulics of two-phase systems for industrial design and nuclear engineering, eds: J.M. Delhaye, M. Giot & M.L. Riethmuller, Hemisphere & McGraw-Hill, Chap. 5, pp. 95-116.

Drew, D. A., 1971, “Averaged field equations for two-phase media”, Stud. Appl. Math., Vol. 1-2, 133-136.

Drew, D. A., 1983, “Mathematical modeling of two-phase flow”, Annu. Rev. Fluid Mech., Vol. 15, pp. 261-291.

Enwald, H., Peirano, E. and Almstedt, A. -E., 1996, “Eulerian two-phase flow theory applied to fluidization”, Int. J. Multiphase Flow, Vol. 22, pp. 21-66.

Ergun, S., 1952, “Fluid Flow through Packed Columns”, Chem. Engng. Prog., Vol. 48, No. 2, pp 89-94.

Geldart, D.., 1986, “ Gas Fluidization Technology ”, John Wiley & Sons, New York, 1986.

Gidaspow, D., 1994, “Multiphase Flow and Fluidization”, Academic Press, San Diego, CA, 407p.

Gidaspow, D., Ettehadieh, B., 1983, " Fluidization in two-dimensional beds with a jet. 2. Hydrodynamics modeling ", I & EC Fundam., v.22, p.193-201.

Goldhirsch, I., Tan, M. -L. and Zanetti, G., 1993, “A molecular dynamical study of granular fluids I: the unforced granular gas in two dimensions”, Journal of Scientific Computing, Vol. 8, No. 1, pp. 1-40.

Grace, J.R., 1982, “ Fluidized-Bed Hydrodynamics ”, in Handbook of Multiphase Systems, Ed. Hetsroni, G., Hemisphere, Washington, pp., 8:5-64.

Haider, Levenspiel, 1989, "Drag Coefficient and Terminal Velocity of Spherical and Nonspherical Particles" Powder Technology, Vol. 58, pp. 63-70.

Hrenya, C. M., Sinclair J. L., 1997, " Effects of particle-phase turbulence in gas-solid flows ", AIChE J., Fluid Mechanics and Transport Phenomena Vol. 43, Issue 4 pp. 853-869.

Igci, Y. and Sundaresan, S., 2010, "Verification of filtered two-fluid models for gas-particle flows in risers", AIChE J., Vol. 57, pp. 2691-2707.

Igci, Y. and Sundaresan, S., 2011, "Constitutive models for filtered two-fluid models of fluidized gas-particle flows", Ind. Eng. Chem. Res., Vol. 50, pp. 13190-13201.

Igci, Y., Andrews IV, A.T., Sundaresan, S., Pannala, S. and O'Brien, T., 2008, "Filtered two-fluid models for fluidized gas-particle suspensions", AIChE Journal, Vol. 54, No. 6, pp. 1431-1448.

Igci, Y., Pannala, S., Benyahia, S. and Sundaresan, S., 2012, "Validation studies on filtered model equations for gas-particle flows in risers", Ind. & Eng. Chem. Res., Vol. 51, pp. 2094-2103.

Ishii, M., 1975, "Thermo-fluid dynamic theory of two-phase flow", Eyrolles, Paris.

Jenkins, J. T., Savage, S. B., 1983, "A Theory for the rapid flow of identical, smooth, nearly elastic spherical particles", J. Fluid Mech., Vol. 130, pp. 187-202.

King, D., Potter, O. E., Nicklin, D. J. eds. " Fluidized Catalytic Crackers: An Engineering Review ", in Fluidization VII, Engineering Foundation, New York, 1992.

Kunii, D., Levenspiel, O., "Fluidization Engineering", 2nd edition, Butterworth-Heineman, Boston and Butterworth-Heinemann, Stoneham, 1991.

Lun, C. K. K., Savage, S. B., Jeffrey, D. J. and Chepurniy, N., 1984, "Kinetic theories for granular flows: inelastic particles in Couette flow and singly inelastic particles in a general flow field", J. Fluid Mech., Vol. 140, pp. 223-256.

Lun, C. K. K., Savage, S.B., 1986, "The effects of an impact velocity dependent coefficient of restitution on stresses developed by sheared granular materials", Acta Mech., Vol. 63, pp. 15-44.

Milioli, C. C., Milioli, F. E., 2011, " On the Subgrid Behavior of Accelerated Riser Flows for a High Stokes Number Particulate ", Industrial & amp, Engineering Chemistry Research Vol. 50 pp. 13538-13544.

Milioli, C. C., Milioli, F.E., Holloway, W., Agrawal, K. and Sundaresan, S., 2013, "Filtered two-fluid models of fluidized gas-particle flows: New constitutive relations", AIChE J., Vol. 59, pp. 3265-3275.

Milioli, F.E., 2016, "Relatório de Pesquisa", Princeton University-USA.

Ozarkar, S. S., Yan, X., Wang, S., Milioli, C.C., Milioli, F.E. and Sundaresan, S., 2015, "Validation of filtered two-fluid models for gas-particle flows against experimental data from bubbling fluidized bed", Powder Technology, Vol. 284, pp. 159–169.

Ozel, A., Fede, P. and Simonin, O., 2013, "Development of filtered Euler–Euler two-phase model for circulating fluidised bed: High resolution simulation, formulation and a priori analyses", Int. J. Multiphase Flow, Vol. 55 . pp. 43-63.

Parmentier J-F, Simonin O, Delsart O., 2012, "A functional subgrid drift velocity model for filtered drag prediction in dense fluidized bed", AIChE J., Vol. 58, pp. 1084-1098.

Ranade, V. V., 2002, " Computational flow modeling for chemical reactor engineering ", Academic Press, San Diego, CA, USA, 452 pages.

Rowe, P.N., 1961, "Drag Forces in a Hydraulic Model of a Fluidized Bed. Part II", Trans. IChemE, Vol. 39, pp. 175-180.

Sarkar, A., Suna, X., Li, T., Milioli, F.E., and Sundaresan, S., 2016, "Filtered sub-grid constitutive models for fluidized gas-particle flows constructed from 3-D simulations", submitted to Powder Technology.

Schiller, L., Neumann, Z., 1935, Ver. Deutsch Ing.

Schneiderbauer, S., Pirker, S., 2014, "Filtered and Heterogeneity-Based Subgrid Modifications for Gas–Solid Drag and Solid Stresses in Bubbling Fluidized Beds", AIChE

J., Vol. 60, pp. 839-854.

Sharma, A.K., Tuzla, K., Matsen, J. and Chen, J.C., 2000, " Parametric Effects of Particle Size and Gas Velocity on Cluster Characteristics in Fast Fluidized Beds ", Powder Technology, 111, 114.

Sun, G., Grace J.R., 1992, " Effect of particle size distribution in different fluidization regimes ", AIChE J., Vol. 38 pp. 716–722.

Sundaresan, S., 2000, "Hydrodynamics of multiphase flow reactors: current status and challenges", AIChE Journal, Vol. 46, No. 6, pp. 1102-1105.

Syamlal, M., 1998, "MFIX documentation numerical technique", DE-AC21-95MC31346 U.S. Department of Energy, EG&G Technical Services of West Virginia, Morgantown-WV, USA.

Syamlal, M., Rogers, W. and O'Brien, T. J., 1993, "Theory guide", MFIX documentation, Vol. 1, DOE/METEC-9411004 NTIS/DE9400087, National Technical Information Service, Springfield, VA.

Tan, M. -L. and Goldhirsch, I., 1997, "Intercluster interactions in rapid granular shear flows", Physics of Fluids, Vol. 9, No. 4, pp. 856-869.

van der Hoef, M.A., Ye, M., van Sint Annaland, M., Andrews IV, A.T., Sundaresan, S. and Kuipers, J.A.M., 2006, "Multiscale modeling of gas-fluidized beds", Adv. in Chemical Engineering, Vol. 31, pp. 65-149.

Wen, C.Y. and Yu, Y.U., 1966, "Mechanics of fluidization", Chem. Engng. Prog. Symp. Series, Vol. 62, pp. 100-111.

Zhang, D.Z. and van der Heyden, W.B., 2002, "The effects of mesoscale structures on the macroscopic momentum equations for two-phase flows", Int. J. Multiphase Flow, Vol. 28, pp. 805-822.

Appendix

APPENDIX A – DRAG COEFFICIENT CORRECTION, H

Drag coefficient correction, H, for the dimensionless filter sizes $\Delta_f / (\mathbf{v}_t^2/\mathbf{g}) = 1.028$ and 4.112.

Figure 19: Drag coefficient correction, H, as a function of the filtered solid volume fraction, $\overline{\phi}_s$, for various gas Reynolds ratios $\langle Re_g\rangle/\langle Re_g\rangle_{susp} = 1$ (–), 4.08 (○), 8.15 (◁), 12.23 (◇), 16.30 (▷), 20.34 (□), and 24.45 (▽), for the domain average solid volume fraction $\langle\phi_s\rangle = 0.05$ (a), 0.15 (b) and 0.25 (c). The results stand for the dimensionless filtered axial slip velocities $\tilde{\mathbf{v}}_{slip,y}/\mathbf{v}_t = 0.85$, 2.03 and 4.85, and the dimensionless filter size $\Delta_f/\left(\mathbf{v}_t^2/\mathbf{g}\right) = 1.028$

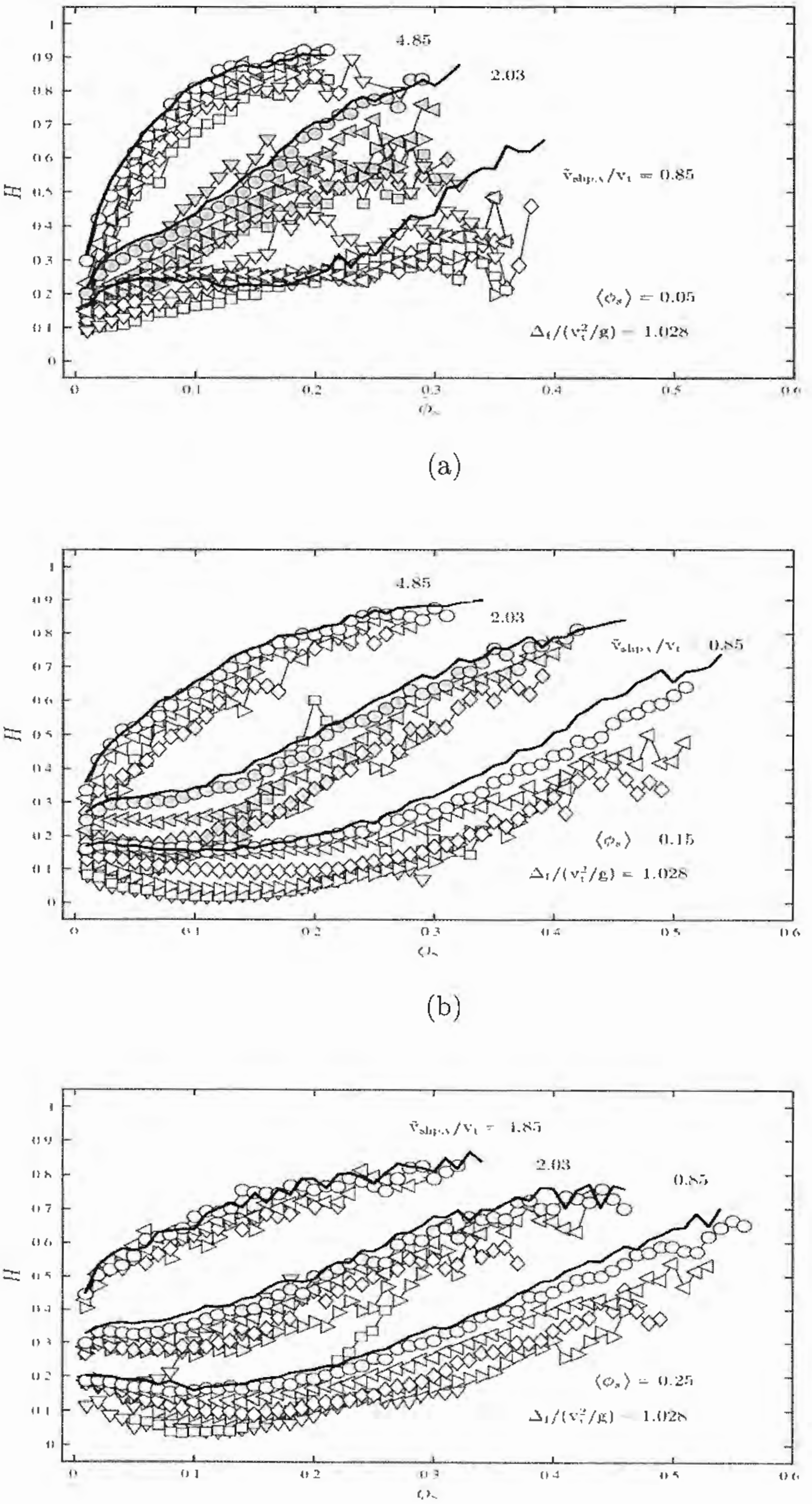

(a)

(b)

(c)

Figure 20: Drag coefficient correction, H, as a function of the filtered solid volume fraction, $\overline{\phi}_s$, for various gas Reynolds ratios $\langle Re_g \rangle / \langle Re_g \rangle_{susp} = 1$ (–), 4.08 (○), 8.15 (◁), 12.23 (◇), 16.30 (▷), 20.34 (□), and 24.45 (▽), for the domain average solid volume fraction $\langle \phi_s \rangle = 0.05$ (a), 0.15 (b) and 0.25 (c). The results stand for the dimensionless filtered axial slip velocities $\tilde{\mathbf{v}}_{slip,y}/\mathbf{v}_t = 0.85$, 2.03 and 4.85, and the dimensionless filter size $\Delta_f / \left(\mathbf{v}_t^2/\mathbf{g}\right) = 4.112$

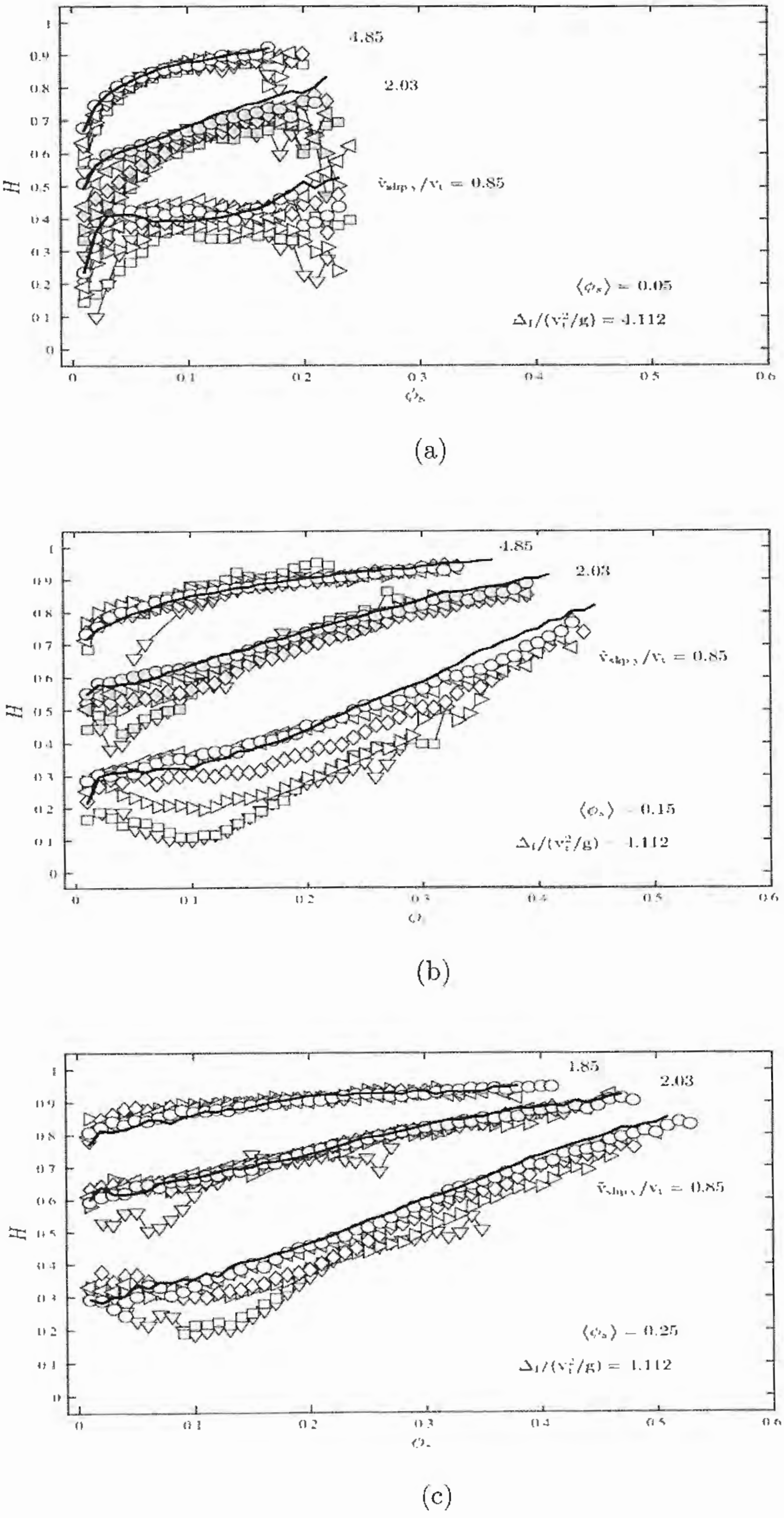

Figure 21: Drag coefficient correction, H, as a function of the filtered solid volume fraction, $\overline{\phi}_s$, for the domain average solid volume fractions $\langle\phi_s\rangle = 0.05$ (full lines), 0.15 (gray symbols) and 0.25 (white symbols), for gas Reynolds ratios $\langle Re_g\rangle/\langle Re_g\rangle_{susp} = 1$ (a), 4.08 (b), 8.15 (c), 12.23 (d), 16.30 (e), 20.34 (f). The results stand for the dimensionless filtered axial slip velocities $\tilde{\mathbf{v}}_{slip,y}/\mathbf{v}_t = 0.85$, 2.03 and 4.85, and the dimensionless filter size $\Delta_f/\left(\mathbf{v}_t^2/\mathbf{g}\right) = 1.028$

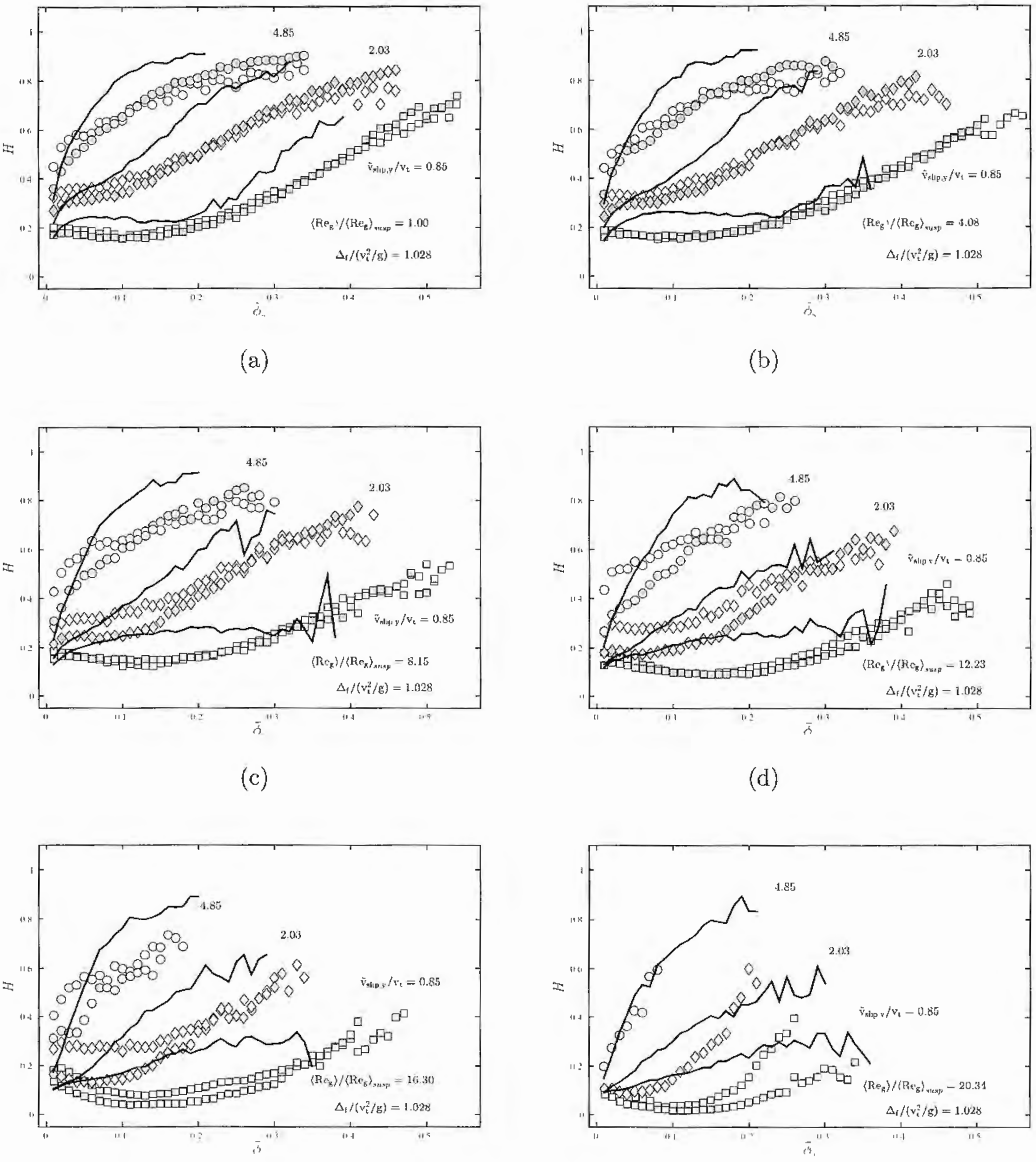

(a)

(b)

(c)

(d)

(e)

(f)

Figure 22: Drag coefficient correction, H, as a function of the filtered solid volume fraction, $\overline{\phi}_s$, for the domain average solid volume fractions $\langle \phi_s \rangle = 0.05$ (full lines), 0.15 (gray symbols) and 0.25 (white symbols), for gas Reynolds ratios $\langle Re_g \rangle / \langle Re_g \rangle_{susp} = 1$ (a), 4.08 (b), 8.15 (c), 12.23 (d), 16.30 (e), 20.34 (f). The results stand for the dimensionless filtered axial slip velocities $\tilde{\mathbf{v}}_{slip,y}/\mathbf{v}_t = 0.85$, 2.03 and 4.85, and the dimensionless filter size $\Delta_f / \left(\mathbf{v}_t^2/\mathbf{g}\right) = 4.112$

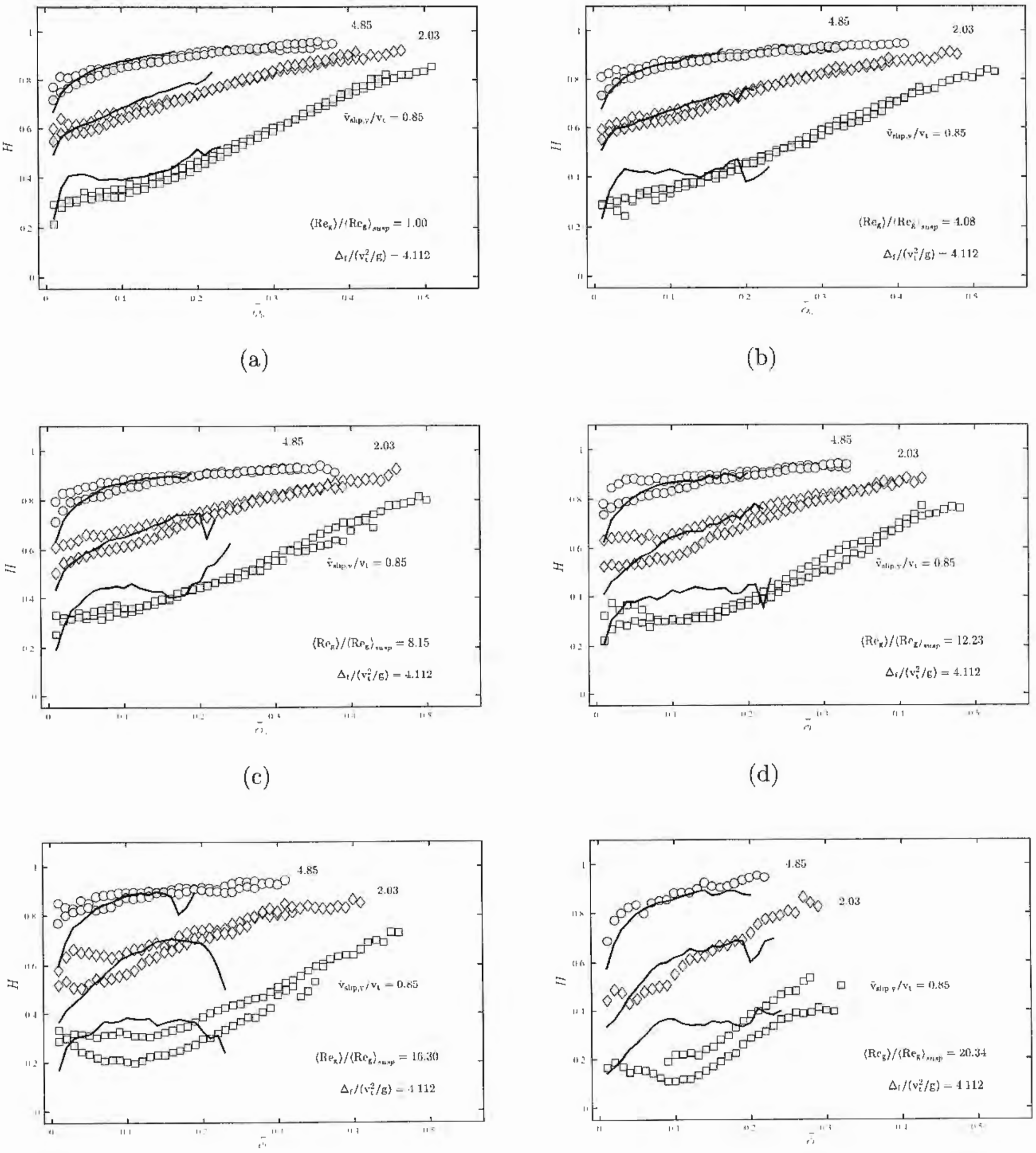

(a) (b)

(c) (d)

(e) (f)

Figure 22: Drag coefficient correction, H, as a function of the filtered solid volume fraction, $\overline{\phi}_s$, for the domain average solid volume fractions $\langle\phi_s\rangle = 0.05$ (full lines), 0.15 (gray symbols) and 0.25 (white symbols), for gas Reynolds ratios $\langle Re_g\rangle / \langle Re_g\rangle_{susp} = 1$ (a), 4.08 (b), 8.15 (c), 12.23 (d), 16.30 (e), 20.34 (f). The results stand for the dimensionless filtered axial slip velocities $\tilde{\mathbf{v}}_{slip,y}/\mathbf{v}_t = 0.85$, 2.03 and 4.85, and the dimensionless filter size $\Delta_f / (\mathbf{v}_t^2/\mathbf{g}) = 4.112$

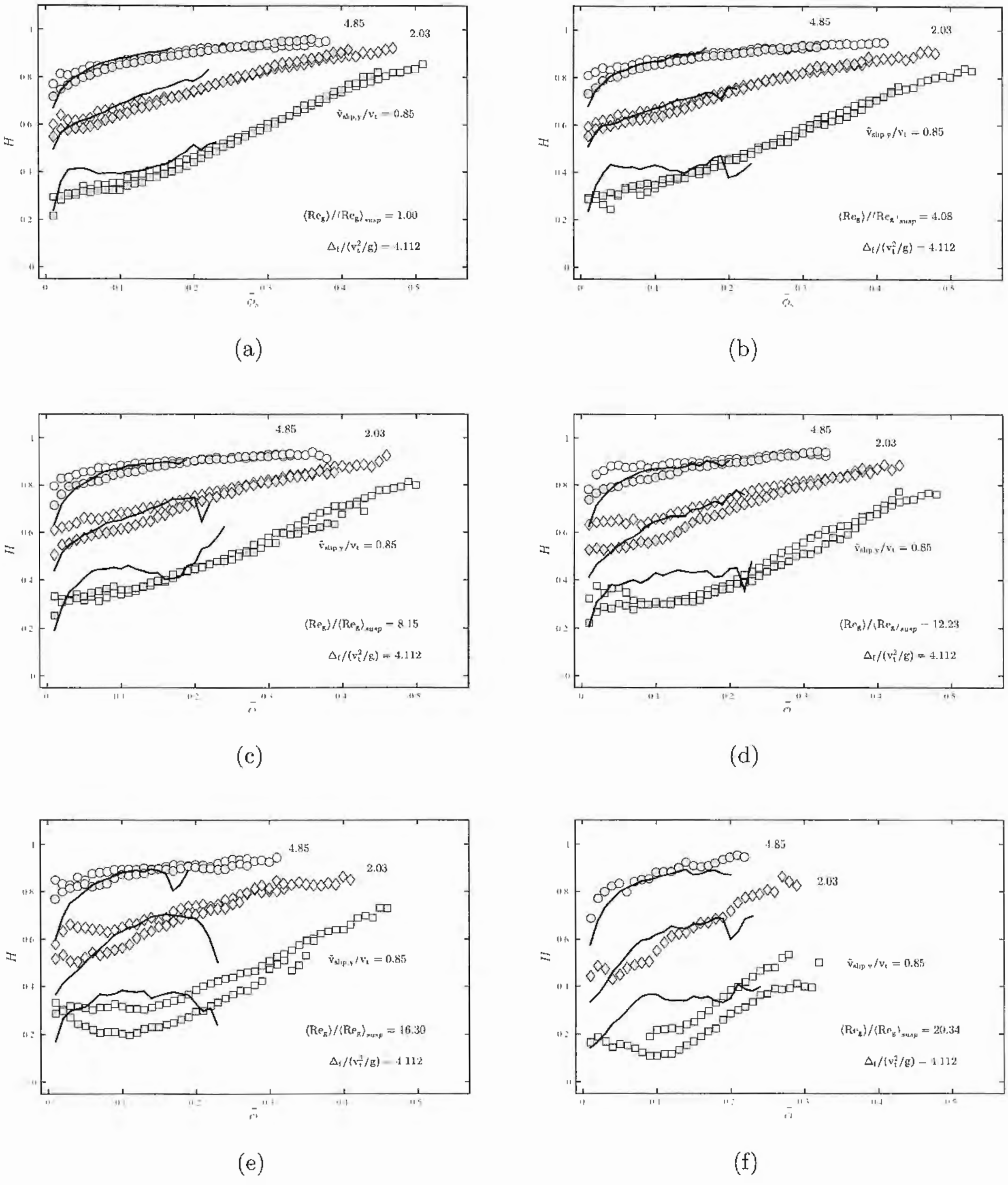

(a)

(b)

(c)

(d)

(e)

(f)

APPENDIX B – FILTERED SOLID PRESSURE, $P_{fil,s}$ AND DYNAMIC VISCOSITY $\mu_{fil,s}$

Filtered solid pressure, $P_{fil,s}$ and dynamic viscosity $\mu_{fil,s}$ for the dimensionless filter sizes $\Delta_f/\left(\mathbf{v}_t^2/\mathbf{g}\right) = 1.028$ and 4.112.

Figure 23: Filtered solid pressure, $P_{fil,s}$, as a function of the filtered solid volume fraction, $\overline{\phi}_s$, for various gas Reynolds ratios $\langle Re_g \rangle / \langle Re_g \rangle_{susp} = 1$ (−), 4.08 (○), 8.15 (◁), 12.23 (◊), 16.30 (▷), 20.34 (□), and 24.45 (▽), for the domain average solid volume fraction $\langle \phi_s \rangle = 0.05$ (a), 0.15 (b) and 0.25 (c). The results stand for the dimensionless filtered axial slip velocity $\tilde{\mathbf{v}}_{slip,y}/\mathbf{v}_t = 0.85$ and the dimensionless filter size $\Delta_f / \left(\mathbf{v}_t^2/\mathbf{g} \right) = 1.028$

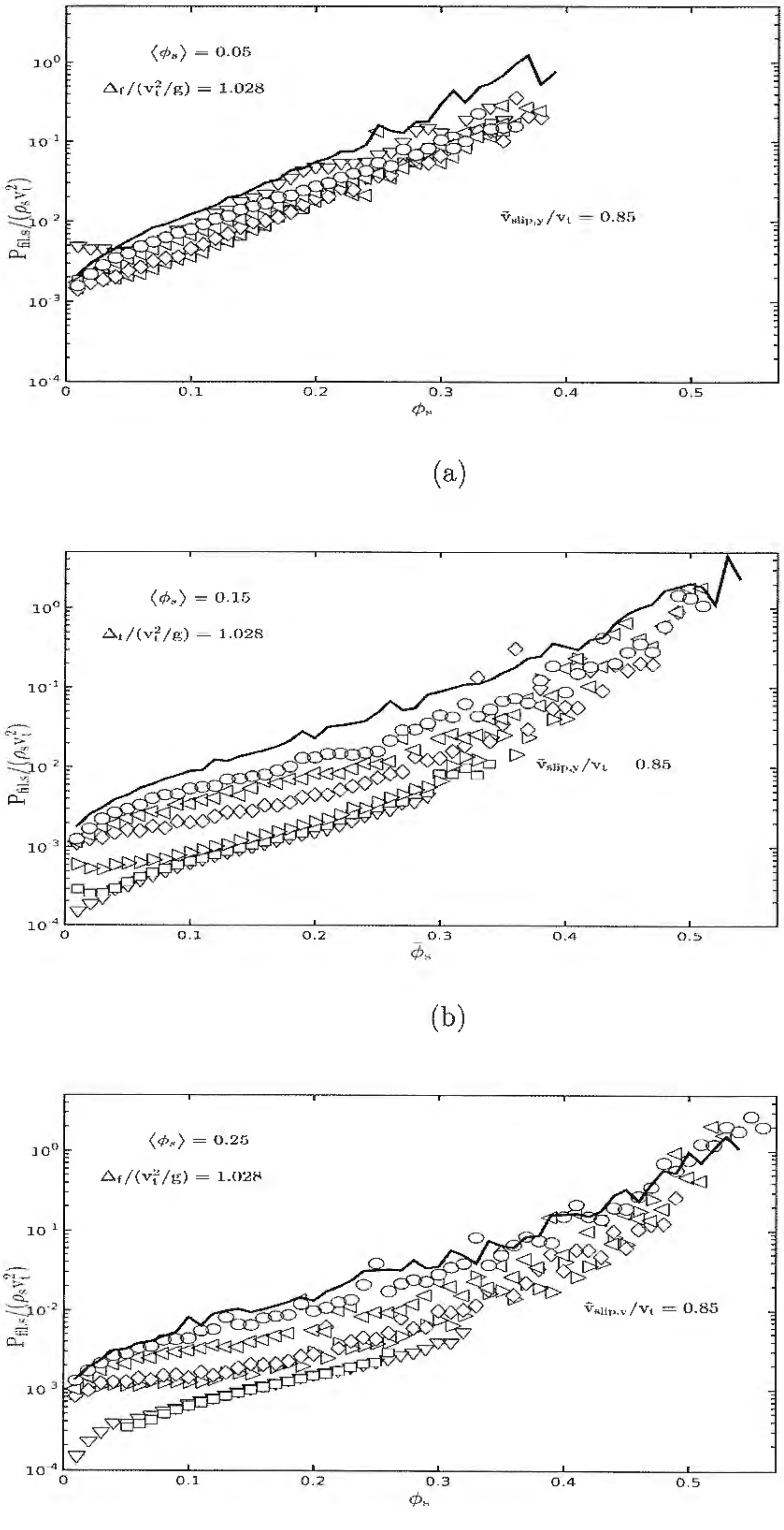

(a)

(b)

(c)

Figure 24: Filtered solid pressure, $P_{fil,s}$, as a function of the filtered solid volume fraction, $\overline{\phi}_s$, for various gas Reynolds ratios $\langle Re_g \rangle / \langle Re_g \rangle_{susp} = 1$ (−), 4.08 (○), 8.15 (◁), 12.23 (◇), 16.30 (▷), 20.34 (□), and 24.45 (▽), for the domain average solid volume fraction $\langle \phi_s \rangle = 0.05$ (a), 0.15 (b) and 0.25 (c). The results stand for the dimensionless filtered axial slip velocity $\tilde{\mathbf{v}}_{slip,y}/\mathbf{v}_t = 0.85$ and the dimensionless filter size $\Delta_f / \left(\mathbf{v}_t^2/\mathbf{g}\right) = 4.112$

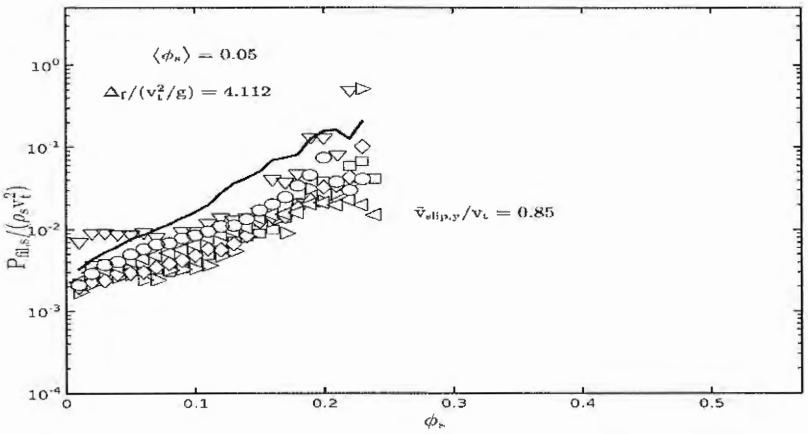

(a)

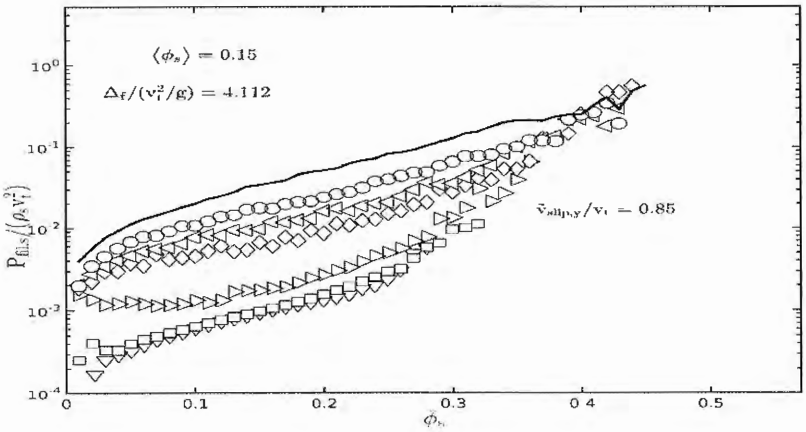

(b)

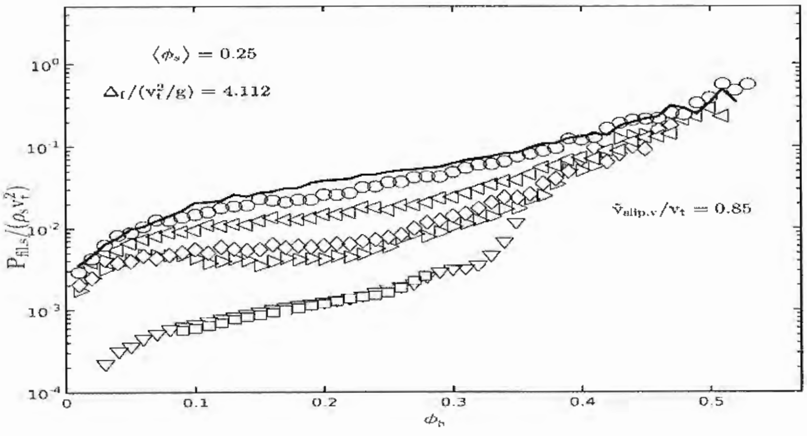

(c)

Figure 25: Filtered solid dynamic viscosity, $\mu_{fil,s}$, as a function of the filtered solid volume fraction, $\overline{\phi}_s$, for various gas Reynolds ratios $\langle Re_g \rangle / \langle Re_g \rangle_{susp} = 1$ (–), 4.08 (○), 8.15 (◁), 12.23 (◇), 16.30 (▷), 20.34 (□), and 24.45 (▽), for the domain average solid volume fraction $\langle \phi_s \rangle = 0.05$ (a), 0.15 (b) and 0.25 (c). The results stand for the dimensionless filtered axial slip velocity $\tilde{\mathbf{v}}_{slip,y}/\mathbf{v}_t = 0.85$ and the dimensionless filter size $\Delta_f / (\mathbf{v}_t^2/\mathbf{g}) = 1.028$

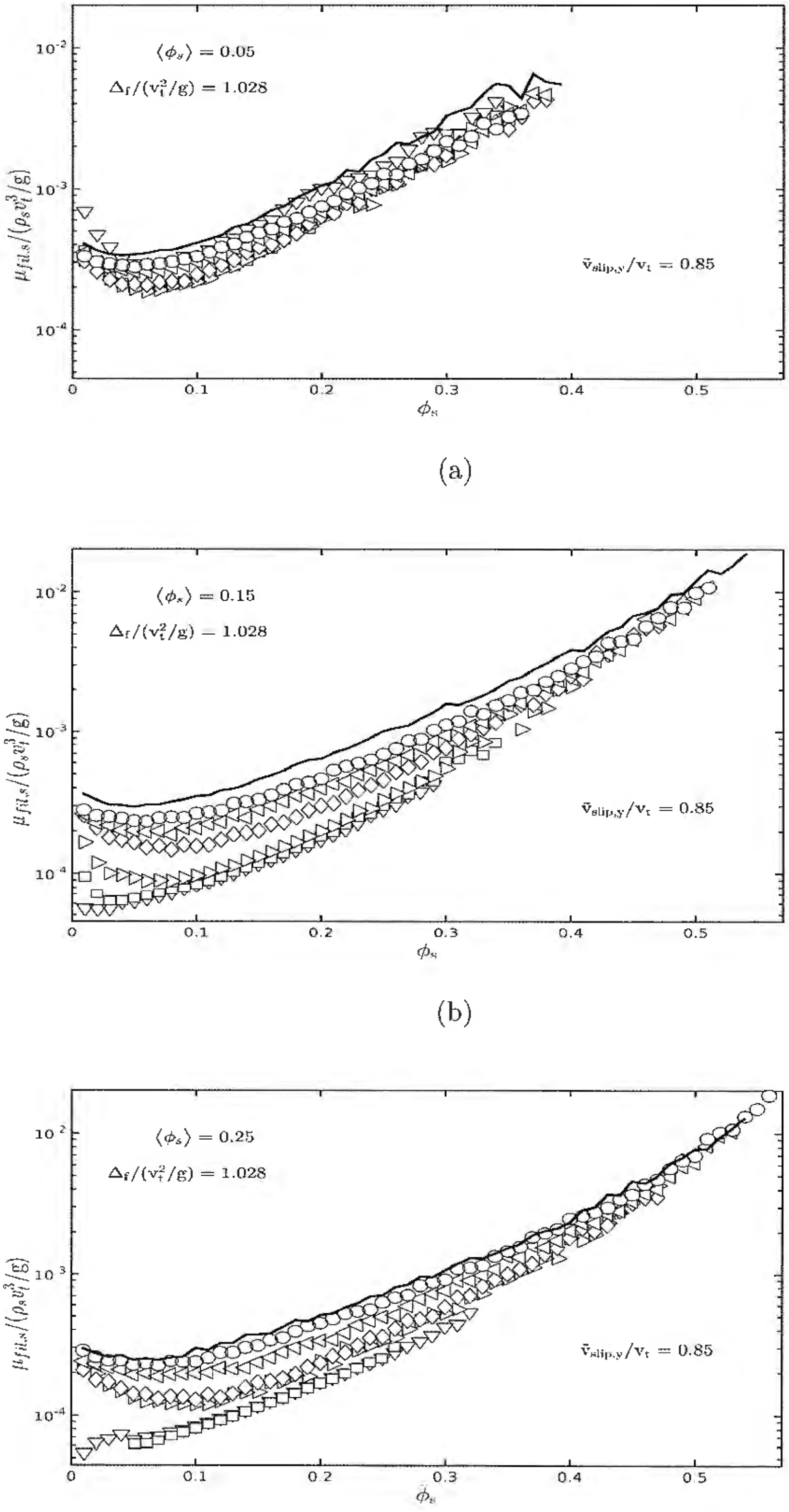

(a)

(b)

(c)

Figure 26: Filtered solid dynamic viscosity, $\mu_{fil,s}$, as a function of the filtered solid volume fraction, $\overline{\phi}_s$, for various gas Reynolds ratios $\langle Re_g\rangle/\langle Re_g\rangle_{susp} = 1$ (−), 4.08 (○), 8.15 (◁), 12.23 (◇), 16.30 (▷), 20.34 (□), and 24.45 (▽), for the domain average solid volume fraction $\langle\phi_s\rangle = 0.05$ (a), 0.15 (b) and 0.25 (c). The results stand for the dimensionless filtered axial slip velocity $\tilde{\mathbf{v}}_{slip,y}/\mathbf{v}_t = 0.85$ and the dimensionless filter size $\Delta_f/\left(\mathbf{v}_t^2/\mathbf{g}\right) = 4.112$

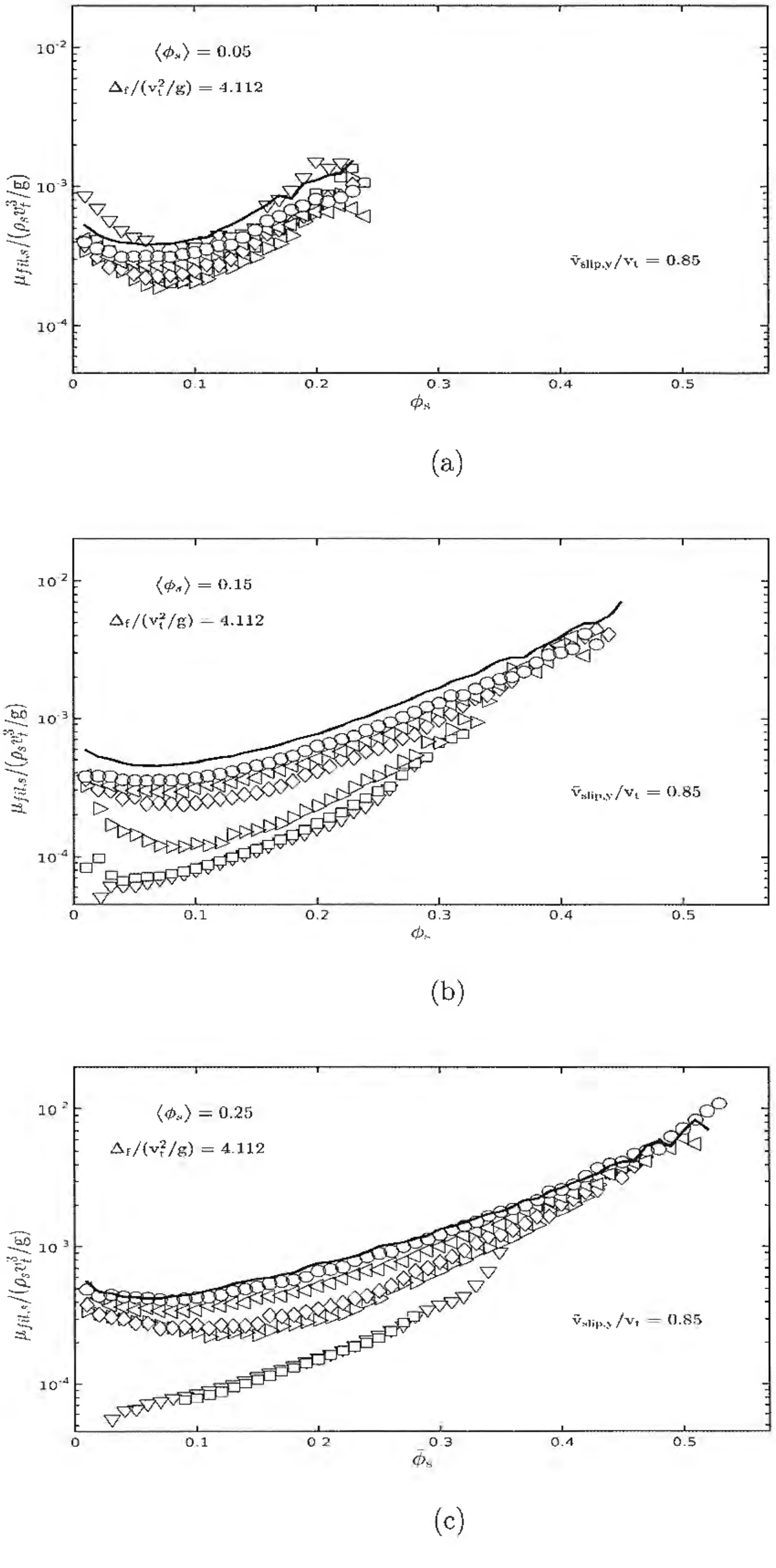

(a)

(b)

(c)